DESIGN, SYNTHESIS AND CHARACTERIZATION OF ORGANIC SEMICONDUCTORS: FROM EUMELANIN-INSPIRED ORGANIC MATERIALS TO NOVEL ELECTRON ACCEPTORS

By

SANTOSH ADHIKARI

Bachelor of Science in Chemistry
Tribhuvan University
Kathmandu, Nepal
2005

Master of Science in Physical Chemistry
Tribhuvan University
Kathmandu, Nepal
2009

Submitted to the Faculty of the
Graduate College of the
Oklahoma State University
in partial fulfillment of
the requirements for
the Degree of
DOCTOR OF PHILOSOPHY
July, 2018

DESIGN, SYNTHESIS AND CHARACTERIZATION OF ORGANIC SEMICONDUCTORS: FROM EUMELANIN-INSPIRED ORGANIC MATERIALS TO NOVEL ELECTRON ACCEPTORS

Dissertation Approved:

Dr. Toby L. Nelson

Dissertation Adviser

Dr. Frank D. Blum

Dr. Richard A. Bunce

Dr. Ziad El Rassi

Dr. Mario F. Borunda

ACKNOWLEDGEMENTS

My PhD journey would not be successfully completed without the professional guidance from my advisory committee members, valuable suggestions from my group members, continuous encouragement from my friends and indispensable support and prayers from my family members.

At first I would like to express my sincere gratitude to my adviser Dr. Toby L. Nelson for his unwavering support, suggestions and motivation during my PhD journey. Thank you Dr. Nelson for encouraging, caring, providing a free science research environment and always believing in me. I have found myself growing as a good researcher and person under your noble guidance. I am always impressed by the way you motivate, mentor, help and love your students and prepare them for the future.

I am also thankful to all my advisory committee members: Dr. Frank D. Blum, Dr. Richard A. Bunce, Dr. Ziad El Rassi, and Dr. Mario F. Borunda for their support, suggestions, and precious time. Thank you for reading my proposal, dissertation and attending my defenses despite of your busy schedules. To Dr. Nelson, Dr. Blum and Dr. Bunce, thank you for writing letters of support for me that have landed me a postdoctoral position.

My graduate life would not be so joyful and relaxed without the presence of really helpful and supportive group members: Subha, Daniel, Dev, Paula, Niradha, Fathima, Martha, and Megan. Thank you all for your advice, support and making our group a family like environment.

Most of my projects were completed in collaboration with researcher from different fields. Many thanks to all my collaborators: Dr. Erika Lutter, Dr. Saadyah Averick, and Dr. Mario F. Borunda for their help in completing my projects. To Dr. Lutter, thank you very much for helping me understand and write the eumelanin-inspired antimicrobial project.

I would also like to acknowledge the Center for C-H Functionalization (CCHF) for providing me an opportunity to do research at Seth Marder's lab in Georgia Institute of Technology as Summer Scholar.

I am also thankful to the Chemistry Department, Oklahoma State University for providing me an opportunity to earn my PhD here. I am also grateful to all the faculty, staff and graduate students of the Chemistry Department.

I am also grateful to my Master's degree adviser Dr. Rameshwar Adhikari for his motivation and encouragement. He is one of my role models.

I would also like to thank all of my friends. To Man B. Karki, thank you for always believing on me and motivating and encouraging me.

I would like to dedicate my PhD work to my mother, Sita Adhikari and my late father Dharma Dutta Adhikari. I have grown witnessing the hard work and determination of my mother to provide good life and education to our family. And I know she is the

happiest person to see me graduating with a PhD degree. Thank you, Mom, for your hard work, prayers and belief on me. I would also like to thank all my family members for their support; my brother Madhav Adhikari, my sister Sabitri Adhikari, my parents-in-law Til Prasad Sapkota and Rita Sapkota, and brothers-in-law Prakash Sapkota and Pradeep Sapkota.

And last but not the least, I would like to thank the most important persons of my life; my dearest wife, Prabina Sapkota and my beautiful daughter Sarvajna Adhikari. Prabina, thank you very much for your love, care, support and prayers. I could not complete my journey without your support. Thank you very much for everything. Please join me to share our success.

Name: SANTOSH ADHIKARI

Date of Degree: JULY, 2018

Title of Study: DESIGN, SYNTHESIS AND CHARACTERIZATION OF ORGANIC SEMICONDUCTORS: FROM EUMELANIN-INSPIRED ORGANIC MATERIALS TO NOVEL ELECTRON ACCEPTORS

Major Field: CHEMISTRY

Abstract:
Eumelanin, the black-brown variety of natural pigment melanin, is a fascinating material owing to its multifunctional physicochemical properties, such as broad-band absorption spectrum, antioxidant and free radical scavenging behavior, strong nonradiative relaxation of photoexcited electronic states and metal chelating properties. Further, biocompatible and biodegradable nature, peculiar physicochemical properties and intrinsic antimicrobial activities make eumelanin a promising material in bioelectronic and biomedical fields. Here, the Eumelanin-inspired indole core has been utilized to synthesize bio-inspired organic semiconductors (OSCs), sensors, and antimicrobials.
In the field of organic semiconductors, both p-type and n-type materials are equally important. While p-type OSCs have seen a dramatic rise in performance over the last decade, n-type OSCs, in general, still lag behind p-type OSCs. This lack of high performance n-type OSCs is mainly related to lower stability, difficulties in synthesis and less availability of electron deficient building blocks that can be used for making n-type OSCs. Both types of OSCs with high performance are required in order to fabricate high-performance complementary circuits or p-n junction devices. Thus, there is a critical need for exploration of new building blocks for making novel n-type OSCs with improved electron mobility, material stability both under processing and operational conditions, and ease of synthesis. Benzo[1,2-b:4,5-b0]dithiophene-1,1,5,5-tetraoxide (BDTT) has seen less utility as a building block to make n-type OSCs despite it being an electron poor heterocycle with promise for development of n-type materials. Difficulties in functionalizing BDTT via carbon-carbon cross coupling reactions and often in low yield is one likely reason for the lack of utilization of BDTT in OSCs. This dissertation will report the successful functionalization and utilization of BDTT for the synthesis of n-type OSCs.
In past few years, organic conductive fibers have emerged as an attractive as well as promising class of materials for realizing non-metallic electrodes for different clinical applications. This is because these materials are biocompatible, better integrated, easier to fabricate, lightweight and have limited magnetic resonance imaging problems compared to the metallic electrodes. This dissertation will highlight novel organic conductive fibers that have been fabricated by a facile, economical, and scalable method by using conductive ink prepared from the two intrinsically conductive materials - poly(3-hexylthiophene) and single walled carbon nanotubes - and these conductive fibers have been utilized as non-metallic electrodes for recording skin surface biological signals.

TABLE OF CONTENTS

Chapter Page

Chapter Page

LIST OF TABLES

LIST OF SCHEMES

LIST OF FIGURES

Figure Page

Figure Page

Figure Page

CHAPTER I

INTRODUCTION

1.1 BACKGROUND

The combination of novel optoelectronic properties with the ability to tailor chemical structures to achieve desired optoelectronic and morphology properties make organic semiconductors (OSCs) attractive materials in the modern technology world. Additionally, OSCs offer the opportunity to fabricate low cost, solution processable, lightweight and flexible electronics and optoelectronic devices which otherwise are inaccessible using conventional semiconductor materials such as silicon.[1,2] Due to these advantages, in past few decades OSCs have attracted a huge attention from the scientific community for their application in organic light emitting diodes (OLEDs)[3], organic photovoltaics (OPVs)[4], organic field effect transistors (OFETs)[5], organic electrically conductive fibers (OECFs)[6] and sensors.[7] While some OSC based devices such as OLEDs have already been successfully commercialized for displays in cell phones, and televisions, many other OSC based technologies still face a huge challenge due to the limited efficiencies and durability of OSCs. Additionally, with the increasing application of OSCs in the biomedical field in past few years,[8,9] it is desired to have more biocompatible and biodegradable OSCs. .Therefore, more research is needed to better understand and develop novel OSCs with high performance and biocompatibility in order to realize them for real life applications.

1.2 ORGANIC SEMICONDUCTORS (OSCs)

OSCs are carbon-rich compounds or carbon-based materials that combine the properties of semiconducting materials with the chemical and mechanical benefits of organic compounds such as plastics. Why do these organic compound exhibit semiconducting properties when a vast number of organic compounds are generally considered as electrical insulating?

Organic molecules having conjugated systems i.e. alternating sigma and pi bonds, allow the electron cloud to delocalize and give them semiconducting properties. Usually, OSCs have molecular sheets with sp^2/sp hybridized carbon atoms. A neutral carbon atom contains four valence electrons; two *2s* electrons and two *2p* electrons. However, these orbitals can undergo three different hybridizations *viz*. *sp*, sp^2 and sp^3 to lower their energy. The *sp* hybridized state results in linear geometry with two unhybridized *2p*-orbitals. Similarly, sp^2 and sp^3 hybridized states result in trigonal planar and tetrahedral geometry with one and zero unhybridized 2*p* orbitals respectively (Figure 1.1). The hybridized orbitals form strong sigma bonds and sigma electrons are localized making the stable carbon chain whereas the unhybridized *p*-orbitals on adjacent carbon atoms can overlap to form weak π bonds. The π electrons system results in the planarity of the molecule and can delocalize electron over many carbon atoms by the process called conjugation.

In ethene, when half-filled p_z orbitals on adjacent carbon atoms overlap, it results in the formation of two molecular orbitals (MOs) *viz.* π (bonding) and π^* (antibonding) MOs. A π MO has lower energy than a π^* MO so two unpaired *pz* electrons occupy the π MO orbital leaving behind an unoccupied π^* MO. The energy difference between the highest occupied molecular orbital (HOMO) and the lowest unoccupied molecular orbital (LUMO) is known as the band gap, which is analogous to the band gap in inorganic semiconductors. With the increase in conjugation, more and more π orbitals will be formed resulting in a quasi-continuous band of π and π^* MOs and a narrowing of the gap between the HOMO and LUMO as illustrated in Figure 1.2. In band theory, these quasi-continuous band of π and

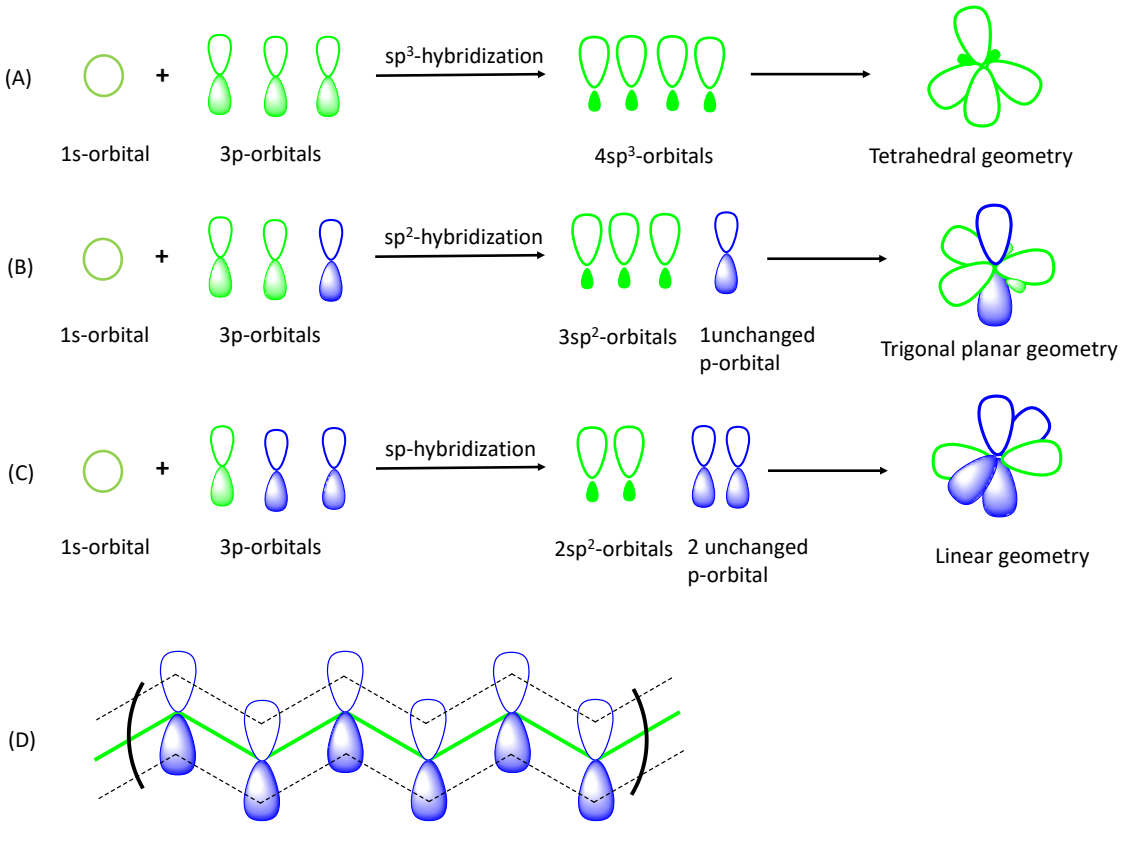

Figure 1.1: Schematics of the electronic orbitals of (A) sp^3 hybridization, (B) sp^2 hybridization, (C) *sp* hybridization, and (D) delocalization of unhybridized *p*-orbitals (conjugation).[10]

π^* MOs are also referred as valence band and conductive bands, respectively. In addition, π orbitals of different molecules may overlap when they come together by the process called $\pi - \pi$ stacking. This results in the intermolecular delocalization of electrons and further reduces the band gap. This combination of intra and inter-molecular delocalization of electrons can make organic compounds semiconductors. And these OSCs have band gap generally less than or equal to 3.2 eV and can absorb light from near the UV-region to the near IR region.

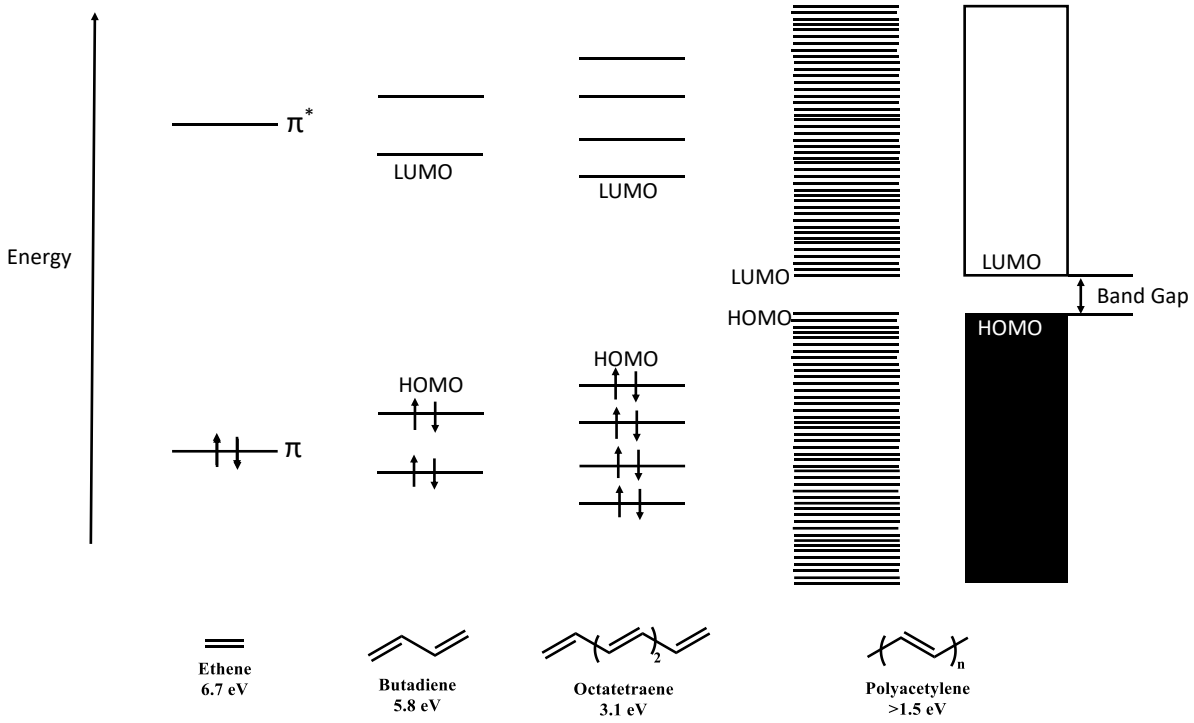

Figure 1.2: Schematic of energy-level splitting in alkenes and decrease in band gap with increasing conjugation length.[10]

1.2.1 Classification of OSCs

Broadly, organic semiconductors materials can be categorized into three main groups; small molecules, polymers and biological materials.[11] Small molecule OSCs refer to compounds with well-defined molecular weights whereas polymers are macromolecules with molecular weight distribution due to the presence of an uncertain number of repeating units. Some important examples of small molecules and polymer OSCs are given in Figure 1.3. While these two classes of OSCs have more similarities in their optoelectronic properties, the major difference lies on the methods of thin film deposition and device fabrication. Small molecules typically have less solubility in common organic solvents and thus are difficult to spin-cast or ink-jet print and hence have to use vapor deposition methods whereas polymers are processed in solution.[1] Vacuum evaporation is more complex than solution processing, but provides quite pure materials with well-controlled structure and layer

thickness. Further, small molecules OSCs are easily reproduced while in polymers there can be batch-to-batch variation.[12] However, with recent developments in synthetic methodology, small molecule OSCs that can be processed in solution and polymers with less variation from batch-to-batch synthesis can be achieved. In polymer OSCs, the possibility of producing branched, cross-linked, or network polymers allows greater tailoring of the mechanical properties and copolymerizing from different monomers allows a single polymer to combine properties of various monomer materials.[13]

Another class of OSCs is the biological or bio-inspired materials. In the past few years, researchers are more interested on biological or bio-inspired materials as these are more biocompatible and eco-friendly with the potential to be used in the biomedical field and also these materials could have a positive impact to address the current problem of electronic waste.[14] One example of a biological or bio-inspired material is indigoid dye, which represents an interesting class of natural organic semiconducting materials. It has been found that the vacuum-deposited films of 6,6'-dibromoindigo (Tyrian purple) have demonstrated field effect mobility of 0.4 cm^2/Vs for holes and 0.3 cm^2/Vs for electrons showing ambipolar nature.[14] Similarly, melanin is also a natural occurring pigmentary macromolecule showing semiconducting properties.[15,16] The details on melanin will be discussed later in this dissertation.

Based on the major charge carrier, all these OSCs are classified into two types, *viz.* p-type OSCs and n-type OSCs. The OSCs in which holes are the major carrier are p-types and these are electron donors with a high lying HOMO. Whereas in n-type OSCs, electrons are the major carrier and these are electron deficient materials with a low lying LUMO. Materials that have both electron as well as hole mobility are called ambipolar.[17] During the past few decades, a lot of research has been devoted to the development of OSCs and researchers have been successful in achieving high performance OSCs. For example, in OFETs, high mobilities of up to ~ 40 $cm^2V^{-1}s^{-1}$ for both single crystal[18] and aligned small molecules[19] and ~ 50 $cm^2V^{-1}s^{-1}$ for well-aligned polymers[20] have been reported.

Similarly, high mobilities above 10 $cm^2V^{-1}s^{-1}$ have been achieved for solution processed OFET devices for several polymer OSCs.[21,22] These mobility data are much higher than that of amorphous silicon (0.1 to 1 $cm^2V^{-1}s^{-1}$) and are already in the mobility regime of multi-crystalline silicon.

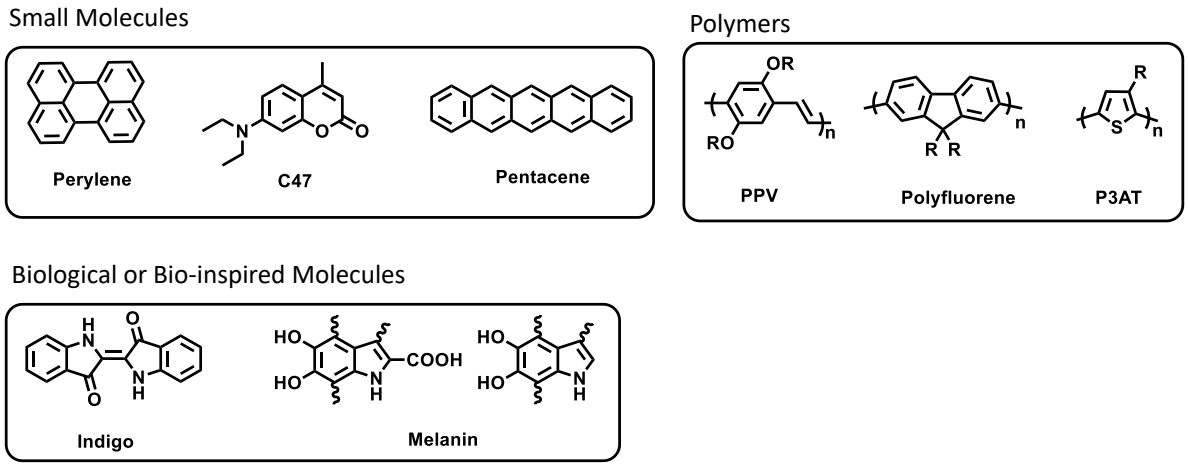

Figure 1.3: Examples of small molecules, conjugated polymers, and biological or bio-inspired OSCs.

However, most of these high performance OSCs are achieved for p-type OSCs. There are far fewer n-type OSCs reported and their performance still lags behind the p-type OSCs. The lack of high performance n-type OSCs are mainly related to the instability of n-type materials, lower availability of electron deficient building blocks, and difficulties in the synthesis of these materials.[23,24] The most widely used n-type material for organic solar cells are fullerene derivatives such as phenyl-C_{61}-butyric acid methyl ester ($PC_{60}BM$) and its C_{71} analogue $PC_{70}BM$. Organic solar cells with the best efficiency (over 11%) are usually achieved using fullerene derivatives as acceptors.[25,26] However, they are limited by the high synthetic costs, low optical absorption, poor bandgap tunability and morphological instability.[27] Rylene diimide, isoindigo, and diketopyrrolopyrrole based small molecules and polymers are the most common high performance n-type materials reported in the literature.[23] However, these materials are either limited by the reduced stability in air or by low

electron mobility. Thus, there is a need to explore new electron deficient building blocks in order to generate high performance n-type OSCs.

1.2.2 Strategy to Design High Performance OSCs

In p- and n-type OSCs, the electrical conduction is associated with oxidation of a neutral molecule to a cation or reduction of a neutral molecule to an anion respectively. In other words, holes are injected into the HOMO of the p-type OSCs and electrons are injected into the LUMO of the n-type OSCs. Thus, the energy levels of frontier orbitals and hence the bandgap in the solid state plays an important role in determining the performance of these materials. Bao and coworkers[28] have reported that the HOMO energy level should be -5.90 eV or higher to allow a p-channel field effect, and the LUMO energy level should be -3.45 eV or lower to allow a n-channel field effect. However, since n-type OSCs are associated with the formation of anions and the injected electron residing in the LUMO is at high energy state which is intrinsically instable since it is prone to react with oxygen and moisture. Thus, it is desirable to have a LUMO energy level of -4 eV or lower to realize n-type OSCs with stable electron mobility.[23]

Since electron rich and electron poor building blocks have high energy HOMO and low energy LUMO levels respectively, the most common strategy to make p-type OSCs is to utilize electron rich moieties while n-type OSCs utilize electron deficient moieties. Further, by attaching electron donating and electron withdrawing groups onto the conjugated system, the energy level of the frontier orbitals can also be tuned. The common electron donating groups that have been employed are alkoxy groups, amino groups, etc. and the most common electron withdrawing groups that have been used are fluorides, nitriles, amides, and imides and so on.

The important strategy to design high performance OSCs is to use donor-acceptor (D-A) type structures, i.e. the molecule has the repeat unit of an electron donor (D) unit and an electron acceptor (A) unit alternately along the conjugated system. Most of the high performance OSCs both p-types

and n-types reported so far have this type D-A structures. This is because such alternating D-A structures would have properties of both donor as well as acceptor moieties which will increase the HOMO energy level on one hand while on the other hand lowers the LUMO energy level resulting in a low band gap. Furthermore, such structures have stronger intermolecular interaction, which shortens the π-π stacking distance, broadens the solar absorption spectra, and thus promotes the charge carrier hopping along the π-stacks.[23,29]

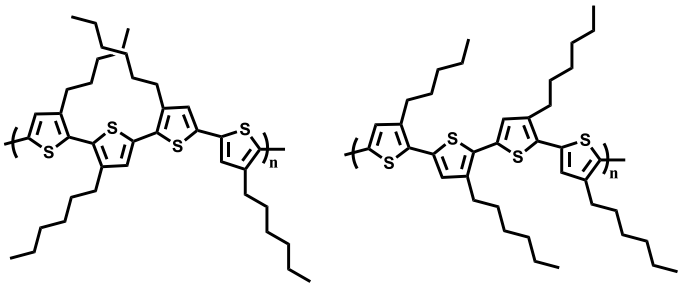

(A) (B)

Figure 1.4: Structure of (A) regioregular and (B) regioirregular P3HT.

Another important approach to design high performance of OSCs is fine tuning of the molecular structure by both molecular framework and side chain engineering.[30] The regiochemistry of the conjugated molecules/polymers obtained from the unsymmetrical building blocks is very important in determining the performance of the resulting OSCs. For example, the conductivity of regioregular poly(3-hexylthiophene) P3HT is much higher than that of regioirregular P3HT (Figure 1.4). This is because the frontier orbitals energy level, stacking pattern, and even solution processability could be regulated by the unsymmetrical building blocks depending on the regiochemistry of the conjugated molecules.[30] Besides improving the solubility of the OSCs, appropriate side chain substitution significantly affects intermolecular packing, thin-film morphology, and thus carrier mobility. Cheng and co-workers[30] have systematically investigated on the charge transport properties of four derivatives of two-dimensional π-expanded quinoidal terthiophenes (2DQTT) with different regiochemistry and alkyl-chain substitution and suggested that fine tuning of the molecular structure

by both molecular framework and side chain engineering is very important to improve the performance of performance OSCs.

1.3 MELANIN AND EUMELANIN

The term 'melanin' was first coined by Berzelius in 1840 to refer to black animal pigments.[31] In general, melanins are naturally occurring pigmentary macromolecules found in all types of living organisms from bacteria to mammals. In mammals, they are found in hair, skin, eye, brain etc. In skin, melanins are synthesized by special cells called melanocytes within membrane-bound organelles termed melanosomes. The amount and type of melanin determines the person's skin's color and the lack of melanin in the skin results in albinism (Figure 1.5).[32-34]

(A) (B)

Figure1.5: (A) Picture of the different skin's color and (B) picture of albino and striped tiger.

Melanins are mainly classified into three main groups *viz:* eumelanins, pheomelanins, and allomelanins. Eumelanins are the black-brown variety of melanin and responsible for the dark colored skin, eye, and hair. The pheomelanins are the yellow-red variety responsible for red hair and freckles. The third type i.e. allomelanins are all other types of melanins encompassing the broad variety of dark non-nitrogenous pigments of plant, fungal, and bacterial origin.[32,34,35] Among different classes of melanins, eumelanins are by far the most relevant from a biological and

technological perspective because of their fascinating multifunctional physiochemical and biological properties.

Eumelanins show broadband and monotonous UV-vis absorption of light ranging from 400 to 700 nm in the electromagnetic spectrum and dissipate 99.9% of absorbed UV and IR radiation by non-radiative pathways and thus act as a natural photoprotector from harmful radiation form the sun. They have antioxidant, free radical scavenging and metal chelating properties. Further, they are known to have intrinsic antimicrobial and antifungal efficacy.[32,33,35] The groundbreaking work of McGuiness and coworkers on electrical switching has established eumelanin as an amorphous semiconductor.[15] After this discovery, eumelanin based materials gained a lot of attention for their use in several applications.[36,37] However, recently Meredith and coworkers have reported that eumelanin is an electronic-ionic hybrid conductor rather than an amorphous semiconductor.[16] Extensive research across biology, chemistry, and physics has been done over a couple of decades to understand the structure and properties of eumelanin,[16,33,35,38-40] but the full details on the structure and functions of the eumelanins are not yet clearly understood. However, it is well known that eumelanins are composed of 5,6-dihydroxyindole, 5,6-dihydroxyindole-3-carboxylic acid and their oxidized derivatives (Figure 1.6).

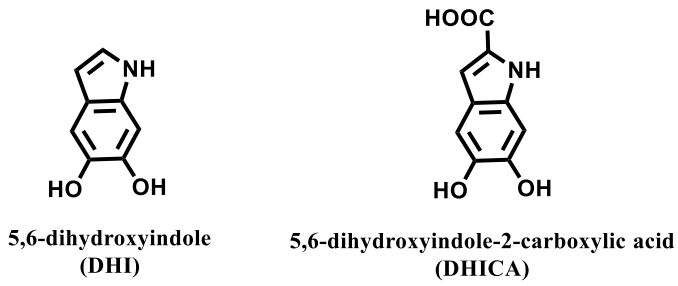

5,6-dihydroxyindole (DHI) **5,6-dihydroxyindole-2-carboxylic acid (DHICA)**

Figure 1.6: Structure of DHI and DHICA.

For decades, natural eumelanins have been considered as extended linear homo- or heteropolymers with a conjugated backbone formed by the oxidative polymerization of derivatives of

dihydroxyindoles. Due to its insolubility in all solvents however, the polymer was considered as undefined. The structure of eumelanin has been better understood now with the development of novel methods for studying condensed-matter physics and chemistry of materials, including imaging techniques and theoretical calculations. Now, the disordered 2D protomolecular sheet model proposed by Meredith and coworkers is widely accepted. According to this model, melanins are not heteropolymers, but are the aggregates formed by the π-stacking of small oligomeric units (less than 10) as in graphite-like-structures.[16,36,38]

In our lab, to better understand the structure-property relationship of eumelanin and to design eumelanin-inspired materials to mimic the properties of natural eumelanin. The eumelanin-inspired indole core, named as DBI (Figure 1.7) was synthesized from the natural product, vanillin extract.[41] In this dissertation, some of the research work has been focused in utilization of this Eumelanin-inspired core to make bio-inspired organic semiconductors and antimicrobials.

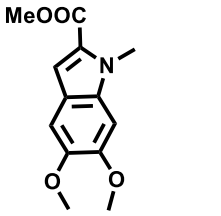

Eumelanin-inspired core (DBI)

Figure 1.7: Structure of DBI.

1.4 REFERENCES

(1) Rockett, A. In *The Materials Science of Semiconductors* Spinger: Boston, MA, **2008**, p 395-453.

(2) Kelley, T. W.; Baude, P. F.; Gerlach, C.; Ender, D. E.; Muyres, D.; Haase, M. A.; Vogel, D. E.; Theiss, S. D. Recent Progress in Organic Electronics: Materials, Devices, and Processes. *Chemistry of Materials* **2004**, *16*, 4413-4422.

(3) Xu, R.-P.; Li, Y.-Q.; Tang, J.-X. Recent advances in flexible organic light-emitting diodes. *Journal of Materials Chemistry C* **2016**, *4*, 9116-9142.

(4) Hedley, G. J.; Ruseckas, A.; Samuel, I. D. W. Light Harvesting for Organic Photovoltaics. *Chemical Reviews* **2017**, *117*, 796-837.

(5) Torsi, L.; Magliulo, M.; Manoli, K.; Palazzo, G. Organic field-effect transistor sensors: a tutorial review. *Chemical Society Reviews* **2013**, *42*, 8612-8628.

(6) Hamedi, M.; Forchheimer, R.; Inganäs, O. Towards woven logic from organic electronic fibres. *Nature Materials* **2007**, *6*, 357.

(7) Bernards, D. A.; Malliaras, G. G.; Owens, R. M., Eds.;*Organic Semiconductors in Sensor Applications*; Springer: Verlag Berlin, Heidelberg, **2008**; Vol. 107.

(8) Someya, T.; Sekitani, T.; Kaltenbrunner, M.; Yokota, T.; Fuketa, H.; Takamiya, M.; Sakurai, T. In *2013 IEEE International Electron Devices Meeting* 2013, p 8.5.1-8.5.4.

(9) Liu, B., Ed.;*Conjugated Polymers for Biological and Biomedical Applications*; John Wiley & Sons, **2018**.

(10) https://www.oe.phy.cam.ac.uk/research/materials/osemiconductors

(11) Forrest, S. R. The path to ubiquitous and low-cost organic electronic appliances on plastic. *Nature* **2004**, *428*, 911.

(12) Lin, Y.; Li, Y.; Zhan, X. Small molecule semiconductors for high-efficiency organic photovoltaics. *Chemical Society Reviews* **2012**, *41*, 4245-4272.

(13) Usta, H.; Facchetti, A. In *Large Area and Flexible Electronics*; Caironi, M., Noh, Y. Y., Eds.; Wiley-VCH Verlag GmbH & Co. KGaA: **2015**, p 1-100.

(14) Glowacki, E. D.; Irimia-Vladu, M. *Natural and Nature-inspired Materials in Organic Electronics*, SPIE Newsroom, **2012**, doi: 10.1117/2.1201201.004054

(15) McGinness, J.; Corry, P.; Proctor, P. Amorphous semiconductor switching in melanins. *Science* **1974**, *183*, 853-855.

(16) Mostert, A. B.; Powell, B. J.; Pratt, F. L.; Hanson, G. R.; Sarna, T.; Gentle, I. R.; Meredith, P. Role of semiconductivity and ion transport in the electrical conduction of melanin. *Proceedings of the National Academy of Sciences* **2012**, *109*, 8943-8947.

(17) Shan, B.; Miao, Q. Molecular design of n-type organic semiconductors for high-performance thin film transistors. *Tetrahedron Letters* **2017**, *58*, 1903-1911.

(18) Liu, J.; Zhang, H.; Dong, H.; Meng, L.; Jiang, L.; Jiang, L.; Wang, Y.; Yu, J.; Sun, Y.; Hu, W.; Heeger, A. J. High mobility emissive organic semiconductor. *Nature Communications* **2015**, *6*, 10032.

(19) Yuan, Y.; Giri, G.; Ayzner, A. L.; Zoombelt, A. P.; Mannsfeld, S. C.; Chen, J.; Nordlund, D.; Toney, M. F.; Huang, J.; Bao, Z. Ultra-high mobility transparent organic thin film transistors grown by an off-centre spin-coating method. *Nature Communincations* **2014**, *5*, 3005.

(20) Luo, C.; Kyaw, A. K. K.; Perez, L. A.; Patel, S.; Wang, M.; Grimm, B.; Bazan, G. C.; Kramer, E. J.; Heeger, A. J. General Strategy for Self-Assembly of Highly Oriented Nanocrystalline Semiconducting Polymers with High Mobility. *Nano Letters* **2014**, *14*, 2764-2771.

(21) Kang, I.; Yun, H.-J.; Chung, D. S.; Kwon, S.-K.; Kim, Y.-H. Record High Hole Mobility in Polymer Semiconductors via Side-Chain Engineering. *Journal of the American Chemical Society* **2013**, *135*, 14896-14899.

(22) Kim, G.; Kang, S.-J.; Dutta, G. K.; Han, Y.-K.; Shin, T. J.; Noh, Y.-Y.; Yang, C. A Thienoisoindigo-Naphthalene Polymer with Ultrahigh Mobility of 14.4 cm2/V·s That Substantially Exceeds Benchmark Values for Amorphous Silicon Semiconductors. *Journal of the American Chemical Society* **2014**, *136*, 9477-9483.

(23) Quinn, J. T. E.; Zhu, J.; Li, X.; Wang, J.; Li, Y. Recent progress in the development of n-type organic semiconductors for organic field effect transistors. *Journal of Materials Chemistry C* **2017**, *5*, 8654-8681.

(24) Jongwan, C.; Heeseok, S.; Nakjoong, K.; Felix Sunjoo, K. Development of n-type polymer semiconductors for organic field-effect transistors. *Semiconductor Science and Technology* **2015**, *30*, 064002.

(25) Zhang, G.; Zhang, K.; Yin, Q.; Jiang, X.-F.; Wang, Z.; Xin, J.; Ma, W.; Yan, H.; Huang, F.; Cao, Y. High-Performance Ternary Organic Solar Cell Enabled by a Thick Active Layer Containing a Liquid Crystalline Small Molecule Donor. *Journal of the American Chemical Society* **2017**, *139*, 2387-2395.

(26) Deng, D.; Zhang, Y.; Zhang, J.; Wang, Z.; Zhu, L.; Fang, J.; Xia, B.; Wang, Z.; Lu, K.; Ma, W.; Wei, Z. Fluorination-enabled optimal morphology leads to over 11% efficiency for inverted small-molecule organic solar cells. *Nature Communications* **2016**, *7*, 13740.

(27) Holliday, S.; Ashraf, R. S.; Wadsworth, A.; Baran, D.; Yousaf, S. A.; Nielsen, C. B.; Tan, C.-H.; Dimitrov, S. D.; Shang, Z.; Gasparini, N.; Alamoudi, M.; Laquai, F.; Brabec, C. J.; Salleo, A.; Durrant, J. R.; McCulloch, I. High-efficiency and air-stable P3HT-based polymer solar cells with a new non-fullerene acceptor. *Nature Communications* **2016**, *7*, 11585.

(28) Tang, M. L.; Reichardt, A. D.; Wei, P.; Bao, Z. Correlating Carrier Type with Frontier Molecular Orbital Energy Levels in Organic Thin Film Transistors of Functionalized Acene Derivatives. *Journal of the American Chemical Society* **2009**, *131*, 5264-5273.

(29) Yu, J.; Ornelas, J. L.; Tang, Y.; Uddin, M. A.; Guo, H.; Yu, S.; Wang, Y.; Woo, H. Y.; Zhang, S.; Xing, G.; Guo, X.; Huang, W. 2,1,3-Benzothiadiazole-5,6-dicarboxylicimide-Based Polymer Semiconductors for Organic Thin-Film Transistors and Polymer Solar Cells. *ACS Applied Materials & Interfaces* **2017**, *9*, 42167-42178.

(30) Zhang, C.; Zang, Y.; Zhang, F.; Diao, Y.; McNeill, C. R.; Di, C. a.; Zhu, X.; Zhu, D. Pursuing High-Mobility n-Type Organic Semiconductors by Combination of "Molecule-Framework" and "Side-Chain" Engineering. *Advanced Materials* **2016**, *28*, 8456-8462.

(31) d'Ischia, M.; Wakamatsu, K.; Napolitano, A.; Briganti, S.; Garcia-Borron, J. C.; Kovacs, D.; Meredith, P.; Pezzella, A.; Picardo, M.; Sarna, T.; Simon, J. D.; Ito, S. Melanins and melanogenesis: methods, standards, protocols. *Pigment Cell Melanoma Res* **2013**, *26*, 616-633.

(32) d'Ischia, M.; Wakamatsu, K.; Napolitano, A.; Briganti, S.; Garcia-Borron, J.-C.; Kovacs, D.; Meredith, P.; Pezzella, A.; Picardo, M.; Sarna, T.; Simon, J. D.; Ito, S. Melanins and melanogenesis: methods, standards, protocols. *Pigment Cell & Melanoma Research* **2013**, *26*, 616-633.

(33) Meredith, P.; Sarna, T. The physical and chemical properties of eumelanin. *Pigment Cell Res* **2006**, *19*, 572-594.

(34) Prota, G. *Melanins and Melanogenesis*; Academic Press: New York, **1992**.

(35) Borovansky, J.; Riley, P. A.; Borovansky, J., Eds.;*Melanins and Melanosomes : Biosynthesis, Biogenesis, Physiological, and Pathological Functions*; John Wiley & Sons, Incorporated, **2011**.

(36) Solano, F. Melanin and Melanin-Related Polymers as Materials with Biomedical and Biotechnological Applications-Cuttlefish Ink and Mussel Foot Proteins as Inspired Biomolecules. *International Journal of Molecular Sciences* **2017**, *18*.

(37) Mostert, A. B.; Davy, K. J. P.; Ruggles, J. L.; Powell, B. J.; Gentle, I. R.; Meredith, P. Gaseous Adsorption in Melanins: Hydrophilic Biomacromolecules with High Electrical Conductivities. *Langmuir* **2010**, *26*, 412-416.

(38) Tran, M. L.; Powell, B. J.; Meredith, P. Chemical and Structural Disorder in Eumelanins: A Possible Explanation for Broadband Absorbance. *Biophysical Journal* **2006**, *90*, 743-752.

(39) Shosuke, I.; Kazumasa, W. Chemistry of Mixed Melanogenesis—Pivotal Roles of Dopaquinone†. *Photochemistry and Photobiology* **2008**, *84*, 582-592.

(40) d'Ischia, M.; Napolitano, A.; Ball, V.; Chen, C.-T.; Buehler, M. J. Polydopamine and Eumelanin: From Structure–Property Relationships to a Unified Tailoring Strategy. *Accounts of Chemical Research* **2014**, *47*, 3541-3550.

(41) Selvaraju, S.; Niradha Sachinthani, K. A.; Hopson, R. A.; McFarland, F. M.; Guo, S.; Rheingold, A. L.; Nelson, T. L. Eumelanin-inspired core derived from vanillin: a new building block for organic semiconductors. *Chemical Communications* **2015**, *51*, 2957-2959.

CHAPTER II

EFFECTS OF STRUCTURAL VARIATIONS ON THE OPTICAL AND ELECTRONIC PROPERTIES OF EUMELANIN-INSPIRED SMALL MOLECULES

2.1 INTRODUCTION

Melanins are naturally occurring pigmentary macromolecules.[1] In mammals, they are found in the hair, eyes, skin and the brain. Two major types of melanin are pheomelanin and eumelanin.[1-3] It is well-known that eumelanin, the black-brown variety of melanin, results from the oxidative polymerization of two building blocks, 5,6-dihydroxyindole (DHI) and 5,6-dihydroxyindole-2-carboxylic acid (DHICA).[4] Since the groundbreaking discovery that natural and synthetic eumelanins possess semiconducting properties, eumelanin-based materials have gained much attention for use in various applications.[5-13] Recently, Meredith and coworkers reported that melanin is an electronic-ionic hybrid conductor, rather than the amorphous organic semiconductor, which opens up new opportunities in bioelectronics given its biocompatibility. Although the overall composition of eumelanin is reasonably understood, the exact structure remains ambiguous.[14-17] Others have synthesized the undefined eumelanin materials via oxidative polymerization of DHI, DHICA or dopamine.[1] In contrast, a new approach has been employed to elucidate and enhance the optical and electronic properties of natural eumelanin by methodically modifying the structure of a eumelanin-inspired indole core. The work demonstrated that the eumelanin-inspired core, 4,7-dibromo-5,6-dimethoxy-N-methyl-1H-

indole-2-carboxylate (**DBI**), could be utilized as a bioinspired building block for organic semiconductors.[18] Our previous data also suggested that with a suitable substitution on the phenylene ring system, the optoelectronic properties could be tuned.[18] To conduct investigations of the effect of substituents (or structural variations) on the optoelectronic properties of the eumelanin-inspired indole core, five new eumelanin-inspired small molecules were synthesized and differ by the substituents attached to the para position of the phenylene ring. In this chapter, it is demonstrated that different electron withdrawing groups (EWGs) and electron donating groups (EDGs) are effective in manipulating the highest occupied molecular orbital (HOMO), the lowest unoccupied molecular orbital (LUMO), and hence the bandgap. Using a combination of synthetic and computational methods, the tunability of the absorption and emission properties of functional eumelanin-inspired compounds **2a–e** based on the substitution on the phenyl ring was studied. Further, the effect of protonation on the optical properties of the dimethylamino compound **2b** was also investigated.

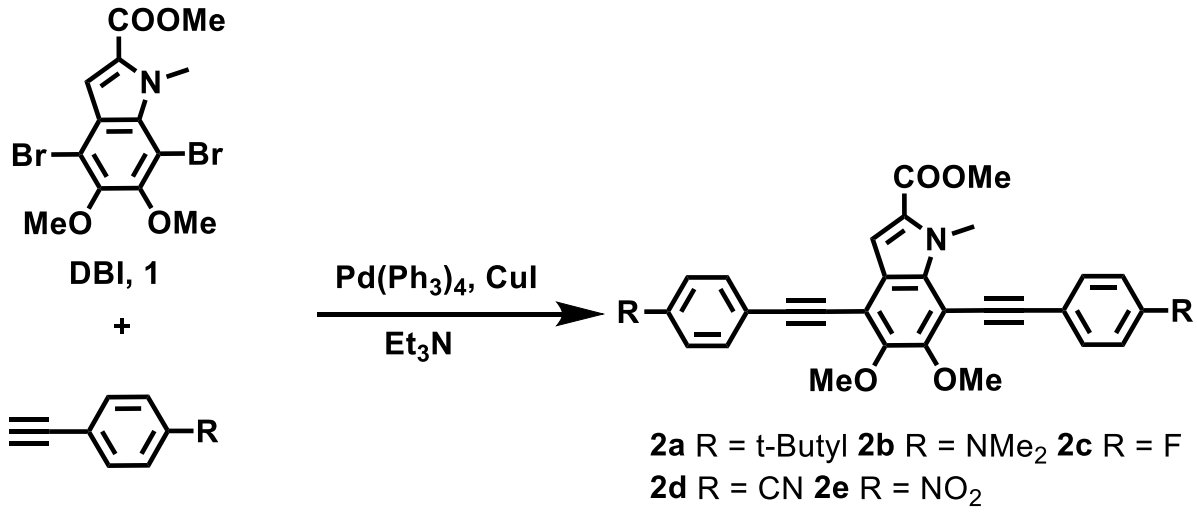

Scheme 2.1: Synthesis of eumelanin-inspired small molecules **2a-e.**

2.2 RESULTS AND DISCUSSION

2.2.1 Synthesis

The synthesis of a series of eumelanin-inspired small molecules whose properties can be tuned based on certain substitution. The 4,7-positions of DBI were functionalized with phenyleneethynylene rings with EWGs and EDGs. Previously, the synthesis of two Eumelanin-inspired small molecules were reported from our laboratory.[18] The syntheses of the derivatives of **1** were achieved by using a similar approach and are shown in Scheme 2.1. The reaction yields ranged from 42% to 99%.

2.2.2 Optical and Electronic Properties

The absorption and emission spectra were taken in $CHCl_3$ solution and are shown in Figure 2.1. The UV-vis absorption and the emission data of the compounds **2a–e** are summarized in Table 2.1. All compounds, except for the unsubstituted DBI core, exhibited two major absorption peaks. The high energy absorption was observed in the range 250–350 nm, while the low energy absorptions were in the range 380–425 nm. The maximum absorption (λ_{max}) increased as the electron-donating strength of the substituent on the phenyl ring increased. The alkyl substituent had the lowest λ_{max} (387 nm), followed by the alkoxy (390 nm) and dimethylamino substituent (415 nm).[18] The same increasing trend was observed in the case of electron-withdrawing groups, that is, as the strength of the substituent on the phenyl increased, an increase in the λ_{max} was observed. The photoluminescence study (Figure 2.1B) displayed a similar trend as the UV-vis spectra in that the stronger EDGs and EWGs exhibited the most red shifted emission versus the weaker EDGs and EWGs. The NMe_2 had the most redshifted emission in the series while NO_2 showed no emissive property. This is not surprising because it is known that NO_2 can quench emission.[19,20] The ϕ_{PL} values for compounds **2a–d** are listed in Table 2.1.

Table 2.1: Optical data of Eumelanin-inspired small molecules.

Compound	λ_{abs}[a] (nm)	ε[a] (M^{-1} cm^{-1})	ϕ_{re}[b]	λ_{ems} (nm)	E_g[c] (eV)
2a	387*, 301, 239	39500	0.77	441	2.92
2b	415*, 310, 239	56600	0.87	476	2.62
2c	382*, 297, 239	4500	0.67	432	2.95
2d	401*, 302, 241	50200	0.65	458	2.77
2e	423*, 304, 280	48200	-	-	2.55

* $\lambda_{max.}$ [a] measure in dilute chloroform. [b] Quantum yields measured in dilute chloroform solutions relative to quinine sulfate. [c] Measured from the tangent drawn at the onset of absorption.

Cyclic voltammetry measurements were carried out in dry degassed acetonitrile under an inert atmosphere using 0.1 M tetrabutylammonium hexafluorophosphate as the supporting electrolyte. The Ag/AgCl reference electrode was calibrated against a ferrocene/ferrocenium (Fc/Fc^+) redox couple. The HOMO and the LUMO energy values were calculated from the onset of the first oxidation and reduction potentials from the equations E_{HOMO} (eV) = [E_{ox}^{onset} - $E_{1/2}$ (Fc/Fc^+) + 4.8] and E_{LUMO} (eV) = [E_{red}^{onset} - $E_{1/2}$ (Fc/Fc^+) + 4.8], where $E_{1/2}$ (Fc/Fc^+) was the cell correction. The lowest bandgap was observed for compounds **2b** ($–NMe_2$) and **2e** ($–NO_2$). In both cases the bandgap values were 2.15 eV. The same was observed in the case of the optical bandgap where both **2b** and **2e** had lower optical bandgaps in the series. It was noted that **2e** had the strongest EWG substituent; and **2b** had the strongest EDG in the series. As expected, it was observed that in the case of **2b**, the HOMO was higher and in **2e** the LUMO was lower and both resulted in smaller bandgaps. Other substituents, like t-butyl (**2a**) and F (**2c**), exhibited similar data as **H**. Compound **2d** showed a reduction in the bandgap but not as significant as in **2b** and **2e**. The

HOMO and LUMO values calculated for compounds **DBI**, R = **H**, **OMe**, and **2a–e** from the CV experiments are shown in Figure 2.2, along with **H** and **OMe** previously reported.[18]

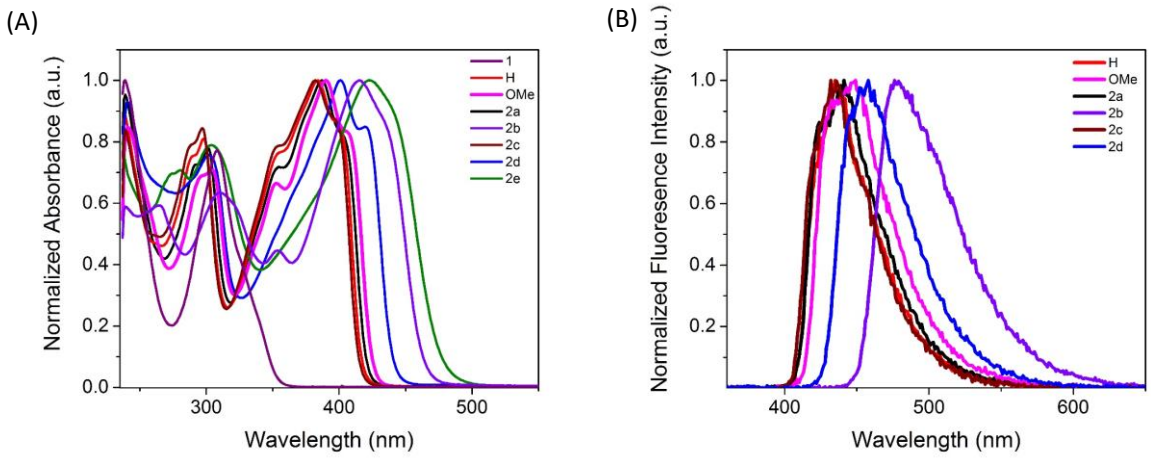

Figure 2.1: A) UV-vis absorption spectra and B) Emission spectra of compounds **1** (DBI)*, R = **H***, **OMe*** and compounds **2a –e**. *Note: these compounds have been previously reported.[18]

Optimized equilibrium structures were obtained using Density Functional Theory (DFT).[21] In all cases, the B3LYP exchange–correlation functional[22,23] and the 6-311G(d) basis set as implemented in the Gaussian 09 package were employed.[24,25] The optimized geometries were also verified through the vibration frequency studies. Second, the molecular orbital densities of HOMOs and LUMOs were calculated with the same functional and the more accurate 6-311G(2d) basis set.[26] The frontier orbitals for all compounds are presented in Figure 2.2, while compounds **2b** and **2e** are shown in Figure 2.3. Compounds **2b** and **2e** were chosen as they exhibited the strongest EDG and EWG capacities in the series. It can be seen that in the HOMO of **2b**, the electron density is mostly distributed along the phenyleneethynylene conjugated system, and in the LUMO they are more localized along the indolylene ring. However, in the case of **2e**, the electron density is more localized along the indolylene axis in the HOMO, while in the LUMO, it is delocalized along the phenyleneethynylene axis bearing the NO_2 substituent. The LUMO and optical bandgaps were obtained from time-dependent density functional theory

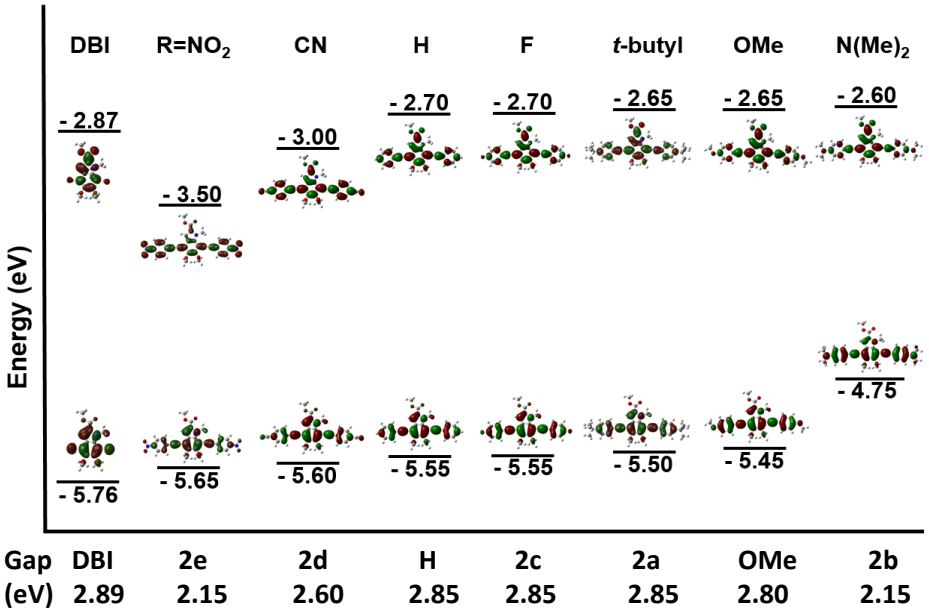

Figure 2.2: HOMO and LUMO levels obtained from CV measurements and frontier molecular orbitals for Eumelanin-inspired small molecules.

(TDDFT)[27] utilizing the first 20 excited states of each compound. A linear correlation between the calculated and experimental values was carried out to correct the theoretical values found.[28] A comparison of the HOMO and LUMO values for **2a–e**, R= **MeO** and **H** from cyclic voltammetry experiments and computational studies are given in Table 2.2. It was found that DFT is well suited to predict the energy values for HOMOs, with the biggest deviation being 6.2%. As expected, the LUMO and optical gap values obtained from DFT are inaccurate for the compounds studied. However, TD-DFT calculations for the energetics of the LUMO correlated well with experimental measurements. Here, the largest difference was below 5.2%. Errors in HOMO–LUMO gaps range from 0.15 to 0.41 eV. Although the accuracy of *ab initio* calculations depends on the level of theory employed, a small deviation between theory and the experiment demonstrates that these methods (DFT + TDDFT) can be useful in the prediction of the eigenvalues of molecular orbitals of eumelanin-inspired conjugated molecules.

Table 2.2: Experimental and theoretical comparison of the electronic level of Eumelanin-inspired small molecules.

		H	**OCH_3**	**2a**	**2b**	**2c**	**2d**	**2e**
HOMO (eV)	Expt.	-5.55	-5.45	-5.50	-4.75	-5.55	-5.60	-5.65
	Theory	-5.44	-5.27	-5.37	-5.05	-5.47	-5.73	-5.77
	Dev. (%)	2.00	3.36	2.39	6.12	1.45	2.29	2.10
LUMO (eV)	Expt.	-2.70	-2.65	-2.65	-2.60	-2.70	-3.00	-3.50
	Theory	-2.74	-2.62	-2.69	-2.49	-2.78	-3.16	-3.33
	Dev. (%)	1.47	1.14	1.150	4.32	2.92	5.19	4.98
GAP (eV)	Expt.	2.85	2.80	2.85	2.15	2.85	2.60	2.15
	Theory	2.70	2.65	2.68	2.56	2.69	2.57	2.44
	Dev. (%)	5.41	5.50	6.15	17.41	5.78	1.16	12.64

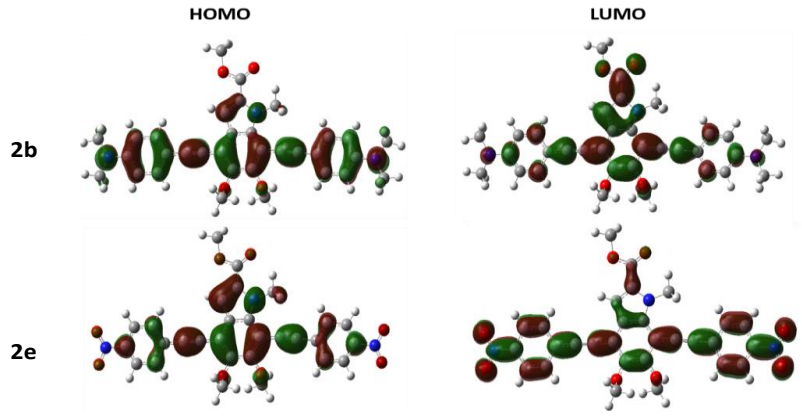

Figure 2.3: Frontier molecular orbitals of compounds **2b** and **2e**.

2.2.3 Acidochromic Sensor

Among the different small molecules, compound **2b** was chosen in order to study the optical response to protonation with trifluoroacetic acid (TFA) in view of the presence of the basic *N*,*N*-dimethylamino group directly connected to the conjugated system. Furthermore, the protonation of the dimethylamino group change from an EDG to an EWG, which completely alters the optical and electronic properties. Such studies could be vital in establishing this molecule as an ideal chemosensor. All experiments for optical responses to protonation with the addition of TFA were performed in dilute $CHCl_3$ solution, and the results are displayed in Figure 2.4. The absorption spectra exhibited a blue shifted absorbance at 415 nm with the addition of TFA. These changes are attributed to the stabilization of the HOMO level due to the protonation of the *N*,*N*-dimethylamino group. Similarly, the emission spectra were also blue-shifted at high TFA concentrations (log [TFA] = 2.05). Fluorescence quenching was also observed in the emission spectra with the addition of TFA.

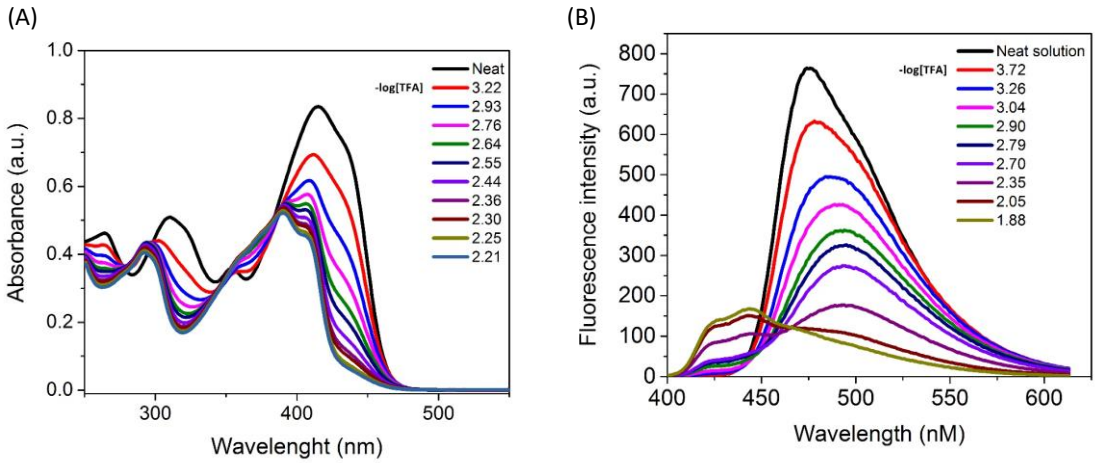

Figure 2.4: Optical response towards the protonation of *2b* in the presence of TFA: A) absorption spectra and B) emission spectra.

The optical changes at high concentration of TFA were visible to the naked eye and found to be reversible upon addition of ammonia as displayed in Figure 2.5A. At a low concentration of TFA (0.18 mM to 2.16 mM), the fluorescence quenching data correlated well in terms of the standard Stern–Volmer relationship (equation 1) with the Stern–Volmer constant being 8.6 x 10^2 $Lmol^{-1}$ (Figure 2.5B). Such a phenomenon marks this system as a potential acidochromic sensor.

$$\frac{F_o}{F} = 1 + Ksv[Q] \qquad (1)$$

Where F_o and F are the emission intensities of compound **2b** without and with TFA. *Ksv* is quenching constant and [Q] is the molar concentration of quencher.

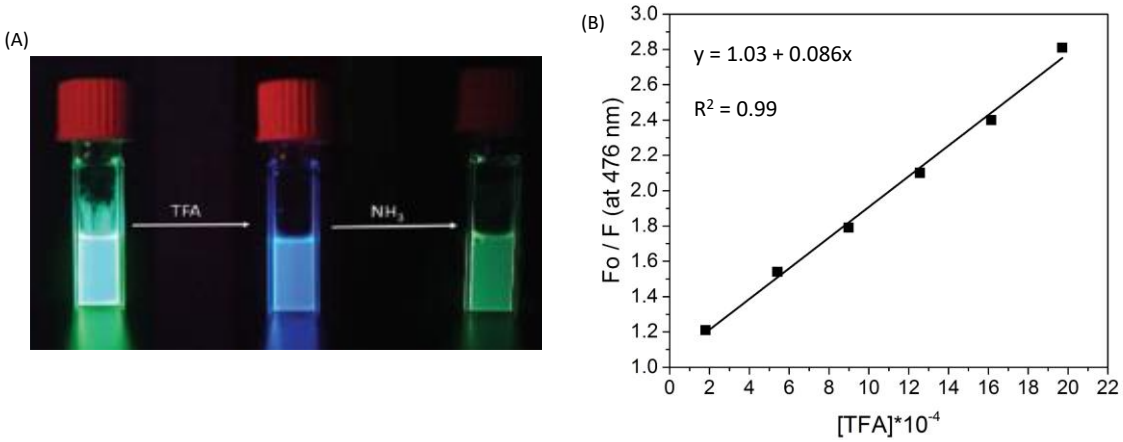

Figure 2.5: A) Emission of **2b** in chloroform (left cuvette, green emission), upon addition of a large excess of TFA (center cuvette, blue emission), and upon addition of a large excess of NH_3 (right cuvette, green emission) and B) Stern-Volmer plot for the data from Figure 2.4B.

2.3 CONCLUSION

In summary, five new eumelanin-inspired conjugated molecules were synthesized by changing the functional group at the para position of the phenyleneethynylene ring. These five molecules were compared to two previously synthesized conjugated structures in an effort to explore the effect of structural variations (electron withdrawing and donating groups) on the optoelectronic

properties of the eumelanin-inspired indole core. It was demonstrated that the substituents can alter the electronic characteristics of these molecules, hence changing their optoelectronic properties. Furthermore, the optical response of compound **2b** to acid was studied and the data suggest that it could act as an acidochromic sensor due to its unique chromic response when exposed to TFA. This work demonstrates the utility of the eumelanin-inspired indole core and opens up the possibility of designing materials with interesting properties for specific applications by decorating this core with various functionalities. Moreover, this work brings the field one step closer to elucidating and enhancing the properties of the naturally occurring eumelanin.

2.4 EXPERIMENTAL SECTION

2.4.1 General Methods and Materials

All commercial reagents were used as received. Et_3N was re-distilled before use. Para-substituted phenylacetylenes were synthesized according to the previously reported procedure.[29] Unless otherwise specified, all reactions were run in oven-dried glassware. Reactions were monitored by thin layer chromatography on silica G TLC plates (Sorbent Technologies No. 1634126). Purifications were performed by column chromatography on silica gel (Sorbent Technologies, 40-63 μm particle size) or neutral alumina (Sorbent Technologies, 32-63 μm particle size). ^{1}H and ^{13}C NMR spectra were measured on a Bruker Avance 400 MHz instrument. Elemental analyses were performed by Atlantic Microlab, Inc., Norcross, GA 30071. Cyclic voltammetry was performed on a CH-instruments 6017E model with 0.1 M tetrabutylammonium hexafluorophosphate as the supporting electrolyte in dry acetonitrile using glassy carbon as the working electrode, platinum wire as counter electrode and Ag/AgCl as the reference electrode with a scan rate of 100 mV/sec. The HOMO and LUMO energy values were calculated from the onset of the first oxidation and reduction potentials from the equations E_{HOMO} (eV) = [E_{ox}^{onset} - $E_{1/2}(Fc/Fc^+)$ + 4.8] and E_{LUMO} (eV) = - [E_{red}^{onset} - $E_{1/2}$ (Fc/Fc^+) + 4.8], where $E_{1/2}$ (Fc/Fc^+) was the

cell correction. Melting points were obtained using a melting point apparatus, upper temperature limit 400 °C. UV-vis spectra were recorded on a Cary 5000 UV-VIS-NIR spectrophotometer. Fluorescence spectra were recorded on a Cary Eclipse fluorescence spectrophotometer. Fluorescence and UV-vis measurements were taken in $CHCl_3$. The optical bandgap was calculated from the wavelength corresponding to the energy absorption onset from the intersection of the leading edge tangent with the x-axis. Quantum yield measurements were performed in dilute $CHCl_3$ solutions with absorbance ranging from 0.01 to 0.04. Quinine sulfate was used as the reference. The excitation wavelength of 313 nm was used to obtain the fluorescence spectra for each solution ranging from 320 to 600 nm. The fluorescence intensity (area of the fluorescence spectrum) was then calculated and recorded. Quantum yields were calculated using the following equation:[30] $\phi s = \phi r \left(\frac{A_r F_s}{A_s F_r}\right)\left(\frac{n_s^2}{n_r^2}\right)$, where ϕr is 0.51, *As* and *Ar* are absorbance of the sample and reference solutions, respectively at the same excitation wavelength, *Fs* and *Fr* are the corresponding relative integrated fluorescence intensities, n is the refractive index [$CHCl_3$ (n_s = 1.445) and 1 N H_2SO_4 (n_r = 1.339) were used]. A Bruker Ultra diffractometer equipped with a mini rotating-anode Mo source and microfocus optics was used for data collection with one-second, one-degree width images. Direct methods were used for structure solution and all non-hydrogen atoms were refined with anisotropic thermal parameters and without restraint. Hydrogen atoms were included as idealized contributions. All software was contained in the current packages of SHELX software as provided by the Bruker Corporation (Madison, WI).

2.4.2 Synthesis

Synthesis of **2a**: In a 8-mL reaction vial, compound **1** (50 mg, 0.123 mmol) was placed under an argon atmosphere, $Pd(PPh_3)_4$ (7.0 mg, 5 mol%), CuI (0.57 mg, 0.003 mmol), Et_3N (2 mL) and 4-*tert*-butylphenylacetylene (50.61 mg, 0.32 mmol) were added and the vial was sealed. The

reaction was heated to 80 °C for a period of 16 h. After 16 h the solvent was evaporated. The resulting residue was purified by column chromatography using alumina column using Hexane/EtOAc (98:2) to afford the yellow solid in 87%. Mp 190–192 °C. ^{1}H NMR (400 MHz, $CDCl_3$) δ 7.62 – 7.48 (m, 4H), 7.46 – 7.37 (m, 5H), 4.55 (s, 3H), 4.05 (d, *J* = 0.8 Hz, 6H), 3.92 (s, 3H), 1.34 (d, *J* = 1.2 Hz, 18H). ^{13}C NMR (101 MHz, $CDCl_3$) δ 162.26, 154.80, 152.17, 150.14, 134.52, 131.60, 130.98, 128.94, 125.67, 125.53, 124.55, 120.41, 120.38, 111.08, 110.65, 103.50, 100.07, 98.85, 82.96, 82.47, 61.90, 61.82, 51.83, 35.01, 34.99, 33.73, 31.32, 31.30. Elemental Anal. Calcd. for $C_{37}H_{39}NO_4$: C, 79.12; H, 7.00; N, 2.49. Found: C, 78.68; H, 7.02; N, 2.54.

Synthesis of compound **2b**: This compound was prepared using the procedure reported for **2a** (yellow solid, 42% yield). Mp 196–198 °C ^{1}H NMR (400 MHz, $CDCl_3$) δ 7.55 – 7.39 (m, 5H), 6.74 – 6.65 (m, 4H), 4.56 (s, 3H), 4.04 (d, *J* = 1.0 Hz, 6H), 3.91 (s, 3H), 3.02 (d, *J* = 0.9 Hz, 12H). ^{13}C NMR (101 MHz, CDCl3) δ 162.26, 154.24, 150.30, 150.26, 149.56, 134.43, 132.90, 132.21, 128.49, 124.25, 111.89, 111.80, 110.94, 110.71, 110.21, 110.15, 103.39, 101.07, 99.96, 81.74, 81.13, 61.68, 61.61, 51.63, 40.23, 40.21, 33.62 Elemental Anal. Calcd. for $C_{33}H_{33}N_3O_4$ $0.1H_2O$: C, 73.75; H, 6.23; N, 7.82. Found: C, 73.51; H, 6.33; N, 7.72.

Synthesis of compound **2c**: This compound was prepared using the procedure reported for **2a** (yellow solid, 99 % yield). Mp 129–131 °C. ^{1}H NMR (400 MHz, $CDCl_3$) δ 7.67 – 7.50 (m, 4H), 7.41 (s, 1H), 7.15 – 7.04 (m, 4H), 4.54 (s, 3H), 4.05 (d, *J* = 2.7 Hz, 6H), 3.93 (s, 3H). ^{13}C NMR (101 MHz, $CDCl_3$) δ 163.99, 162.05, 161.48, 154.73, 150.08, 134.33, 133.69, 133.61, 133.05, 132.97, 129.01, 124.36, 119.34, 116.03, 115.86, 115.81, 115.64, 110.84, 110.37, 103.20, 98.68, 97.42, 83.09, 82.61, 61.80, 61.72, 51.77, 33.61. Elemental Anal. Calcd. for $C_{29}H_{21}F_2NO_4$ $0.15Et_2O$: C, 71.59; H, 4.57; N, 2.82. Found: C, 71.66; H, 4.92; N, 2.71.

Synthesis of compound **2d**: This compound was prepared using the procedure reported for **2a** (yellowish-orange solid, 57 % yield). Mp 150–152 °C ^{1}H NMR (400 MHz, $CDCl_3$) δ 7.74 – 7.61

(m, 8H), 7.40 (s, 1H), 4.54 (s, 3H), 4.05 (d, *J* = 3.9 Hz, 6H), 3.94 (s, 3H). ^{13}C NMR (101 MHz, $CDCl_3$) δ 161.89, 155.05, 150.49, 134.72, 132.29, 132.21, 132.15, 129.48, 127.96, 127.87, 124.41, 118.47, 118.38, 111.99, 111.91, 110.90, 110.18, 103.20, 98.20, 96.92, 87.64, 87.26, 61.95, 61.88, 51.93, 33.70. Elemental Anal. Calcd. for $C_{31}H_{21}N_3O_4$ 0.5$CHCl_3$: C, 67.66; H, 3.88; N, 7.51. Found: C, 67.70; H, 4.10; N, 7.65.

Synthesis of compound **2e**: This compound was prepared using the procedure reported for **2a** (orange solid, 56 % yield). Mp 248–250 °C ^{1}H NMR (400 MHz, $CDCl_3$) δ 8.32 – 8.23 (m, 4H), 7.82 – 7.74 (m, 2H), 7.75 – 7.67 (m, 2H), 7.42 (s, 1H), 4.56 (s, 3H), 4.07 (d, *J* = 4.5 Hz, 6H), 3.95 (s, 3H). ^{13}C NMR (101 MHz, $CDCl_3$) δ 161.85, 155.13, 150.58, 147.26, 134.20, 132.43, 131.75, 129.90, 129.80, 129.57, 124.43, 123.90, 123.75, 110.96, 110.16, 103.23, 98.06, 96.75, 88.52, 88.15, 61.98, 61.91, 51.94, 33.71. Elemental Anal. Calcd. for $C_{29}H_{21}N_3O_8$: C, 64.56; H, 3.92; N, 7.79. Found: C, 64.39; H, 3.88; N, 7.88.

2.4.3 Crystal structures

Crystals were formed by the vapor diffusion technique. The 10 mg each compound was first dissolved in DCM and filtered into the small vial to get rid of any insoluble impurities. The vial was capped with the rubber septum having small pores to diffuse vapor of more volatile solvent. The vial was then placed on the larger vial containing pentane solvent. The larger vial was capped well and sealed with electrical tape and left for recrystallization. All the reported crystals were formed after 24 hours.

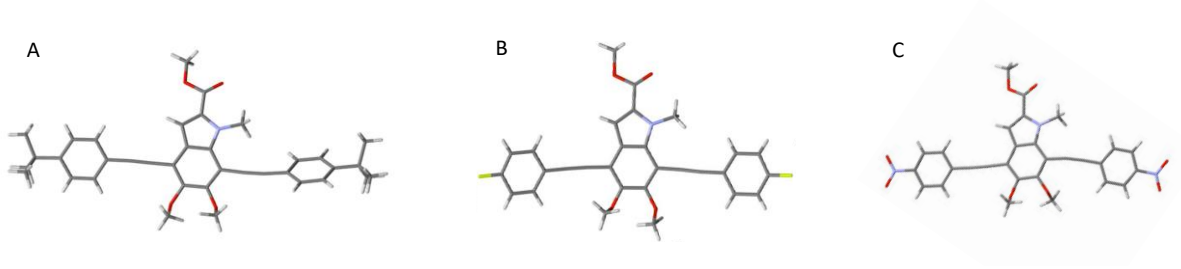

Figure 2.6: Crystal structure of A) **2a**, B) **2c**, and C) **2e**.

2.5 REFERENCES

(1) Prota, G. *Melanins and Melanogenesis*; Academic Press: New York, **1992**.

(2) Alessandro Pezzella, J. W. *Organic Electronics: Emerging Concepts and Technologies*; Wiley-VCH Verlag GmbH & Co. KGaA: Weinheim, Germany, **2013**.

(3) d'Ischia, M.; Wakamatsu, K.; Napolitano, A.; Briganti, S.; Garcia-Borron, J.-C.; Kovacs, D.; Meredith, P.; Pezzella, A.; Picardo, M.; Sarna, T.; Simon, J. D.; Ito, S. Melanins and melanogenesis: methods, standards, protocols. *Pigment Cell & Melanoma Research* **2013**, *26*, 616-633.

(4) Meredith, P.; Sarna, T. The physical and chemical properties of eumelanin. *Pigment Cell Res* **2006**, *19*, 572-594.

(5) Wünsche, J.; Cardenas, L.; Rosei, F.; Cicoira, F.; Gauvin, R.; Graeff, C. F. O.; Poulin, S.; Pezzella, A.; Santato, C. In Situ Formation of Dendrites in Eumelanin Thin Films between Gold Electrodes. *Advanced Functional Materials* **2013**, *23*, 5591-5598.

(6) Friedman, S. L.; Roll, F. J.; Boyles, J.; Bissell, D. M. Hepatic lipocytes: the principal collagen-producing cells of normal rat liver. *Proceedings of the National Academy of Sciences of the United States of America* **1985**, *82*, 8681-8685.

(7) Strube, O. I.; Büngeler, A.; Bremser, W. Site-Specific In Situ Synthesis of Eumelanin Nanoparticles by an Enzymatic Autodeposition-Like Process. *Biomacromolecules* **2015**, *16*, 1608-1613.

(8) McQueenie, R.; Sutter, J.; Karolin, J.; Birch, D. J. Eumelanin fibrils. *Journal of Biomedical Optics* **2012**, *17*, 075001.

(9) Mula, G.; Manca, L.; Setzu, S.; Pezzella, A. Photovoltaic properties of PSi impregnated with eumelanin. *Nanoscale Research Letters* **2012**, *7*, 377-377.

(10) Kim, Y. J.; Wu, W.; Chun, S.-E.; Whitacre, J. F.; Bettinger, C. J. Biologically derived melanin electrodes in aqueous sodium-ion energy storage devices. *Proceedings of the National Academy of Sciences* **2013**, *110*, 20912-20917.

(11) Belitsky, J. M.; Ellowitz, M. Z.; Lye, D.; Kilbo, A. L. Small molecule modulators of aggregation in synthetic melanin polymerizations. *Bioorganic & Medicinal Chemistry Letters* **2012**, *22*, 5503-5507.

(12) Belitsky, J. M.; Lye, D. S.; Gittleman, H. R.; Gorlin, T. A.; Gorham, A. N.; Moore, C. A.; Chaves, M. B.; Ellowitz, M. Z. Colorimetric metal ion binding of catechol-based coatings inspired by melanin and molecular imprinting. *Supramolecular Chemistry* **2014**, *26*, 233-244.

(13) Schweitzer, A. D.; Revskaya, E.; Chu, P.; Pazo, V.; Friedman, M.; Nosanchuk, J. D.; Cahill, S.; Frases, S.; Casadevall, A.; Dadachova, E. Melanin-Covered Nanoparticles for Protection of Bone Marrow During Radiation Therapy of Cancer. *International Journal of Radiation Oncology • Biology • Physics*, *78*, 1494-1502.

(14) Mostert, A. B.; Powell, B. J.; Pratt, F. L.; Hanson, G. R.; Sarna, T.; Gentle, I. R.; Meredith, P. Role of semiconductivity and ion transport in the electrical conduction of melanin. *Proceedings of the National Academy of Sciences* **2012**, *109*, 8943-8947.

(15) Mostert, A. B.; Davy, K. J. P.; Ruggles, J. L.; Powell, B. J.; Gentle, I. R.; Meredith, P. Gaseous Adsorption in Melanins: Hydrophilic Biomacromolecules with High Electrical Conductivities. *Langmuir* **2010**, *26*, 412-416.

(16) Mostert, A. B.; Powell, B. J.; Gentle, I. R.; Meredith, P. On the origin of electrical conductivity in the bio-electronic material melanin. *Applied Physics Letters* **2012**, *100*, 093701.

(17) Mostert, A. B.; Hanson, G. R.; Sarna, T.; Gentle, I. R.; Powell, B. J.; Meredith, P. Hydration-Controlled X-Band EPR Spectroscopy: A Tool for Unravelling the Complexities of the Solid-State Free Radical in Eumelanin. *The Journal of Physical Chemistry B* **2013**, *117*, 4965-4972.

(18) Selvaraju, S.; Niradha Sachinthani, K. A.; Hopson, R. A.; McFarland, F. M.; Guo, S.; Rheingold, A. L.; Nelson, T. L. Eumelanin-inspired core derived from vanillin: a new building block for organic semiconductors. *Chemical Communications* **2015**, *51*, 2957-2959.

(19) Donnelly, V. M.; Keil, D. G.; Kaufman, F. Fluorescence lifetime studies of NO2. III. Mechanism of fluorescence quenching. *The Journal of Chemical Physics* **1979**, *71*, 659-673.

(20) Braslavsky, S.; Heicklen, J. Quenching of the fluorescence of NO2. *Journal of Photochemistry* **1972**, *1*, 203-223.

(21) Kohn, W. *Density Functional Theory*; Springer US, NY, **1995**.

(22) Becke, A. D. Density-functional thermochemistry. III. The role of exact exchange. *The Journal of Chemical Physics* **1993**, *98*, 5648-5652.

(23) Lee, C.; Yang, W.; Parr, R. G. Development of the Colle-Salvetti correlation-energy formula into a functional of the electron density. *Physical Review B* **1988**, *37*, 785-789.

(24) Francl, M. M.; Pietro, W. J.; Hehre, W. J.; Binkley, J. S.; Gordon, M. S.; DeFrees, D. J.; Pople, J. A. Self-consistent molecular orbital methods. XXIII. A polarization-type basis set for second-row elements. *The Journal of Chemical Physics* **1982**, *77*, 3654-3665.

(25) Frisch, M. J.; Trucks, G. W.; Schlegel, H. B.; Scuseria, G. E.; Robb, M. A.; Cheeseman, J. R.; Scalmani, G.; Barone, V.; Petersson, G. A.; Nakatsuji, H.; Li, X.; Caricato, M.; Marenich, A. V.; Bloino, J.; Janesko, B. G.; Gomperts, R.; Mennucci, B.; Hratchian, H. P.; Ortiz, J. V.; Izmaylov, A. F.; Sonnenberg, J. L.; Williams; Ding, F.; Lipparini, F.; Egidi, F.; Goings, J.; Peng, B.; Petrone, A.; Henderson, T.; Ranasinghe, D.; Zakrzewski, V. G.; Gao, J.; Rega, N.; Zheng, G.; Liang, W.; Hada, M.; Ehara, M.; Toyota, K.; Fukuda, R.; Hasegawa, J.; Ishida, M.; Nakajima, T.; Honda, Y.; Kitao, O.; Nakai, H.; Vreven, T.; Throssell, K.; Montgomery Jr., J. A.; Peralta, J. E.; Ogliaro, F.; Bearpark, M. J.; Heyd, J. J.; Brothers, E. N.; Kudin, K. N.; Staroverov, V. N.; Keith, T. A.; Kobayashi, R.; Normand, J.; Raghavachari, K.; Rendell, A. P.; Burant, J. C.; Iyengar, S. S.; Tomasi, J.; Cossi, M.; Millam, J. M.; Klene, M.; Adamo, C.; Cammi, R.; Ochterski, J. W.; Martin, R. L.; Morokuma, K.; Farkas, O.; Foresman, J. B.; Fox, D. J. Wallingford, CT, 2016.

(26) Bérubé, N.; Gosselin, V.; Gaudreau, J.; Côté, M. Designing Polymers for Photovoltaic Applications Using ab Initio Calculations. *The Journal of Physical Chemistry C* **2013**, *117*, 7964-7972.

(27) Runge, E.; Gross, E. K. U. Density-Functional Theory for Time-Dependent Systems. *Physical Review Letters* **1984**, *52*, 997-1000.

(28) Zhang, G.; Musgrave, C. B. Comparison of DFT Methods for Molecular Orbital Eigenvalue Calculations. *The Journal of Physical Chemistry A* **2007**, *111*, 1554-1561.

(29) Dutta, U.; Maity, S.; Kancherla, R.; Maiti, D. Aerobic Oxynitration of Alkynes with tBuONO and TEMPO. *Organic Letters* **2014**, *16*, 6302-6305.

(30) Crosby, G. A.; Demas, J. N. Measurement of photoluminescence quantum yields. Review. *The Journal of Physical Chemistry* **1971**, *75*, 991-1024.

Contribution by the author: In this work, the author synthesized and characterized a couple of eumelanin-inspired small molecules and prepared the crystals of the molecules and performed acidochromic experiments.

CHAPTER III

EUMELANIN-INSPIRED ANTIMICROBIAL WITH BIOCIDAL ACTIVITY AGAINST METHICILLIN RESISTANT *STAPHYLOCOCCUS AUREUS*

3.1. INTRODUCTION

Bacterial antibiotic resistance is a serious threat worldwide significantly impacting human health.[1] As more pathogens develop resistance to antibiotics, standard treatments decrease in their efficacy, infections become more difficult or impossible to control**,** and the risk of spreading infections to others greatly increases. Resistant pathogens have significant impact on patient morbidity and mortality as well as increased economic costs associated with treatment.[2] Resistance, as arisen due to misuse of drugs, has generated a number of resistant bacterial strains that have rendered many clinically relevant antibiotics ineffective against drug-resistant bacteria,[3,4] particularly methicillin resistant *Staphylococcus aureus* (MRSA).[5-8] Much research that focused on identifying novel antibiotics to combat drug resistant strains such as antimicrobial compounds that can coat surfaces and decrease transmission rates are of paramount importance.

Many therapies against antibiotic resistant bacteria have centered on the development of certain antimicrobials**,** including rigid photosensitizer molecules and macromolecules that are irradiated under ultraviolet[9,10] and visible light[11,12] to generate singlet oxygen. To improve biocompatibility, it would be advantageous to develop new antimicrobials that are inspired by nature**,** especially since it offers a rich toolbox of functional and chemically diverse building blocks.

One such inspiration is a class of biomacromolecular pigments, melanins, which gives rise to all coloration of hair, skin, and eyes in humans and animals[13-18] and can act as a natural sunscreen to protect against harmful UV light.[19,20] The black-brown variety of melanin, eumelanin, is known to be composed 5,6-dihydroxyindole and 5,6-dihydroxyindole 2-carboxylic acid.[19,21-24] Biocompatible, biodegradable and peculiar physicochemical properties of eumelanin has branded it as a promising material in medicine and bioelectronics.[25,26]

Among many functions and properties, eumelanin possesses an intrinsic antimicrobial activity.[27,2] From our lab, the synthesis of an eumelanin-inspired indole core, methyl 4,7-dibromo-5,6-dimethoxy-1-methyl-1*H*-indole-2-carboxylate (DBI) was reported, and in Chapter 2, it was shown that the optoelectronic properties of BDI can be tuned by decorating 4- and 7-positions with different functional groups.[29,30] In this chapter, the antimicrobial activity of eumelanin-inspired indole core (DBI) and the synthesis and enhanced antimicrobial activities of eumelanin-inspired indoylenephenyleneethynylene, EIPE-1 will be discussed (Scheme 1).

3.2 RESULTS AND DISCUSSION

3.2.1 Antimicrobial Activity of Eumelanin Inspired Core (DBI)

To evaluate if the eumelanin-inspired indole core (DBI) maintained its intrinsic antimicrobial activity, DBI was tested against *S. aureus* and *P. aeruginosa*. The eumelanin-inspired core was found to retain its intrinsic antimicrobial activity against *S. aureus* (Figure 3.1). A *S. aureus* bacterial culture was grown overnight and subcultured (1 mL into 10 mL of Mueller Hinton Broth) to which either DMSO or DBI was added. After 4 h of growth, the resulting cultures were plated onto mannitol salts agar (MSA). Decreased bacterial growth and decreased fermentation of the mannitol (retention of the reddish hue of the MSA plate) could be seen in the *S. aureus* culture exposed to DBI.

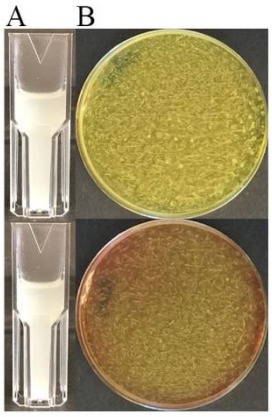

Figure 3.1: Antimicrobial effects of DBI on *S. aureus*. (A) Resulting bacterial growth of *S. aureus* measured by turbidity in cuvettes and (B) recoverable growth on MSA when exposed to DMSO (top) or DBI (bottom).

3.2.2 Synthesis of EIPE-1

In order to enhance the intrinsic antimicrobial efficacy of the eumelanin-inspired indole core (**DBI**) against pathogenic bacteria, two bacterial targeting sites were incorporated to generate eumelanin-inspired indoylenephenyleneethynylene (EIPE-1). Initially, EIPE-1 was prepared by following the synthetic route depicted in Scheme 3.1. The synthesis of compound *4 via* Sonogashira coupling reaction between DBI and compound **3** result in the impure desired product which was very difficult to purify. Further, the methylation of the impure compound **4** was not successful in improving purification of EIPE-1. Thus, an alternate route depicted in Scheme 3.2.was developed and conducted for the the synthesis of EIPE-1. The synthesis of EIPE-1 was conducted by Sonogashira coupling of DBI with trimethylsilylacetylene, followed by a deprotection to yield the diacetylene compound **5** in 65 % yield. The arms of the EIPE-1 were constructed by reacting *p*-bromophenol with 3-chloro-*N*,*N*-dimethylpropan-1-amine hydrochloride under basic conditions to afford compound **2** in 88 % yield. Compounds **2** and **5** were coupled under Sonogashira coupling conditions followed by *N*-methylation with methyl iodide to afford EIPE-1 in 36 % yield.

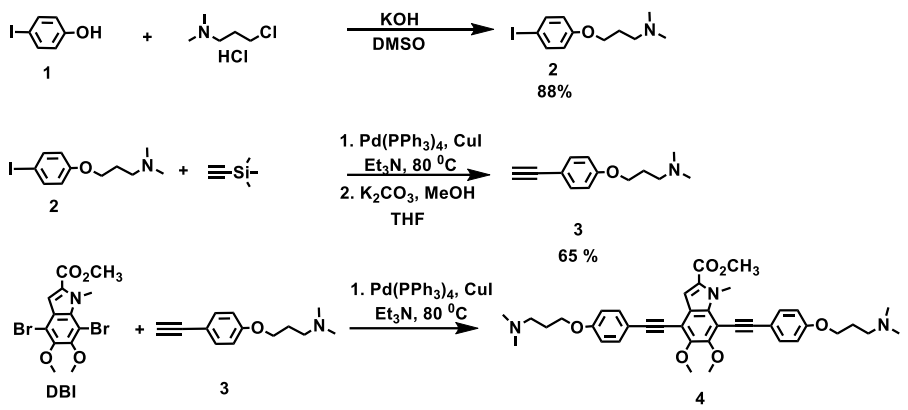

Scheme 3.1: Attempted synthesis of eumelanin-inspired antimicrobial **(**EIPE-1**).**

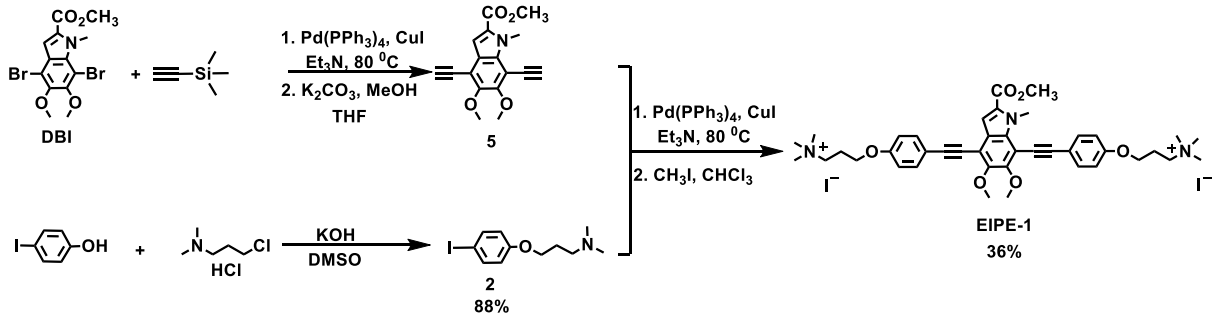

Scheme 3.2: Synthesis of eumelanin-inspired antimicrobial (EIPE-1).

EIPE-1 structure and purity was confirmed by NMR and HRMS analysis along with a melting point determination. The incorporated bacterial targeting sites were expected to have the same antibiotic mechanism against bacterial cells as Triton B, polymyxins and other cationic detergents.[31,32] These systems target the stability the bacterial outer membrane resulting in lysis and ultimately death of the bacterial cell.

3.2.3 Antimicrobial Activity of EIPE-1

The efficacy of compound EIPE-1 was tested by the Kirby-Bauer disc assay.[33] The Kirby-Bauer assay assesses the sensitivity of bacteria to antimicrobial agents. If the bacteria are sensitive to

the antimicrobial being tested, then a zone of inhibition of bacterial growth is seen around the filter disc containing the antimicrobial. The Kirby-Bauer assay was used to test the antimicrobial efficacy of EIPE-1 against *S. aureus*. EIPE-1 was reconstituted at 1 mg/mL in DMSO and serially diluted (10^{-1} to 10^{-5}) after which 10 µL of each dilution (and DMSO as a solvent control) was added to a separate disc on an LB plate inoculated with a lawn of bacteria. The plates were incubated at 37 ˚C for 24 h, and the resulting radii zone sizes around each disc were then measured. The newly generated EIPE-1 compound was observed to inhibit *S. aureus* growth as can be seen by zones of clearing around the discs displayed in Figure 3.2 for concentrations of 1.0 mg/mL, 0.1 mg/mL and 0.01 mg/mL. EIPE-1 was not effective against Gram-negative bacteria. The solvent negative control, DMSO, did not affect growth of *S. aureus* (Figure 3.2F). These experiments demonstrated that EIPE-1 has antimicrobial activity against *S. aureus* (Figure 3.2).

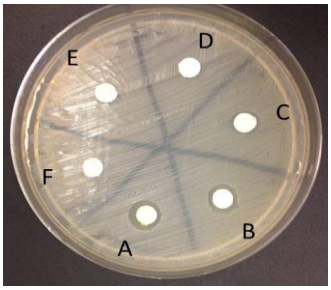

Figure 3.2: Kirby-Bauer disc assay. *S. aureus* was inoculated as a bacterial lawn and 10 µL of EIPE-1 added at (A) 1.0 mg/mL (B), 0.1 mg/mL (C) 0.01 mg/mL (D) 0.001 mg/mL, (E) 0.0001 mg/mL and (F) DMSO control. Zone sizes of (A) 2 mm, (B) 1.5 mm and (C) 1 mm observed after 24 hour incubation at 37 °C.

In order to determine the minimum inhibitory concentration of EIPE-1 on *S. aureus* a culture of *S. aureus* was grown overnight in Mueller Hinton broth (MHB) at 37 ˚C, sub-cultured by a 1/100 dilution into MHB and dispensed into a 96 well culture block (900 µL of diluted culture in each well). To each well either DMSO or a serial dilution of EIPE-1 was added and the culture was grown for 18 h at 37 ˚C. The next day each well was tested for either growth or inhibition of growth by measuring of the OD_{600} of the resulting culture. It was determined that a minimum

inhibitory concentration of 16 µg/mL was needed in broth culture to inhibit *S. aureus* growth. This data correlates to the zone sizes seen in the Kirby-Bauer disc assay (Figure 3.2).

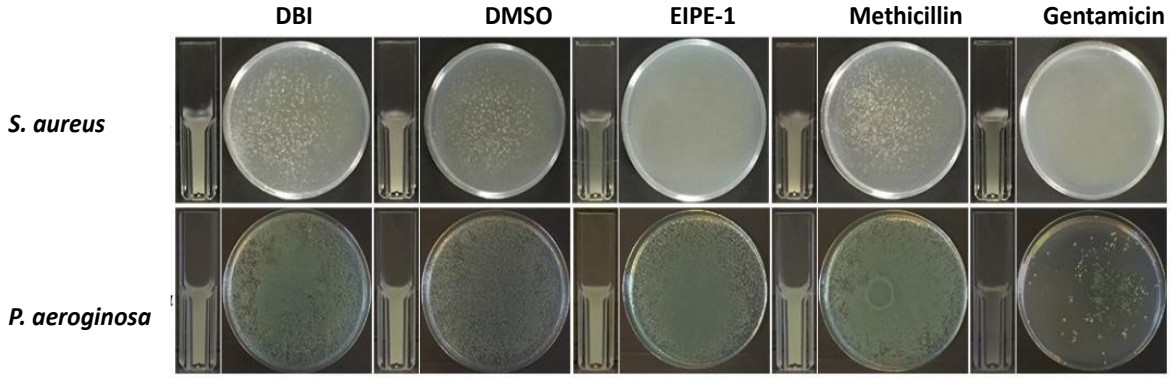

Figure 3.3: Effects of EIPE-1 and antibiotics on *S. aureus* and *P. aeruginosa*. Shown are broth and plate cultures of *S. aureus* (top) and *P. aeruginosa* (bottom) exposed to DBI, DMSO, EIPE-1, Methicillin and Gentamicin.

EIPE-1 antimicrobial activity against *S. aureus* and *P. aeruginosa* was compared to Methicillin and Gentamicin treatment. Bacterial cultures were grown, normalized and then exposed to the DBI, DMSO (solvent control), EIPE-1, Methicillin or Gentamicin (Figure 3.3). EIPE-1 was effective in killing methicillin resistant *S. aureus* (top panel Figure 3.3). This is highly significant and novel as methicillin resistance is a huge problem in hospitals and patient treatment worldwide. EIPE-1 does not appear to have activity against *P. aeruginosa.* Gram negative bacteria like *P. aeruginosa* have an outer membrane covered with lipopolysaccharides that protects the bacteria from antibiotics, dyes, and detergents from penetrating the bacterial cell.

To address *S. aureus* viability in response to EIPE-1 treatment, Live/Dead staining and microscopy was utilized. *S. aureus* was treated with either DBI or EIPE-1 (16 µg/mL each) for 30 minutes (DMSO was used as a negative solvent control) and then stained with the dyes, Sytox 9 (Green stain) and propidium iodide (Red stain). Both of these dyes are nuclear dyes which can bind with the cell's DNA. While Sytox 9 is cell permeable, propidium iodide is impermeable and

can only stain the cell when the outer membrane has been compromised and bacteria are dead. For this reason, live bacteria will stain green and the dead bacteria will be red, allowing for us to measure the proportion of live or dead bacteria by color florescence. The stained bacteria were

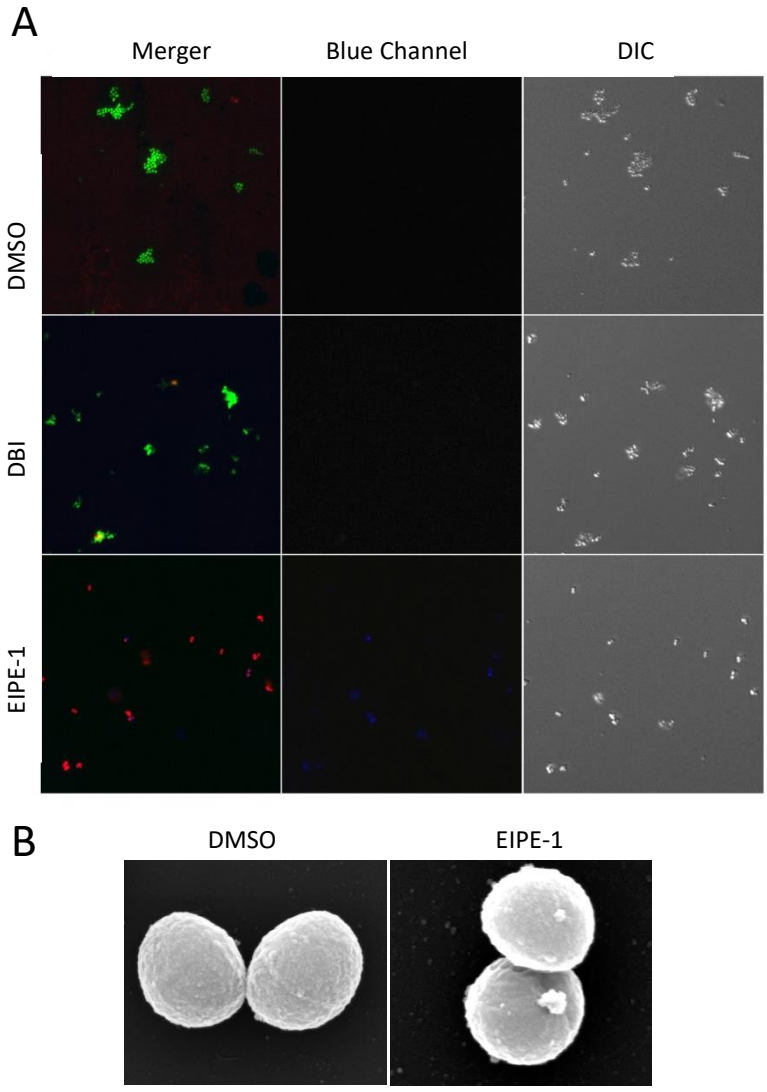

Figure 3.4: Effects of EIPE-1 on *S. aureus* viability**.** (A) *S. aureus* viability was assessed after exposure to DMSO, DBI and EPIE1 for 30 minutes. Live *S. aureus* stain green whereas dead *S. aureus* stain red. The blue channel images and DIC images of bacteria are shown in the middle panel and right panel respectively. (B) Scanning electron microscopy images of DMSO or EIPE-1 treated *S. aureus.*

analyzed under a fluorescent microscope in three different wavelength channels (red, blue and green). The images were taken in the three different channels separately and were merged in

Figure 3.4A. DIC images were also taken to confirm the presence and position of the bacteria. If the *S. aureus* has an intact cell membrane then it will stain fluorescent green whereas if the *S. aureus* have damaged cell membranes they will stain red. The DMSO treated *S. aureus* only stained green and the DBI treated *S. aureus* mostly stained green with only an occasional red stained *S. aureus* bacterium (Figure 3.4A). This was in marked contrast to the EIPE-1 treated *S. aureus* which only stained red (Figure 3.4A). Under blue channel, the bacteria was fluorescing blue, indicating the presence of EIPE-1 inside the bacteria (Figure 3.4A). This result shows that EIPE-1 had indeed killed the *S. aureus* bacteria and suggested that membrane damage was occurring to the *S. aureus* with EIPE-1 treatment.

To visualize potential membrane changes, DMSO and EIPE-1 treated *S. aureus* were prepped and visualized by scanning electron microscopy (Figure 3.4B). DMSO treated *S. aureus* had intact cell membranes whereas the EIPE-1 treated *S. aureus* appeared to have damaged cell membranes as seen via possible protrusions from the *S. aureus* (Figure 3.4B; right), confirming that EIPE-1 may affect membrane or bacterial cell wall integrity.

3.3 CONCLUSION

In summary, a new antimicrobial. EIPE-1, inspired by the black-brown pigment, eumelanin, was designed and synthesized. It was confirmed that the eumelanin-inspired core DBI maintained its intrinsic antimicrobial activity and that enhancement could be achieved with the incorporation of bacterial targeting sites. EIPE-1 exhibited biocidal activity against clinical isolates of Gram-positive bacteria a minimum inhibitory concentration of 16 μg/mL was attained. In comparison with Methicillin and Gentamicin treatment, EIPE-1 exhibited biocidal activity against *S. aureus* but did not display any activity against *P. aeruginosa.*

3.4 EXPERIMENTAL SECTION

3.4.1 Materials and Instrumentation

Tetrakis(triphenylphosphine)palladium(0) [$Pd(PPh_3)_4$], copper (I) iodide (CuI) and 3-chloro-*N*,*N*-dimethylpropan-1-amine hydrochloride were purchased from Sigma-Aldrich. Iodomethane and 4-iodophenol were purchased from Alfa Aesar. Mannitol salts agar was purchased from Criterion Culture Media by Hardy Diagnostics. Luria-Bertani broth, Mueller Hinton agar and Live/Dead *Bac*Light bacterial viability kit were purchased from ThermoFisher. All other solvents and reagents were purchased from Fisher Scientific. All commercial reagents were used as received. Methyl 4,7-dibromo-5,6-dimethoxy-1-methyl-1*H*-indole-2-carboxylate (DBI) was synthesized according to a reported procedure.[29] Et_3N was freshly distilled before use. Unless otherwise specified, all reactions were conducted in oven-dried glassware under nitrogen atmosphere. Anhydrous tetrahydrofuran (THF) and chloroform ($CHCl_3$) were obtained from a solvent purification system under ultrapure argon. Reactions were monitored by thin layer chromatography on silica G TLC plates (Sorbent Technologies No. 1634126). Purifications were performed by column chromatography on silica gel (Sorbent Technologies, 40-63 μm particle size) or neutral alumina (Sorbent Technologies, 32-63 μm particle size). ^1H- and ^{13}C-NMR spectra were measured on a Bruker Avance 400 MHz instrument. High-resolution mass spectrometry was performed using an Orbitrap operated in the FT mode to provide a nominal resolution of 100000.

3.4.2 Synthesis

Synthesis of 3-(4-iodophenoxy)-*N*,*N*-dimethylpropan-1-amine (**2**): Compound **2** was synthesized according to the previously reported procedure with an 83 % yield.[10] The spectrum were consistent with the previously reported data.

Synthesis of 3-(4-ethynylphenoxy)-N,N-dimethylpropan-1-amine (**3**): Compound **3** was synthesized according to the previously reported procedure with 65 % yield.[34] The spectrum were consistent with the previously reported data.

Synthesis of ethyl 4,7-diethynyl-5,6-dimethoxy-1-methyl-1*H*-indole-2-carboxylate (**5**): To a 25-mL Schlenk flask was added **DBI** (500 mg, 1.22 mmol) under argon atmosphere, and then $Pd(PPh_3)_4$, (71 mg, 5 mol %) and CuI (3 mg, 2.5 mol %) were added. To the mixture was added Et_3N (10 mL), followed by trimethylsilylacetylene (603 mg, 6.14 mmol), and the reaction mixture was heated overnight at 80 ˚C. The final mixture was cooled to room temperature, filtered through Celite® and concentrated under vacuum to give a yellow solid. To this solid was added THF (5 mL), MeOH (5 mL) and K_2CO_3 (696 mg, 6.1 mmol). The new reaction mixture was stirred at room temperature for 1 h and then distilled water (10 mL) was added. The resulting mixture was allowed to stir for another 10 minutes. The mixture was extracted with ethyl acetate (3 × 15 mL), dried with $MgSO_4$ and concentrated under *in vacuo*. Column chromatography of the concentrate on silica gel using hexane/ethyl acetate (98:2) as eluent afforded a brown solid (218 mg, 60 %). Mp 137 ˚C (dec). ^{1}H NMR (400 MHz, $CDCl_3$) δ 7.35 (s, 1H), 4.46 (s, 3H), 3.98 (d, *J* = 2.1 Hz, 6H), 3.90 (s, 3H), 3.71 (s, 1H), 3.62 (s, 1H). ^{13}C NMR (101 MHz, $CDCl_3$) ppm δ 161.99, 155.74, 150.76, 134.45, 129.18, 124.78, 110.24, 110.20, 102.57, 88.09, 86.01, 61.72, 61.63, 51.75, 33.54. HRMS (ESI) $[M]^+$ Calcd for $C_{17}H_{16}NO_4$: *m/z* 298.1074. Found: 298.1062.

Synthesis of 3,3'-((((5,6-dimethoxy-2-(methoxycarbonyl)-1-methyl-*1H*-indole-4,7-diyl)bis(ethyne-2,1-diyl))bis(4,1-phenylene))bis(oxy))bis(*N*,*N*,*N*-trimethylpropan-1-aminium) iodide **(**EIPE-1**)**: Into a microwave reactor vial was added compound **5**, methyl 4,7-diethynyl-5,6-dimethoxy-1-methyl-*1H*-indole-2-carboxylate (50 mg, 0.168 mmol) and compound **2**, 3-(4-iodophenoxy)-*N*,*N*-dimethylpropan-1-amine (107 mg, 0.353 mmol). Then $Pd(PPh_3)_4$ (9.7 mg, 5 mol %) and CuI (0.8 mg, 2.5 mol %) were added under argon atmosphere, and the system was sealed. To this freshly distilled Et_3N (1 mL) was added and the reaction mixture was stirred for

24 h at 85 ˚C. The final solution was cooled to room temperature, filtered through Celite® and neutral alumina, and then concentrated *in vacuo* to give a yellowish orange solid. The solid was then dissolved in dry $CHCl_3$ (1 mL), and iodomethane (0.1 mL, 1.61 mmol) was added. The reaction mixture was then stirred overnight at room temperature. A red solid precipitated which was filtered and washed with $CHCl_3$ and dried to afford EIPE-1 (57 mg, 36 %). Mp 234 ˚C (dec). ^{1}H NMR (400 MHz, DMSO-d_6) δ 7.64-7.50 (m, 4H), 7.31 (s, 1H), 7.06 (d, *J* = 7.9, 4H), 4.47 (s, 3H), 4.13 (t, *J* = 5.0 Hz, 4H), 3.96 (d, *J* = 1.6 Hz, 6H), 3.87 (s, 3H), 3.51 (t, *J* = 7.6 Hz, 4H), 3.12 (s, 18H), 2.22 (q, *J*=7.1 Hz, 4H). ^{13}C NMR (101 MHz, DMSO-d_6), ppm 161.62, 159.26, 154.51, 150.13, 133.85, 133.65, 133.08, 129.48, 123.89, 115.62, 115.56, 115.09, 114.99, 110.32, 109.71, 103,33, 100.38, 98.98, 82.71, 82.04, 65.46, 63.37, 61.97, 61.90, 52.81 (t, $J_{C\text{-}N}$ = 3.4 Hz), 52.42, 33.93, 22.98. HRMS (ESI) $[M]^{2+}$ Calcd for $C_{41}H_{51}N_3O_6$: *m/z* 340.6883. Found: 340.6866.

3.4.3 Bacterial Strains, Growth Conditions, and Media

The *S. aureus* and *P. aeruginosa* strains used in this study are clinical isolates obtained from an adult CF patient at the Cystic Fibrosis Clinic at the OU Children's Hospital (Oklahoma City, OK). The strains were grown overnight with shaking at 37 °C (220 RPM) in 15 mL of Luria-Bertani (LB) broth. The overnight culture was sub-cultured the next day before use for the MIC experiments. All subcultures consisted of 1 mL of the overnight culture, mixed with 10 mL of Meuller Hinton broth. The working stock of the EIPE-1 and DBI was prepared by dissolving 1 mg of each in 1 mL of DMSO.

3.4.4 Minimum Inhibitory Concentrations (MIC) Determination

The minimum inhibitory concentrations were determined by the broth microdilution method, following the guidelines of the Clinical and Laboratory Standards Institute (CLSI). Two-fold serial dilutions of EIPE-1 and DBI (starting with 1mg/mL) were prepared in a 100 µL volume in 96-well microtiter plates. The dilution series included DMSO as a negative control. The

bacterial culture (900 µL) was normalized to an OD_{600} of 0.2 and was then added to each well. Plates were incubated with shaking at 220 RPM at 37 °C, and the MIC was determined based on the lowest concentration at which no visible growth of the bacterial isolate was observed.

3.4.5 Susceptibility Testing by the Kirby-Bauer Disc Diffusion Methods

The susceptibility of *S. aureus* to EIPE-1 was determined by the Kirby-Bauer disc diffusion method. Using a cotton swab applicator, a lawn of the *S. aureus* clinical isolate was placed onto Mueller Hinton agar plates to cover the entire surface of the plate. Filter discs (size = 6mm) were added onto the bacterial lawn. EIPE-1, DBI, and DMSO (10 µL each) were then added onto the filter discs. The susceptibility was determined based on an evaluation of the size of the zones of clearance after 24 h of incubation at 37 °C.

3.4.6 Live/dead Staining of EIPE-1 Treated *S. Aureus*

S. aureus was grown overnight in 10 mL of LB broth, sub cultured (5 mL of overnight culture added to 20 mL LB) and grown for 3 h. One hundred and fifty microliters of bacterial culture were removed, and transferred to a 1.5 mL centrifuge tube, which was treated with DMSO, EIPE-1 (0.01 mg/mL) or DBI (0.01 mg/mL) for 30 minutes. Equal amounts of the two dyes [SYTO 9 dye, 3.34 mM in DMSO], and propidium iodide [20 mM in DMSO] were mixed. Then 0.5 µL of dye mixture was added to each tube of treated *S. aureus* cultures. Wet mounts were prepared on glass slides for imaging live and dead *S. aureus*, and Differential Interference Contrast (DIC) images were obtained using a Leica DMI600B fluorescent microscope.

3.4.7 Scanning Electron Microscopy

S. aureus was grown overnight in 10 mL of LB broth, sub cultured (5 mL of overnight culture added to 20 mL LB) and grown for 3 h. Three hundred microliters of *S. aureus* culture was removed, placed into a 1.5 mL tube, and treated with DMSO or EIPE-1 (0.01mg/ML) for 30

minutes. Each sample was placed on glass coverslips (treated with poly-*L*-lysine) in a 24 well plate and fixed with 2% glutaraldehyde (in 0.1 M sodium cacodylate buffer) for 2 h at room temperature (RT). After fixation, samples were washed three times with 0.1 M sodium cacodylate buffer. Samples were then fixed with 1% osmium tetraoxide in water for one hour at RT and were then washed three times with 0.1 M sodium cacodylate buffer. The samples were then dehydrated with an ethanol series (once with 50%, 70%, 90%, 95% and thrice with 100% ethanol). Samples were dried using hexamethyldisilazane (HMDS) and then were mounted on stubs. Finally, samples were coated with gold and palladium using an automated sputter coater. Micrographs were acquired using Quanta 600 Scanning electron microscope.

3.5 REFERENCES

(1) Rossolini, G. M.; Arena, F.; Pecile, P.; Pollini, S. Update on the antibiotic resistance crisis. *Curr Opin Pharmacol* **2014**, *18*, 56-60.

(2) Carlet, J.; Collignon, P.; Goldmann, D.; Goossens, H.; Gyssens, I. C.; Harbarth, S.; Jarlier, V.; Levy, S. B.; N'Doye, B.; Pittet, D.; Richtmann, R.; Seto, W. H.; van der Meer, J. W. M.; Voss, A. Society's failure to protect a precious resource: antibiotics. *The Lancet* **2011**, *378*, 369-371.

(3) Gould, I. M. Coping with antibiotic resistance: the impending crisis. *International Journal of Antimicrobial Agents* **2010**, *36*, S1-S2.

(4) Levy, S. B. Multidrug resistance--a sign of the times. *The New England Journal of Medicine* **1998**, *338*, 1376-1378.

(5) Dantes, R.; Mu, Y.; Belflower, R.; Aragon, D.; Dumyati, G.; Harrison, L. H.; Lessa, F. C.; Lynfield, R.; Nadle, J.; Petit, S.; Ray, S. M.; Schaffner, W.; Townes, J.; Fridkin, S. National

burden of invasive methicillin-resistant Staphylococcus aureus infections, United States, 2011. *JAMA internal medicine* **2013**, *173*, 1970-1978.

(6) Nguyen, D. B.; Lessa, F. C.; Belflower, R.; Mu, Y.; Wise, M.; Nadle, J.; Bamberg, W. M.; Petit, S.; Ray, S. M.; Harrison, L. H.; Lynfield, R.; Dumyati, G.; Thompson, J.; Schaffner, W.; Patel, P. R. Invasive methicillin-resistant Staphylococcus aureus infections among patients on chronic dialysis in the United States, 2005-2011. *Clinical infectious diseases : an official publication of the Infectious Diseases Society of America* **2013**, *57*, 1393-1400.

(7) Klevens, R. M.; Morrison, M. A.; Nadle, J.; Petit, S.; Gershman, K.; Ray, S.; Harrison, L. H.; Lynfield, R.; Dumyati, G.; Townes, J. M.; Craig, A. S.; Zell, E. R.; Fosheim, G. E.; McDougal, L. K.; Carey, R. B.; Fridkin, S. K. Invasive methicillin-resistant Staphylococcus aureus infections in the United States. *Jama* **2007**, *298*, 1763-1771.

(8) Morell, E. A.; Balkin, D. M. Methicillin-resistant Staphylococcus aureus: a pervasive pathogen highlights the need for new antimicrobial development. *The Yale Journal of Biology and Medicine* **2010**, *83*, 223-233.

(9) Ding, L.; Chi, E. Y.; Chemburu, S.; Ji, E.; Schanze, K. S.; Lopez, G. P.; Whitten, D. G. Insight into the mechanism of antimicrobial poly(phenylene ethynylene) polyelectrolytes: interactions with phosphatidylglycerol lipid membranes. *Langmuir* **2009**, *25*, 13742-13751.

(10) Zhou, Z.; Corbitt, T. S.; Parthasarathy, A.; Tang, Y.; Ista, L. K.; Schanze, K. S.; Whitten, D. G. "End-Only" Functionalized Oligo(phenylene ethynylene)s: Synthesis, Photophysical and Biocidal Activity. *The Journal of Physical Chemistry Letters* **2010**, *1*, 3207-3212.

(11) Parthasarathy, A.; Goswami, S.; Corbitt, T. S.; Ji, E.; Dascier, D.; Whitten, D. G.; Schanze, K. S. Photophysics and Light-Activated Biocidal Activity of Visible-Light-Absorbing Conjugated Oligomers. *ACS Applied Materials & Interfaces* **2013**, *5*, 4516-4520.

(12) Zhao, Q.; Li, J.; Zhang, X.; Li, Z.; Tang, Y. Cationic Oligo(thiophene ethynylene) with Broad-Spectrum and High Antibacterial Efficiency under White Light and Specific Biocidal Activity against S. aureus in Dark. *ACS Applied Materials & Interfaces* **2016**, *8*, 1019-1024.

(13) Simon, J. D.; Peles, D. N. The Red and the Black. *Acc. Chem. Res.* **2010**, *43*, 1452-1460.

(14) Rok, J.; Otreba, M.; Buszman, E.; Wrzesniok, D. Melanin - from melanocyte to keratinocyte that is how melanin is transported within the skin. *Annales Academiae Medicae Silesiensis* **2012**, *66*, 60-66.

(15) Ito, S.; Wakamatsu, K. Diversity of human hair pigmentation as studied by chemical analysis of eumelanin and pheomelanin. *Journal of the European Academy of Dermatology and Venereology* **2011**, *25*, 1369-1380.

(16) Prota, G. *Melanins and Melanogenesis*, 1st ed; Academic Press: New York, 1992.

(17) Birngruber, C. G.; Verhoff, M. A. In *Handbook of Hair in Health and Disease*; Preedy, V. R., Ed.; Wageningen Academic: Netherlands, 2011; Chapter 2, pp 31-49.

(18) Aoki, H.; Kunisada, T. Recent progress on melanin research. *Fragrance Journal* **2008**, *36*, 10-16.

(19) Rosman, H. In *Light in Biology and Medicine*; Douglas, R. H.; Moan, J.; Dall'Acuao, F., Eds.; Springer: Boston, MA, 1988, pp 321-327.

(20) Pathak, M. A. In *Light in Biology and Medicine*; Douglas, R. H.; Moan, J.; Dall'Acuao, F., Eds.; Springer: Boston, MA, 1988, pp 337-344.

(21) Meredith, P.; Sarna, T. The physical and chemical properties of eumelanin. *Pigment Cell Research* **2006**, *19*, 572-594.

(22) d'Ischia, M.; Napolitano, A.; Pezzella, A. 5,6-Dihydroxyindole Chemistry: Unexplored Opportunities Beyond Eumelanin. *European Journal of Organic Chemistry* **2011**, *2011*, 5501-5516.

(23) Meredith, P.; Powell, B. J.; Riesz, J.; Nighswander-Rempel, S. P.; Pederson, M. R.; Moore, E. G. Towards structure-property-function relationships for eumelanin. *Soft Matter* **2006**, *2*, 37-44.

(24) d'Ischia, M.; Napolitano, A.; Pezzella, A.; Meredith, P.; Sarna, T. Chemical and Structural Diversity in Eumelanins: Unexplored Bio-Optoelectronic Materials. *Angewandte Chemie International Edition* **2009**, *48*, 3914-3921.

(25) Meredith, P.; Tandy, K.; Mostert, A. B. In *Organic Electronics*; F., C., Santato, C., Eds.; Wiley-VCH Verlag GmbH & Co. KGaA: 2013, pp 91-111.

(26) Pezzella, A.; Wünsche, J. In *Organic Electronics*; Cicoira, F., Santato, C., Eds.; Wiley-VCH Verlag GmbH & Co. KGaA: 2013, pp 113-137.

(27) Nosanchuk, J. D.; Casadevall, A. The contribution of melanin to microbial pathogenesis. *Cellular Microbiology* **2003**, *5*, 203-223.

(28) Nosanchuk, J. D.; Casadevall, A. Impact of Melanin on Microbial Virulence and Clinical Resistance to Antimicrobial Compounds. *Antimicrobial Agents and Chemotherapy* **2006**, *50*, 3519-3528.

(29) Selvaraju, S.; Niradha Sachinthani, K. A.; Hopson, R. A.; McFarland, F. M.; Guo, S.; Rheingold, A. L.; Nelson, T. L. Eumelanin-inspired core derived from vanillin: a new building block for organic semiconductors. *Chemical Communications* **2015**, *51*, 2957-2959.

(30) Selvaraju, S.; Adhikari, S.; Hopson, R. A.; Dai, S.; Rheingold, A. L.; Borunda, M. F.; Nelson, T. L. Effects of structural variations on the optical and electronic properties of eumelanin-inspired small molecules. *Journal of Materials Chemistry C* **2016**, *4*, 3995-3999.

(31) Velkov, T.; Roberts, K. D.; Nation, R. L.; Thompson, P. E.; Li, J. Pharmacology of polymyxins: new insights into an 'old' class of antibiotics. *Future microbiology* **2013**, *8*, 711-724.

(32) Baker, Z.; Harrison, R. W.; Miller, B. F. Action of Synthetic Detergents on the Metabolism Of Bacteria. *The Journal of experimental medicine* **1941**, *73*, 249-271.

(33) Matsen, J. M.; Koepcke, M. J.; Quie, P. G. Evaluation of the Bauer-Kirby-Sherris-Turck single-disc diffusion method of antibiotic susceptibility testing. *Antimicrobial agents and chemotherapy* **1969**, *9*, 445-453.

(34) Placide, V.; Pitrat, D.; Grichine, A.; Duperray, A.; Andraud, C.; Maury, O. Design and synthesis of europium luminescent bio-probes featuring sulfobetaine moieties. *Tetrahedron Letters* **2014**, *55*, 1357-1361.

CHAPTER IV

SYNTHESIS AND CHARACTERIZATION OF EUMELANIN-INSPIRED CONJUGATED POLYMERS

4.1 INTRODUCTION

Poly(arylenevinylene)s (PAVs) and poly(aryleneethynylene)s (PAEs) are a class of conjugated polymers that are frequently reported for their potential use in a large number of applications including organic light emitting diodes (OLED)s, thin film transistors (TFT)s, chemical sensors, and photovoltaic cells (PVC)s.[1-12] This is due to ease of processing, good optical and electronic properties, and the tunability of semiconducting properties to match desired applications. There are several different building blocks that have been incorporated in PAEs and PAVs, but there are limited examples utilizing the indole moiety as a building block for synthesizing PAEs and PAVs. Our interest in using indole as a building block for conjugated polymers stems from indole's ubiquity in nature. Indole is biocompatible and has been a building block in several biopolymers such as eumelanins. Eumelanin is a black-brown pigment and understood to be a biosynthesized heterogeneous macromolecule containing 5,6-dihydroxyindole (DHI) and 5,6-dihydroxyindole-2-carboxylic acid (DHICA) units.[13] Extensive research has been done on the optical, electronic, physical, metal chelating, and structural properties of natural and synthetic eumelanin.[14-19] Our group previously synthesized an eumelanin-inspired core (DBI) similar to the building blocks found in eumelanin.[20] We also demonstrated, *via* small molecules, that

substitution at the 4- and 7-positions affect both the optical and electrical properties of these organic semiconductors.[21] To further understand how to influence the optoelectronic properties of this bioinspired building block, we have incorporated the eumelanin-inspired indole core into conjugated polymers. In this chapter, the synthesis of new conjugated polymers based on our eumelanin-inspired core, differing by arylene and carbon–carbon bond linkages will be discussed. Four new polymers have been synthesized using Stille and Sonagashira coupling. Poly(indoylenephenyleneethynylene) (PIPE) has been prepared *via* a different route in order to compare the polymers' properties. Further, the attempted synthesis of high molecular weight PIE and PIV by incorporating solubilizing groups on eumelanin-inspired cores will also be discussed.

These new molecules were characterized using gel permeation chromatography (GPC), ^{1}H and ^{13}C NMR spectroscopy, Fourier transform infrared spectroscopy (FTIR), thermal gravimetric analysis (TGA), differential scanning calorimetry (DSC) and atomic force microscopy (AFM). Optical and electronic properties of these polymers were further evaluated using UV–visible and fluorescence spectroscopy as well as cyclic voltammetry.

4.2 RESULTS AND DISCUSSION

4.2.1 Synthesis and Physical Properties

The synthetic routes for PIE, PIV, PIPE, PIFE and PICE polymers are shown in Scheme 4.1. The yield, number average molecular weight (M_n), and polydispersity index (PDI) for all polymers are shown in Table 4.1. PIE and PIV were synthesized using Stille coupling conditions resulting in low molecular weight polymers, M_n of 1.8 and 2.8 kDa, respectively. To obtain high molecular weights of PIE and PIV, Stille coupling conditions were altered by changing the ligand. The ligands evaluated were P(*t*-Bu)$_3$, P(*o*-tol)$_3$, and X-Phos. Unfortunately, similar molecular weights and yields were observed. The low molecular weights of PIE and PIV were due to a lack of solubilizing groups on the eumelanin-inspired core. This ultimately resulted in precipitation

before high molecular weight materials could be achieved. PIPE, PIFE, and PICE were synthesized using Sonagashira coupling conditions resulting in moderate to high molecular weight polymers, 26.3 kDa, 15.1 kDa, and 12.0 kDa respectively. All five polymers were soluble in common organic solvents such as chloroform and THF.

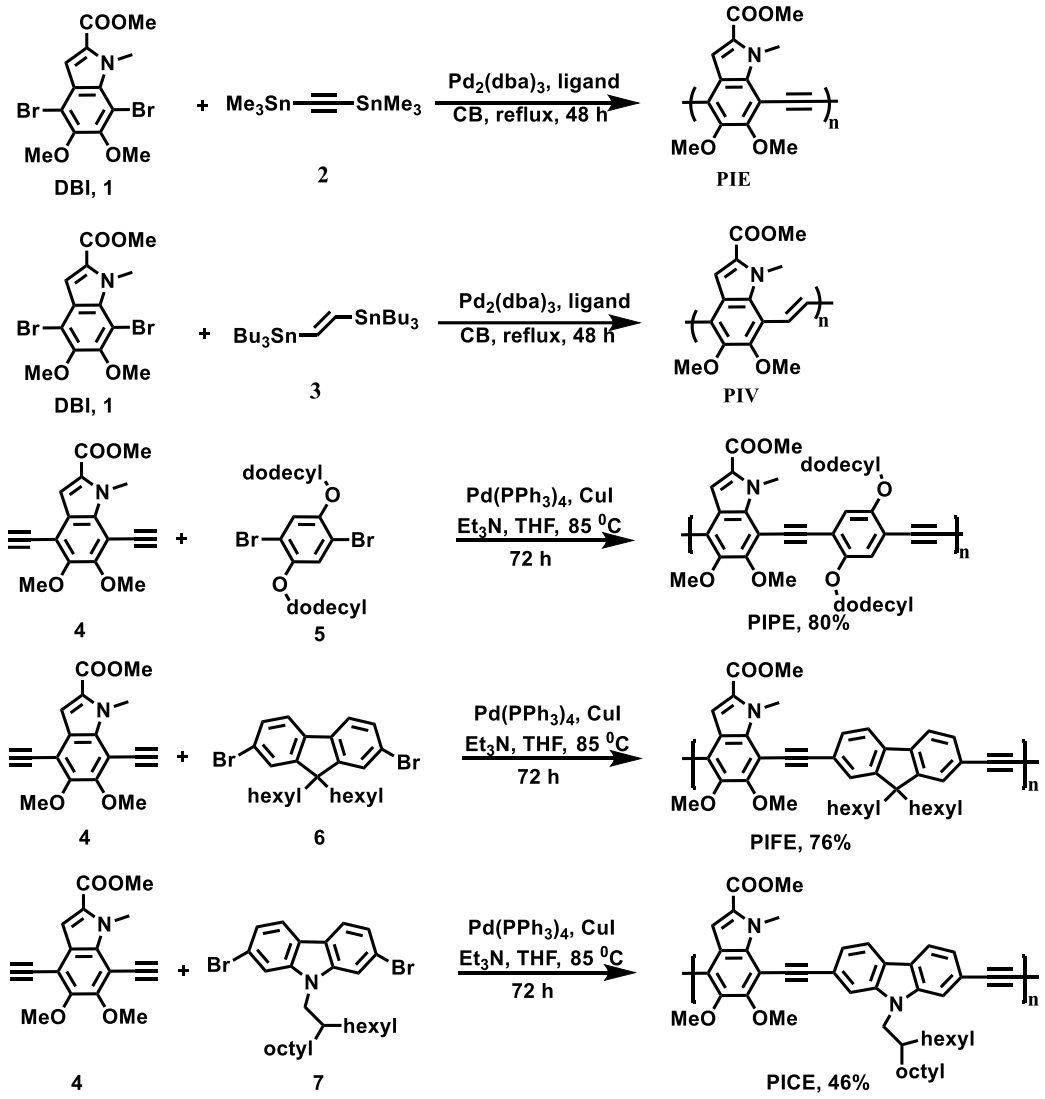

Scheme 4.1: Synthesis of PIE, PIV, PIPE, PIFE, and PICE polymers.

Table 4.1: Structure properties of polymers.

Polymer	M_n[a] (kDa)	M_w[a] (kDa)	PDI[a]	Yield (%)	T_d[b] (°C)	T_g[c] (°C)
PIE	1.8	2.2	1.20	42	172	188
PIV	2.1	2.3	1.10	46	194	134
PIPE	26.3	62.2	2.3	80	268	-
PIFE	15.1	33.8	2.2	76	320	-
PICE	12.0	23.8	1.9	46	310	-

[a] The number average molecular weight and the PDI were measure by GPC on polystyrene standards.
[b] 5% weight loss temperature by TGA under N_2.
[c] Data from second scan reported, heating rate 3 °C min^{-1} under N_2.

4.2.2 Optical and Electronic Properties

The photophysical properties of these polymers were evaluated using UV–vis absorption and fluorescence spectroscopy both as dilute solutions in $CHCl_3$ and as thin films. The absorption and emission spectra of the polymers are shown in Figures 4.1, and the spectroscopic data are summarized in Table 4.2. Compared to the vinylene-linked polymer, PIV, the ethynylene-linked counterpart, PIE, exhibited bathochromically shifted absorption spectra. The absorption maxima in solution and film for PIV were at 438 and 431 nm, respectively; however these absorptions were red-shifted to 459 and 478 nm for PIE. This spectral difference can be explained by the better pi-conjugation along the polymer chain due to the ethynylene linkage as it minimizes steric and conformational hindrances in contrast to the vinylene linkage.[22,23] However, the emission maxima for PIE were blue-shifted in comparison to the PIV. This spectral behavior can be correlated with the rigid backbone structure of the ethynylene-linked polymers compared to the

vinylene-linked systems. This is also the same reason large Stokes shift is observed in PIV in comparison to the PIE (Table 4.2).[24] In case of eumelanin-inspired polymers differing by arylene groups, the red-shifted absorption maxima in solution and film are found in the increasing order of PIFE > PICE > PIPE. This indicates better pi-conjugation along the polymer chain follows the order PIPE > PICE > PIFE. The broad and red-shifted absorption spectra were observed for all polymer thin films, excluding PIV. In the case for the vinylene-linked polymers, the λ_{max} for the absorption spectra in solution and thin films were comparable. However, other polymers (PIE, PIPE, PIFE and PICE) exhibited significantly red-shifted λ_{max} values for the absorption spectra (19–34 nm) for polymer thin films versus solution.

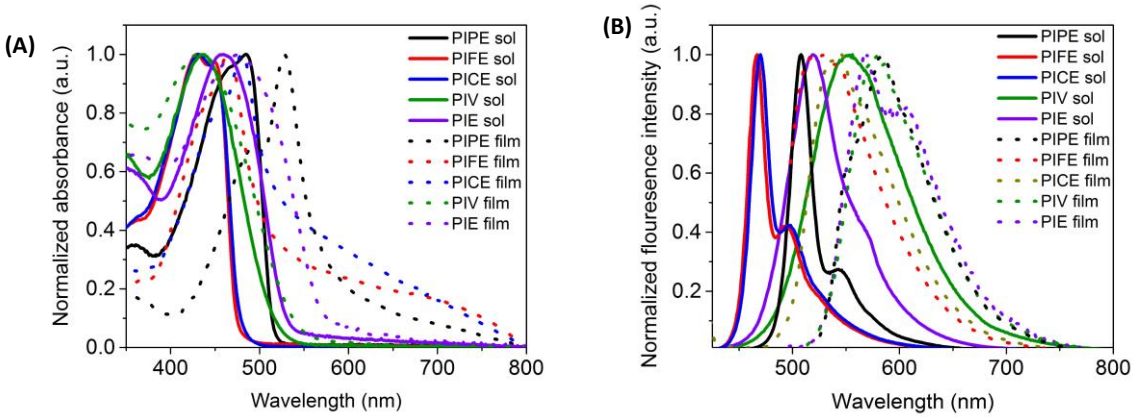

Figure 4.1: A) Absorption spectra and B) Emission spectra of polymer in solution ($CHCl_3$, solid lines) and the thin film (drop cast from $CHCl_3$, dashed lines). For emission spectra polymers were excited at 285 nm (solution) and 400 nm (thin film).

The fluorescence quantum yield, which is a ratio of number of photons emitted to the numbers of photons absorbed, was calculated using following equation:[1] $\phi_s = \phi_r(\frac{A_r F_s}{A_s F_r})(\frac{n_s^2}{n_r^2})$. ϕ_r is 0.79, A_s *and* A_r are absorbances of the sample and reference (fluorescein) solutions, respectively at the same excitation wavelength, F_s *and* F_r are the corresponding relative integrated fluorescence intensities, n is the refractive index [$CHCl_3$ (n_s = 1.445) and 0.1 NaOH (n_r = 1.335) were used]. The quantum yield data are summarized in Table 4.2. In solution, all polymers were efficient fluorophores with

Table 4.2: Electronic and optical properties of PIPE, PIFE, PICE, PIV and PIE.

Polymer	Media	λ_{abs}[a] (nm)	λ_{ems}[a] (nm)	Stoke's Shift (cm^{-1})	ϕ_{re}[b]	E_g^{opt} (eV)[c]	E_{ox} (V)[d]	HOMO (eV)[e]	LUMO (eV)[f]
PIPE	$CHCl_3$	484	508	1053	0.67				
	FILM	528,412	582	1903		2.17	1.00	-5.43	-3.26
PIFE	$CHCl_3$	429,454	468,496						
	FILM	465	528			2.41	1.15	-5.58	-3.17
PICE	$CHCl_3$	432	470,498						
	FILM	480	545			2.34	1.05	-5.48	-3.14
PIV	$CHCl_3$	438	556	4845	0.21				
	FILM	431	579			2.34	0.94	-5.35	-3.01
PIE	$CHCl_3$	459	519	2518	0.49				
	FILM	478	569			2.22	1.03	-5.44	-3.22

[a]Measured in dilute chloroform. [b]Quantum yields measured in dilute chloroform solutions relative to fluorescein. [c]Measured from the tangent drawn at the onset of absorption. [d]Measured from the onset of oxidation wave.
[e]Calculated from the onset of the first oxidation from the equations E_{HOMO} (eV) = -[E_{ox}^{onset} – $E_{1/2}$ (Fc/Fc^+) + 4.8], where $E_{1/2}(Fc/Fc^+)$ was the cell correction. [f]Calculated from the equation LUMO = (E_g^{opt} – HUMO).

fluorescence quantum yields ranging from 0.12 to 0.67. As expected, the ethynylene-linked polymers have high fluorescence quantum yields in solution. This is attributed to the shape-persistent, rigid rod-like structures of the ethynylene-linked polymers.[22,23] Optical bandgaps were calculated from wavelengths corresponding to the energy absorption onset from the intersection of the leading edge tangent with the x-axis. The optical bandgap of the PIE was relatively smaller than that of the PIV. While comparing the different polymers with arylene groups, PIPE was found to have a relatively smaller optical band gap than those of PIFE and PICE. It might be due to the higher molecular weight of PIPE, which lead to better conjugation and a decrease in bandgap. The optical band gaps of PICE and PIFE were comparable. The electronic properties

were measured by cyclic voltammetry on thin films of these eumelanin-inspired polymers; the results are summarized in Table 4.2, and the voltammograms are shown in Figure 4.2. The HOMO energy values were calculated from the onset of the first oxidation from the equations HOMO (eV) = -[E_{ox}^{onset} – $E_{1/2}$ (Fc/Fc$^+$) + 4.8] where $E_{1/2}$ (Fc/Fc$^+$) was the cell correction. The LUMO energy values were calculated from the equation LUMO (ev) = (E_g^{opt}- HOMO) where E_g^{opt} is the optical band gap. All of these polymers showed irreversible oxidation potentials and did not give any reduction wave when scanning in the negative potential up to -2 V. PIE and PIV have similar HOMO levels, suggesting that changing the backbone from triple bond to double bond has little effect on the HOMO levels. However, LUMO levels are stabilized (lowered) for the ethynylene-linked polymer PIE when compared with their vinylene counterpart PIV. This is attributed to the ethynylene's weak electron-withdrawing nature which should result in lowering of LUMO level.[22,23]

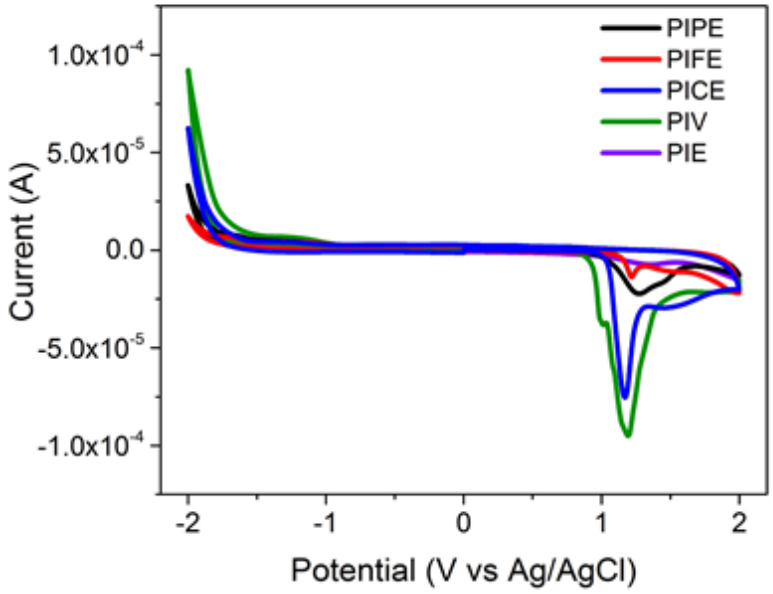

Figure 4.2: CV spectra of PIPE, PIFE, PICE, PIV, and PIE.

4.2.3 Thermal Analysis

The thermal stability of the polymers was evaluated using TGA and DSC. The TGA curves are shown in Figure 4.3A, and data are summarized in Table 4.1. As expected, the higher molecular weight polymers, PIPE, PIFE and PICE, were thermally more stable compared to the lower molecular weight of PIE and PIV. Although the T_d is significantly lower for PIE and PIV, compared to PIPE, PIFE and PICE, it is still high enough for these polymers to be useful in the semiconducting applications. DSC scans of the second cooling cycle for the polymers are shown in Figure 4.3B. The glass transition temperatures (T_g) of the polymers are summarized in Table 4.1. DSC revealed T_g of PIE and PIV at 183 °C and 135 °C, respectively, whereas PIPE, PIFE and PICE did not show any observable transitions before the decomposition temperatures. The higher T_g of PIE in comparison to PIV can be correlated to the rigid backbone of PIE compared to PIV.[25,26] In all of these polymers, crystallization and melting transitions were not observed, suggesting an amorphous nature for these materials.[27,28]

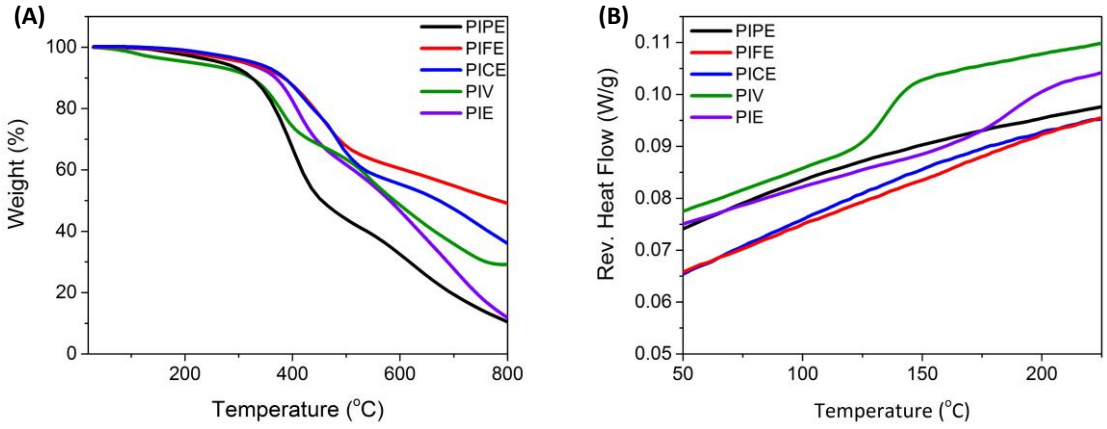

Figure 4.3: TGA curves (A) and DSC curves (B) of PIPE, PIFE, PICE, PIV and PIE.

4.2.4 FTIR

The polymers were further characterized by FTIR experiments and spectra are depicted in Figure 4.4. The characteristic peak for the carbonyl of the ester group at 1710 cm^{-1} confirmed the presence of the DBI core in all the polymers. For polymer having an ethynylene linkage (PIE, PIPE, PIFE and PICE), the characteristic peak at 2185 cm^{-1} confirmed the presence of carbon–carbon triple bonds in these polymers, which were absent in PIV.

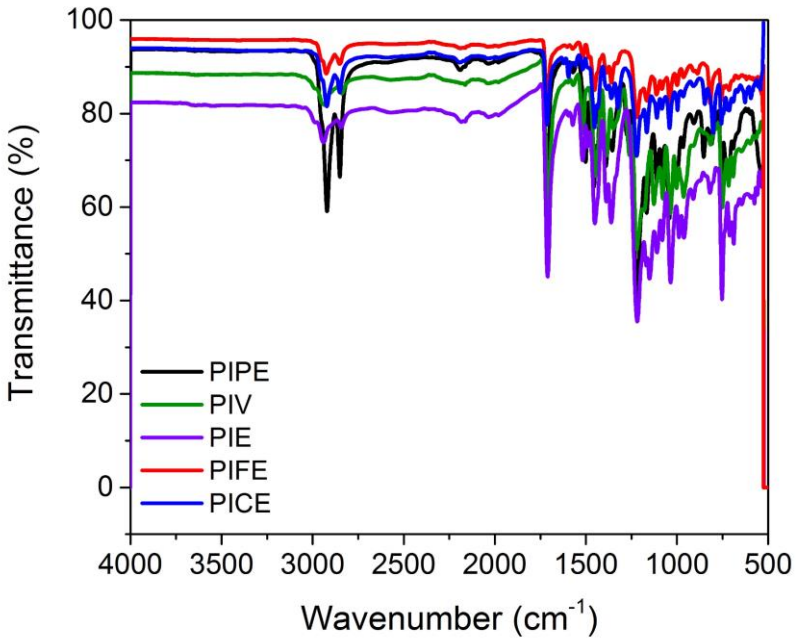

Figure 4.4: FTIR spectra of PIPE, PIFE, PICE, PIV, and PIE.

4.2.5 Morphology Characterization

AFM was used to study the morphology of thin films of the three different polymers (PIE, PIV and PIPE), as shown in Figure 4.5. The polymer thin films appear to be composed of packed small grains varying in size and shape. Compared to PIE and PIV, PIPE thin films show almost no pitted areas where polymers do not assemble, indicating that the added 1,4-bis(dodecyloxy)benzene motif lead to better intermolecular interactions. In particular, the long

dodecyloxy side chains provide substantial alkyl–alkyl interactions that could affect the polymer chain aggregations. The grain sizes for PIV and PIE are generally 10 nm in diameter, while the grains of PIPE are about 20 nm. The doubled grain sizes of PIPE compared to PIE and PIV are likely due to the enhanced stacking between conjugated backbone through added 1,4-bis(dodecyloxy)benzene and the additional alkyl side chains. It was expected to see similar morphology in PIFE and PICE as they also have additional aryl motifs with long alkyl chains.

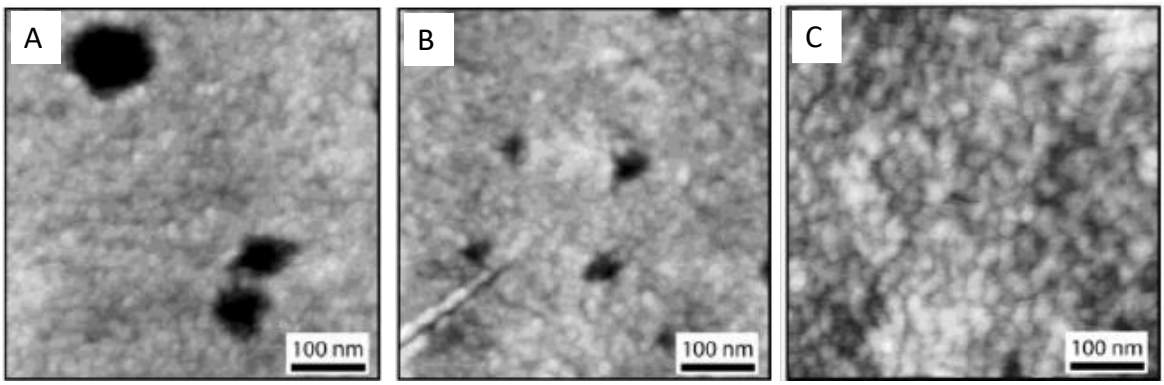

Figure 4.5: 500 x 500 nm^2 AFM topography images of (A) PIV, (B) PIE, and (C) PIPE. The z ranges are 30 nm for (A) and (B) and 15 nm for (C). RMS roughness values for (A)-(C), excluding the pits in (A) and (B), are 2.43, 2.03, and 1.64 nm respectively.

4.3 ATTEMPTED SYNTHESIS OF HIGH MOLECULAR WEIGHT PIE AND PIV

The molecular weights of PIE and PIV were quite small. This was due to a lack of solubilizing groups on the eumelanin-inspired core which ultimately resulted in precipitation before high molecular weight materials could be achieved. Thus, to achieve high molecular weight polymers, the solubilizing group was incorporated on the Eumelanin-inspired core. The synthetic route for the synthesis of eumelanin-inspired core having a solubilizing group is depicted in Scheme 4.2. The ester group at DBI core was hydrolyzed to the carboxylic acid and then converted to the acid chloride by treatment with oxalyl chloride. The compound **9** was reacted with *N*,*N*-dioctylamine to get an eumelanin-inspired core with a potential solubilizing group. Polymerization of

compound **10** was attempted under Stille coupling conditions with compounds **2** and **3** but did not proceed. The reaction with different ligands such as P(*t*-Bu)$_3$, P(*o*-tol)$_3$, and X-Phos with $Pd_2(dba)_3$ as catalyst was attempted, but did not result in any polymers. At this point the reason behind not obtaining polymers under the reaction conditions is not clear. It may be related to the stability of the monomer or we may need to try different reaction conditions to get the polymers.

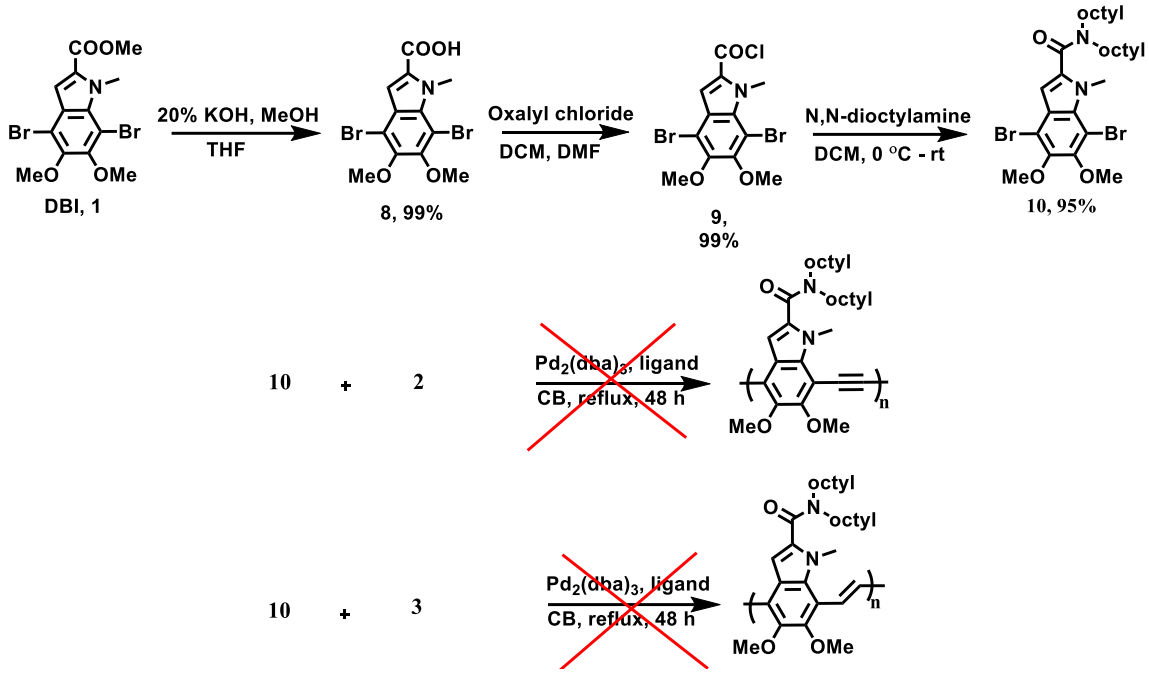

Scheme 4.2: Synthesis of the Eumelanin-inspired core with solubilizing group and high molecular weight PIE and PIV.

4.4 CONCLUSION

Five conjugated polymers based on the eumelanin-inspired indole core were synthesized differing by the arylene and carbon–carbon bond linkages. The ethynylene-linked polymer, PIE showed red-shifted absorption spectra and blue-shifted emission spectra compared to the vinylene-linked, PIV. Furthermore, the optical bandgap of PIE was reduced compared to PIV. These behaviors can be explained based on findings that ethynylene linkage minimizes steric and conformational hindrances, which leads to better p-conjugation along the polymer backbone and hence a red-

shifted absorption spectra with reduced optical bandgap. Due to the rigidity of the ethynylene-linked polymer backbone in PIE, the emission spectrum is blue-shifted and exhibits much less Stokes shift compared to the vinylene-linked polymer. The HOMO levels of PIE and PIV are not affected by the change in the carbon–carbon bond linkage while the LUMO of the ethynylene-linked polymers are stabilized due to the weak electron withdrawing nature of the ethynylene unit compared to the vinylene-linked polymer. In the case of eumelanin-inspired polymers differing by aryl groups, PIPE had a lower band gap and a red shifted absorption compared to PIFE and PICE. Among PIFE and PICE, not much difference in optoelectronic properties was seen. The molecular weights of PIE and PIV were quite small in comparison to PIPE, PIFE and PICE. However, despite the low molecular weights, these polymers were found to have good optical and electrical properties. An attempt to synthesize high molecular weight PIE and PIV by incorporating solubilizing groups on the eumelanin-inspired indole core. Even though the solubilizing group was successfully incorporated on the eumelanin-inspired core, polymers could not be synthesized from this molecule.

4.5 EXPERIMENTAL SECTION

4.5.1 Materials

Anhydrous *N*,*N*-dimethylformamide (DMF) and tetrahydrofuran (THF) were obtained from a solvent purification system under ultrapure argon. Et_3N was redistilled under argon before use. DBI[20] and methyl 4,7-diethynyl-5,6-dimethoxy-1-methyl-1H-indole-2-carboxylate (compound **4)** were synthesized according to the previously reported procedure. All other commercial reagents were used as received.

4.5.2 Instrumentation

^{1}H and ^{13}C NMR spectra were measured on a Bruker Avance 400 MHz instrument. GPC was performed using a Waters pump with a Waters 2410 refractive index detector with THF as the

solvent at 30 °C with a flow rate 1.0 mL min^{-1}. Polystyrene standards were used for calibration. UV–visible and fluorescence spectra were recorded on a Cary 5000 UV–VIS– NIR spectrophotometer and a Cary Eclipse fluorescence spectrophotometer, respectively. UV–visible and fluorescence measurements were obtained using polymer solutions in $CHCl_3$, and thin films were drop casted from these solutions. Cyclic voltammetry was performed on a BASI CV-50W Version 2.3 instrument with 0.1 M tetrabutylammonium hexafluorophosphate as the supporting electrolyte in dry acetonitrile using a platinum working electrode, a platinum wire as counter electrode, and a Ag/AgCl reference electrode with a scan rate of 100 mV s^{-1}. The CV experiment was performed by drop-casting a thin film of the polymer on the platinum working electrode. TGA measurements were performed using a high-resolution thermogravimetric analyzer TA instrument Model Q-50, within the temperature interval of 30–900 °C, with a rate of 20 °C min^{-1} under continuous nitrogen flow. DSC was performed using a TA Instruments Model Q-2000 from -50 to 250 °C at a heating rate of 3 °C min^{-1} in a modulated mode. The second cooling thermal cycle was chosen to observe the thermal transitions in polymers. All runs were performed under nitrogen. The AFM topographic images of the polymer films were acquired in a NT-MDT NTEGRA Prima AFM using a semicontact mode with a silicon tip (spring force constant = 1.2– 6.4 N m^{-1}). The polymer thin films were prepared by spin-coating 100 mL of 20 mg mL^{-1} polymer solution in chloroform at 1000 rpm. FTIR experiments were evaluated on a Nicolet iS50 FT-IR instrument using ATR diamond.

4.5.3 Synthesis

General procedure for Stille polymerization: In a 25-mL, oven-dried Schlenk flask were placed, methyl 4,7-dibromo-5,6-dimethoxy-1-methyl-1H-indole-2-carboxylate, (**1**, 100 mg, 0.24 mmol), $Pd_2(dba)_3$ (4.4 mg, 2 mol%) and X-Phos (9.3 mg, 8 mol%) under vacuum for 5 min, and the system was purged with argon. This was repeated three times. Bis(trimethylstannyl) substituted monomer (0.24 mmol) in chlorobenzene (3 mL) was added to the Schlenk flask while

stirring. The reaction mixture was purged for 30 min and then heated at reflux for 2 days. The reaction mixture was cooled to room temperature and precipitated into methanol (20 mL) to give precipitate. The resulting precipitate was filtered through a cellulose thimble, which was then subjected to Soxhlet extractions with methanol, hexane, and chloroform. Finally, the solvent was evaporated to yield the polymer.

Synthesis of poly(indoylene ethynylene **(PIE):** Red polymer (30 mg, 45%). ^{1}H NMR (400 MHz, $CDCl_3$) δ 7.67–7.40 (m, indole proton, 1H), 4.71–4.59 (m, –NCH_3, 3H), 4.21–3.95 (m, –OCH_3 and –CO_2CH_3, 9H). ^{13}C NMR (101 MHz, $CDCl_3$) δ 162.24, 155.03, 154.90, 150.36, 150.13, 134.17, 131.89, 131.23, 129.34, 128.70, 128.56, 124.51, 111.45, 110.70, 110.55, 103.86, 103.83, 62.01, 61.81, 52.00, 51.98, 34.05, 33.94, 33.81. M_n = 1.8 kDa and PDI = 1.20.

Poly(indoylene vinylene) **(PIV):** Greenish-brown polymer (31.2 mg, 46%). ^{1}H NMR (400 MHz, $CDCl_3$) δ 7.93–7.31 (m, indole and vinyl protons, 3H), 4.30–4.15 (m, – NCH_3, 3H), 4.02–3.90 (m, –OCH_3 and –CO_2CH_3, 9H). ^{13}C NMR (101 MHz, $CDCl_3$) δ 162.46, 151.04, 147.33, 147.27, 135.71, 130.09, 129.26, 128.98, 128.85, 126.76, 126.60, 122.01, 121.97, 111.32, 110.83, 61.35, 60.97, 51.86, 51.81, 36.67, 36.42, 36.15. M_n = 2.1 kDa and PDI = 1.10.

General procedure for Sonagashira polymerization: In a microwave reactor vial, methyl 4,7-diethynyl-5,6-dimethoxy-1-methyl-1H-indole-2-carboxylate, **4** (50 mg, 0.168 mmol) and dibromoarylene (0.168 mmol) was taken inside a glove box and added $Pd(PPh_3)_4$ (9.7 mg, 0.008 mmol), and CuI (0.8 mg, 0.004 mmol), followed by 5 mL of a 2:1 THF:Et_3N mixture. The vial was sealed inside the glove box and brought outside and heated to 85 °C for 72 hours. The reaction mixture was cooled and the polymer was precipitated in a beaker containing 20 mL of methanol. The resulting precipitate was filtered through a Soxhlet thimble, which was then subjected to methanol, hexane and chloroform extractions. Finally, the solvent was evaporated to yield polymer.

Poly(indoylene phenylene ethynylene) **(PIPE):** Red polymer (97 mg, 80%). ^{1}H NMR (400 MHz, $CDCl_3$) δ 7.56 (s, indole proton, 1H), 7.13–7.05 (m, phenyl protons, 2H), 4.62 (s, –NCH_3, 3H), 4.10 (m, –OCH_3 and –OCH_2, 10), 3.93 (s, – CO_2CH_3, 3H), 1.96–1.86 (m, 4H), 1.24 (m, 36H), 0.88 (t, J = 6H). ^{13}C NMR (101 MHz, $CDCl_3$) δ 162.29, 154.85, 153.89, 150.04, 134.40, 132.30, 132.20, 128.97, 128.70, 128.58, 124.73, 116.45, 116.09, 114.08, 111.29, 103.77, 103.69, 69.74, 69.33, 62.12, 61.99, 51.77, 46.04, 34.03, 32.07, 29.80, 29.61, 29.51, 29.43, 26.21, 22.84, 14.27. M_n = 26.3 kDa and PDI = 2.3.

Poly(indoylene flourene ethynylene) **(PIFE):** Yellowish brown polymer (80 mg, 76%). ^{1}H NMR (400 MHz, $CDCl_3$) δ 7.76 - 7.48 (m, indole and fluorene protons, 7H), 4.65(s, -NCH_3, 3H), 4.14 (s, -OCH_3, 6H), 3.97 (s, -CO_2CH_3, 3H), 2.04 (m, 4H, 1.26-1.10 (m, 16H), 0.79 (t, *J* = 5.6, 6H). M_n = 15.1 kDa, PDI = 2.2.

Poly(indoylene carbazole ethynylene) **(PICE):** Yellow polymers (52 mg, 47%). ^{1}H NMR (400 MHz, $CDCl_3$) δ 8.09-7.37 (m, indole and flourene protons, 7H), 4.65 (s, -NCH_3, 3H), 4.15 (s, -OCH_3, 6H), 4.01-3.91 (m, 5H), 2.16 (m, 1H), 1.41-1.23 (m, 24H), 0.83 (m, 6H). M_n = 12.0 kDa, PDI = 1.9.

Synthesis of 4,7-dibromo-5,6-dimethoxy-1-methyl-1H-indole-2-carboxylic acid (**8**): In a 250 mL one-necked round-bottomed flask, DBI (200 mg, 0.49 mmol) was dissolved in THF (15 mL) and added aqueous 20 % KOH (4 mL) and MeOH (4 mL). The reaction mixture was stirred at room temperature for 3 h. After the completion of the reaction, 10% HCl (15 mL) was added and stirred for 5 min. The product was extracted in DCM (3 x 15 mL) and the organic layer was washed with distilled water, dried over $MgSO_4$ and concentrated in vacuo to afford 2 as a white solid which was used for next step without further purification. Yield (193, 99%). ^{1}H NMR (400 MHz, DMSO-d_6) δ 7.09 (s, 1H), 4.36 (s, 3H), 3.84 (s, 3H), 3.82 (s, 3H). ^{13}C NMR (101 MHz,

DMSO-d_6) δ 162.49, 150.10, 146.60, 132.68, 131.92, 124.78, 110.46, 108.84, 100.19, 61.57, 61.45, 35.05.

Synthesis of 4,7-dibromo-5,6-dimethoxy-1-methyl-1H-indole-2-carbonyl chloride (**9**): In a 100 mL one neck round bottom flask, compound **8** (150 mg, 0.38 mmol)) was dissolved in dry DCM (5 mL) and oxalyl chloride (0.1 mL, 1.16 mmol) was added followed by a drop of DMF. The reaction proceeded vigorously after the addition of DMF. The reaction was stirred for 2 h at room temperature. After the completion of the reaction, the reaction mixture was concentrated *in vacuo* to afford white solid which was used for next step without further purification. Yield (157 mg, 99%). ^{1}H NMR (400 MHz, $CDCl_3$) δ 7.67 (s, 1H), 4.38 (s, 3H), 3.95 (s, 3H), 3.92 (s, 3H). ^{13}C NMR (101 MHz, $CDCl_3$) δ 159.26, 152.49, 147.41, 135.04, 131.84, 124.83, 119.86, 110.31, 99.85, 61.34, 61.27, 35.29.

Synthesis of 4,7-dibromo-5,6-dimethoxy-1-methyl-*N*,*N*-dioctyl-1H-indole-2-carboxamide (**10**): In a 100-mL one-necked round-bottomed flask, compound **9** (150 mg, 0.36 mmol) was dissolved in dry DCM (10 mL) and cooled to 0 °C in an ice-bath. *N*,*N*-dioctylamine (279 mg, 1.09 mmol) was added and the reaction mixture was warmed to room temperature and stirred for 1 h. When TLC indicated the reaction is completed, the solvent was removed under reduced pressure, and the residue was purified by flash column chromatography on silica gel with a mixture of hexane and ethyl acetate (95:5) to afford the compound **10** as a clear liquid. Yield (210 mg, 95%). ^{1}H NMR (400 MHz, $CDCl_3$ δ 6.50 (s, 1H), 4.08 (s, 3H), 3.91 (s, 3H), 3.90 (s, 3H), 3.50 (t, J = 7.1 Hz, 2H), 3.36 (t, J = 7.1 Hz, 2H), 1.66 (m, 2H), 1.55 (m, 2H), 1.35-1.18 (m, 20H), 0.86 (m, 6H). ^{13}C NMR (101 MHz, $CDCl_3$) δ 163.47, 148.31, 146.07, 136.47, 130.49, 125.93, 108.33, 102.33, 99.59, 61.30, 61.26, 49.00, 44.95, 34.75, 31.80, 31.72, 29.37, 29.27, 29.08, 28.78, 27.48, 27.12, 26.49, 22.63, 14.10.

4.6 REFERENCES

(1) Dini, D. Electrochemiluminescence from Organic Emitters. *Chemistry of Materials* **2005**, *17*, 1933-1945.

(2) H. S. Nalwa, L. S. R. *Handbook of luminescence, Display Materials, and Devices*; American Scientific Publishers: Los Angeles, **2003**.

(3) Kraft, A.; Grimsdale, A. C.; Holmes, A. B. Electroluminescent Conjugated Polymers—Seeing Polymers in a New Light. *Angewandte Chemie International Edition* **1998**, *37*, 402-428.

(4) Segura, J. L.; Martin, N.; Guldi, D. M. Materials for organic solar cells: the C60/[small pi]-conjugated oligomer approach. *Chemical Society Reviews* **2005**, *34*, 31-47.

(5) Günes, S.; Neugebauer, H.; Sariciftci, N. S. Conjugated Polymer-Based Organic Solar Cells. *Chemical Reviews* **2007**, *107*, 1324-1338.

(6) Thomas, S. W.; Joly, G. D.; Swager, T. M. Chemical Sensors Based on Amplifying Fluorescent Conjugated Polymers. *Chemical Reviews* **2007**, *107*, 1339-1386.

(7) Swager, T. M.; Zheng, J. In *Advances in Polymer Science*; Weder, C., Ed.; Springer-Verlag Berlin Heidelberg: **2005**, p 151-179.

(8) Bunz, U. H. F. *Poly(arylene ethynylenes)s: From Synthesis to Application*; Springer-Verlag Berlin Heidelberg, **2005**.

(9) Bunz, U. H. F. Poly(aryleneethynylene)s: Syntheses, Properties, Structures, and Applications. *Chemical Reviews* **2000**, *100*, 1605-1644.

(10) Nesterov, E. E.; Zhu, Z.; Swager, T. M. Conjugation Enhancement of Intramolecular Exciton Migration in Poly(p-phenylene ethynylene)s. *Journal of the American Chemical Society* **2005**, *127*, 10083-10088.

(11) Pang, Y. In *Design and Synthesis of Conjugated Polymers*; Leclerc, M., Morin, J.-F., Eds.; Wiley-VCH Verlag GmbH & Co. KGaA: **2010**, p 147-174.

(12) Friend, N. C. G. a. R. H. In *Organic Light-Emitting Devices: A survey*; Shinar, J., Ed.; Springer-Verlag New York: **2004**, p 127-153.

(13) Prota, G. *Melanins and Melanogenesis*; Academic Press: San Diego, **1992**.

(14) Pezzella, A.; Wünsche, J. In *Organic Electronics: Emerging Concepts and Technologies*; Cicoira, F., Santato, C., Eds.; Wiley-VCH Verlag GmbH & Co. KGaA: **2013**, p 113-137.

(15) Strube, O. I.; Büngeler, A.; Bremser, W. Site-Specific In Situ Synthesis of Eumelanin Nanoparticles by an Enzymatic Autodeposition-Like Process. *Biomacromolecules* **2015**, *16*, 1608-1613.

(16) Mostert, A. B.; Powell, B. J.; Pratt, F. L.; Hanson, G. R.; Sarna, T.; Gentle, I. R.; Meredith, P. Role of semiconductivity and ion transport in the electrical conduction of melanin. *Proceedings of the National Academy of Sciences* **2012**, *109*, 8943-8947.

(17) Kim, Y. J.; Khetan, A.; Wu, W.; Chun, S.-E.; Viswanathan, V.; Whitacre, J. F.; Bettinger, C. J. Evidence of Porphyrin-Like Structures in Natural Melanin Pigments Using Electrochemical Fingerprinting. *Advanced Materials* **2016**, *28*, 3173-3180.

(18) Wünsche, J.; Cardenas, L.; Rosei, F.; Cicoira, F.; Gauvin, R.; Graeff, C. F. O.; Poulin, S.; Pezzella, A.; Santato, C. In Situ Formation of Dendrites in Eumelanin Thin Films between Gold Electrodes. *Advanced Functional Materials* **2013**, *23*, 5591-5598.

(19) Meredith, P.; Sarna, T. The physical and chemical properties of eumelanin. *Pigment Cell Res* **2006**, *19*, 572-594.

(20) Selvaraju, S.; Niradha Sachinthani, K. A.; Hopson, R. A.; McFarland, F. M.; Guo, S.; Rheingold, A. L.; Nelson, T. L. Eumelanin-inspired core derived from vanillin: a new building block for organic semiconductors. *Chemical Communications* **2015**, *51*, 2957-2959.

(21) Selvaraju, S.; Adhikari, S.; Hopson, R. A.; Dai, S.; Rheingold, A. L.; Borunda, M. F.; Nelson, T. L. Effects of structural variations on the optical and electronic properties of eumelanin-inspired small molecules. *Journal of Materials Chemistry C* **2016**, *4*, 3995-3999.

(22) Egbe, D. A. M.; Neugebauer, H.; Sariciftci, N. S. Alkoxy-substituted poly(arylene-ethynylene)-alt-poly(arylene-vinylene)s: synthesis, electroluminescence and photovoltaic applications. *Journal of Materials Chemistry* **2011**, *21*, 1338-1349.

(23) Egbe, D. A. M.; Carbonnier, B.; Birckner, E.; Grummt, U.-W. Arylene-ethynylene/arylene-vinylene copolymers: Synthesis and structure–property relationships. *Progress in Polymer Science* **2009**, *34*, 1023-1067.

(24) Liu, B.; Yu, W.-L.; Pei, J.; Liu, S.-Y.; Lai, Y.-H.; Huang, W. Design and Synthesis of Bipyridyl-Containing Conjugated Polymers: Effects of Polymer Rigidity on Metal Ion Sensing. *Macromolecules* **2001**, *34*, 7932-7940.

(25) Torres, J. M.; Wang, C.; Coughlin, E. B.; Bishop, J. P.; Register, R. A.; Riggleman, R. A.; Stafford, C. M.; Vogt, B. D. Influence of Chain Stiffness on Thermal and Mechanical Properties of Polymer Thin Films. *Macromolecules* **2011**, *44*, 9040-9045.

(26) Shavit, A.; Riggleman, R. A. Influence of Backbone Rigidity on Nanoscale Confinement Effects in Model Glass-Forming Polymers. *Macromolecules* **2013**, *46*, 5044-5052.

(27) Shen, P.; Sang, G.; Lu, J.; Zhao, B.; Wan, M.; Zou, Y.; Li, Y.; Tan, S. Effect of 3D π−π Stacking on Photovoltaic and Electroluminescent Properties in Triphenylamine-containing Poly(p-phenylenevinylene) Derivatives. *Macromolecules* **2008**, *41*, 5716-5722.

(28) Li, S.; Zhao, P.; Huang, Y.; Li, T.; Tang, C.; Zhu, R.; Zhao, L.; Fan, Q.; Huang, S.; Xu, Z.; Huang, W. Poly-(p-phenylene vinylenes) with pendent 2,4-difluorophenyl and fluorenyl moieties: Synthesis, characterization, and device performance. *Journal of Polymer Science Part A: Polymer Chemistry* **2009**, *47*, 2500-2508.

CHAPTER V

NOVEL ORGANIC CONDUCTIVE FIBERS AS NON-METALLIC ELECTRODES AND NEURAL INTERCONNECTS

5.1 INTRODUCTION

The ability to measure, as well as modulate electrical activity associated with the human central nervous system, has emerged as invaluable for the diagnosis and management of a growing number of conditions over the past 60 years.[1] Electroencephalography (EEG) allows clinicians to recognize brain wave patterns related to various syndromes such as abnormal synchronous electrical discharges characteristic of seizure disorders. Electromyography (EMG) helps localize and diagnose muscle and peripheral nerve disease. Electrocardiography (ECG) helps assess the electrical and muscular functions of the heart. Stimulation of the nervous system has led to revolutionary treatments for movement disorders like Parkinson's disease, dystonia, and tremor, as well as psychiatric conditions and pain disorders.[2] Neuromodulation, based on the recording and delivery of electrical signals, has allowed researchers and physicians to diagnose and treat conditions in the absence of anatomic abnormalities.[3] Most neural recording and stimulating electrodes are metallic. While highly efficient conductors of electric charge, metals present several important disadvantages, such as poor biocompatibility properties which lead to reactive, gliotic changes in neural tissue which, in turn, leads to increasing impedances of the interface to

the tissue.[4] Metals used as current injectors (e.g. platinum and iridium) are expensive and fragile,[5] and the resistance inherent in metallic conductors causes energy to be dissipated as heat, which can worsen reactive changes in the surrounding tissues.[6]

The next generation neural interfaces will be designed to eliminate or minimize the above concerns. The working hypothesis is that new electrodes should be based on material substrates which have an organic composition. The new electrically conductive organic electrodes will both capture and deliver adequate electrical currents, while promoting neural integration with reduced tissue injury and inflammation. This will be accomplished through the enhanced biocompatibility of these organic materials when compared to metals. These materials can also allow for the development of more cost-effective devices, since the expense of organic conductive materials will be significantly lower than precious metals.

In the last few years, electrically conductive fibers (ECFs) made from organic materials have emerged as an attractive and promising class of materials for the realization of non-metallic interconnects for medical applications.[7-13] The conductive inks for the ECFs have been comprised of conjugated polymers (CPs),[13-17] carbons,[10,18] carbon/electrolyte[19] or carbon/polymer composite.[9,20] In this chapter, the investigation on the utilization of a conductive ink composed of a CP/carbon nanotube assembly to stain natural and synthetic fibers for fabrication of organic ECFs will be discussed. The CPs have been known to disperse carbon nanotubes (CNTs) very efficiently in organic solvents.[21] Furthermore, both of these materials are conductive with CNTs being highly electrical conductive with good thermal/photo-stability and high mechanical strength. In this study, the organic ECFs were fabricated using commercially available, non-conductive, cotton, silk and polyester sutures stained with a conductive ink made from a regioregular poly(3-hexylthiophene). The (rr-P3HT)/SWCNT assembly materials were examined for their ability to serve as non-metallic electrodes and neural interconnects.

5.2 RESULTS AND DISCUSSION

5.2.1 Preparation of Electrically Conductive Fibers

The conductive ink was prepared by the addition of SWCNTs to the rr-P3HT solution in $CHCl_3$. The resulting mixture was ultrahigh sonicated using a Microson Ultrasonic Cell Disruptor for 30 minutes in an ice bath to avoid overheating and undesirable secondary reactions. A dipping and drying technique was utilized to stain the fibers with the conductive ink. After staining, the fibers were oven dried for 15 minutes at 100 °C.

5.2.2 Dependence of Conductive Ink Content and Number of Deposition Cycles

The dependence of the conductive ink content and the number of deposition cycles with respect to the conductivity of the fiber were investigated. To optimize the concentration of the SWCNTs, three different concentrations of SWCNTs (0.5, 0.8 and 1.2 mg/mL) were used to prepare the conductive ink while keeping the SWCNT:rr-P3HT ratio of 1:2 constant and the electrical resistance data are listed in Table 5.1. It was found that SWCNT concentration of 0.8 mg/mL yielded relatively low resistance of 0.39 ± 0.04 kΩ/cm.

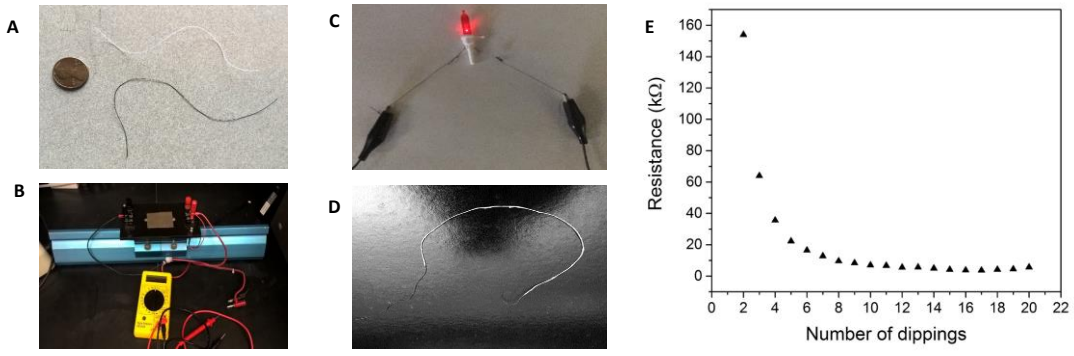

Figure 5.1: A) Picture of original and stained fiber, B) In-house built apparatus setup for electrical DC resistance measurements, C) lightening of the LED bulb using organic ECF, D) Organic ECF coated with outer insulating material, and E) dependence of the number of depositions on electrical resistance of organic ECF.

Table 5.1: Electrical resistance of the coated cotton obtained by varying concentration of SWCNTs with constant SWCNT:rr-P3HT ratio.

SWCNT:rr-P3HT	Concentration of SWCNT	Resistance (kΩ/cm)
1:2	0.5 mg/mL	0.78 ± 0.07
1:2	0.8 mg/mL	0.39 ± 0.04
1:2	1.2 mg/mL	0.61 ± 0.26

Once the concentration of SWCNT was optimized, then the ratio of the SWCNT to rr-P3HT was investigated by keeping the SWCNTs concentration constant (0.8 mg/mL) and the electrical resistance data are listed in Table 5.2. It was found that 1:2 ratio of SWCNT to rr-P3HT provided relatively low resistance of 0.39 ± 0.04 kΩ/cm.

Table 5.2: Electrical resistance of the coated cotton obtained by changing the SWCNT:rr-P3HT ratio with constant SWCNTs concentration.

SWCNT:rr-P3HT	Concentration of SWCNT	Resistance (kΩ/cm)
1:1	0.8 mg/mL	0.48 ± 0.05
1:2	0.8 mg/mL	0.39 ± 0.04
1:3	0.8 mg/mL	0.69 ± 0.06

The organic ECFs stained with the conductive ink having a composition of 0.8 mg/mL of SWCNTs with a 1:2 ratio of SWCNTs to rr-P3HT gave the lowest electrical resistance of 0.39 kΩ/cm. The conductive fibers also exhibited the conductance dependence on deposition cycles. Figure 5.1E shows the dependence of electrical resistance of the fiber as a function of the number of deposition cycles. The fiber was found to be conductive after one deposition cycle and became more conductive with each deposition cycle. However, after 10 deposition cycles, the electrical resistance of the fiber plateaued and remained unchanged. This is attributed to the adsorption of the SWCNTs on to the fiber which made it conductive. When an optimum amount of SWCNTs was deposited on the fiber, further addition did not affect its conductivity. These optimized conditions were used to further fabricate the organic ECFs from non-conductive fibers, such as cotton, polyester and silk, to study their electrical, morphological and mechanical properties.

All these stained fibers are conductive enough to light the LED bulb as shown in Figure 5.1C. Further, these organic ECFs were successfully coated with outer insulating material (see Figure 5.1D) using Flex Seal retaining its original conductivity.

Table 5.3: Electrical and mechanical properties of the conductive fibers.

Fiber type	Resisistance ($k\Omega\ cm^{-1}$)	Young's Modulus (MPa)	Ultimate Breaking Stress (MPa)	Elongation at Break Point (%)
Original Cotton	>2000	269 ± 36	1214 ± 173	6.0 ± 0.3
rr-P3HT/SWCNTs + cotton	0.50 ± 0.06	257 ± 17	1402 ± 30	7.9 ± 0.2
Original polyester	>2000	127 ± 10	2833 ± 127	30.7 ± 0.5
rr-P3HT/SWCNTs + polyester	0.65 ± 0.10	76 ± 4	2915 ± 289	40.0 ± 1.3
Original silk	>2000	305 ± 32	3920 ± 34	13.1 ± 0.9
rr-P3HT/SWCNTs + silk	0.73 ± 0.19	241 ± 23	3414 ± 69	15.9 ± 0.3

5.2.3 Effect of Molecular Weight of rr-P3HT

Two different molecular weights of rr-P3HT (M_w = 22 kDa and 12 kDa) were used in order to investigate the effect of the molecular weight of rr-P3HT on the electrical resistance of the stained fibers. While rr-P3HT with M_w = 22 kDa was purchased, rr-P3HT with M_w = 12 kDa was synthesized according to the previously reported procedure.[22] It was found that the cotton fibers stained with the conductive ink made from low molecular weight rr-P3HT gave lower resistance (0.45 kΩ) than with higher molecular weight (0.65 kΩ). A similar trend was found in the case of polyester and silk fibers. It may be attributed to the better dispersion of SWCNTs by low molecular weight rr-P3HT compared to the higher molecular weight polymer.

5.2.4 Electrical Measurement

The resistance of the organic ECFs was measured by using our in-house built apparatus (Figure 5.1B). The results are shown in Table 5.3, and the data are the average of three different conductive fibers of each type. The resistance of the unstained fibers could not be measured by the given apparatus as it was above 2 MΩ. The organic ECFs obtained from cotton had slightly less electrical resistance compared to those obtained from polyester and silk. This result could be due to the better adsorption of conductive ink by the porous cotton fibers.

5.2.5 Effect of Doping on Conductive Fibers

Different dopants were used to dope the rr-P3HT/SWCNTs composite to study the effects on the conductivity of the conductive cotton fibers. Different dopants used and their effects on the conductivity of the fibers are discussed below.

Iodine: The resistance of the conductive fiber was reduced to 180 Ωcm^{-1} from 720 Ωcm^{-1} after doping with iodine for overnight.

DMSO: The conductive fiber was dipped onto DMSO for overnight and was dried in preheated oven (100 °C) until it dried. The resistance of the conductive fiber remained almost the same or less after doping with DMSO.

Poly(styrene sulfonic acid) (PSS): The conductive fiber was dipped onto PSS solution (18% weight in water) for overnight and was dried in preheated oven (100 °C) until it dried. PSS increased the resistance of the conductive fiber and the fiber became stiffer and was broken easily. The increase in resistance of the fiber after treating with the PSS solution may be attributed to the formation of an insulating coating of PSS on the conductive fiber. In different experiment, PSS solution was added to the $CHCl_3$ solution containing SWCNTs, and P3HT and ultrahigh sonicated to make doped conductive ink. This doped conductive ink was used to make

conductive fibers. However, the resistance of the stained fiber with doped conductive ink was less (3.2 $k\Omega cm^{-1}$) compared to the undoped conductive fibers (2.5 $k\Omega\ cm^{-1}$).

2,3,5,6-Tetrafluoro-7,7,8,8-tetracyanoquinodimethane (F4TCNQ): F4TCNQ was added to the $CHCl_3$ solution containing SWCNTs and P3HT while making conductive ink. This composition of conductive ink was used to make conductive fibers, but it also did not help in reducing the resistance of the stained fibers.

5.2.6 Raman spectroscopy

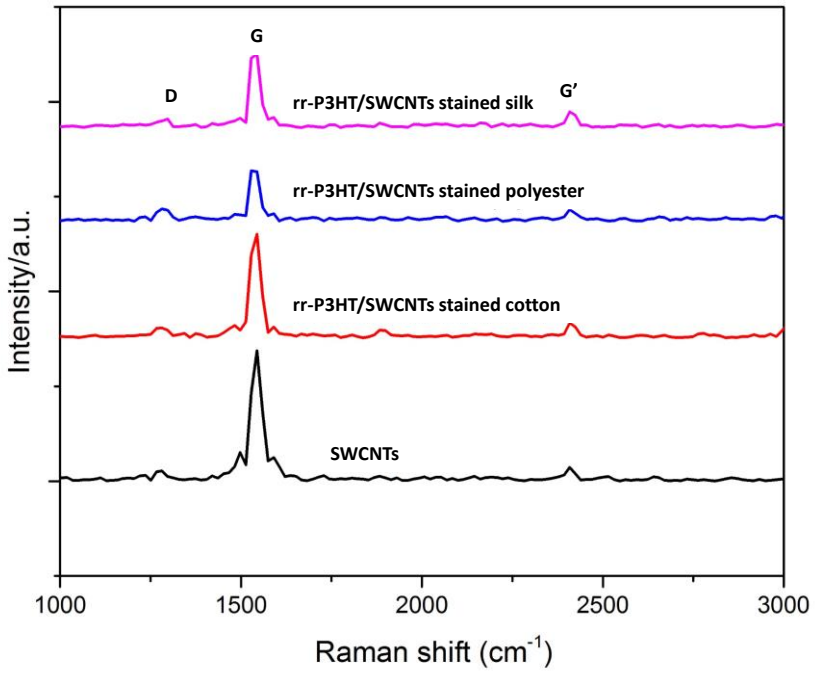

Figure 5.2: Raman spectra of SWCNTs and rr-P3HT/SWCNT stained fibers.

In order to provide evidence for the presence of SWCNTs, the organic ECFs were examined using Raman spectroscopy. The Raman spectra of the three organic ECFs and SWCNTs are shown in Figure 5.2. The characteristic D–band (~ 1277 cm^{-1}) and G–band (~ 1540 cm^{-1}) for SWCNTs can be clearly observed on all three organic ECFs. Additionally, the second order band

at (~ 2407cm^{-1}) is also clearly identified in all the organic ECFs implying the presence of SWCNTs in all stained fibers.

5.2.7 Stress-strain Measurement

The mechanical strength of the fibers was characterized by stress-strain measurements. Three mechanical parameters, namely the Young's Modulus, the ultimate breaking stress and the elongation at break point, were measured. The mean values of such parameters for all original and stained fibers are reported in Table 5.1, and stress-strain plots are shown in Figure 5.3.

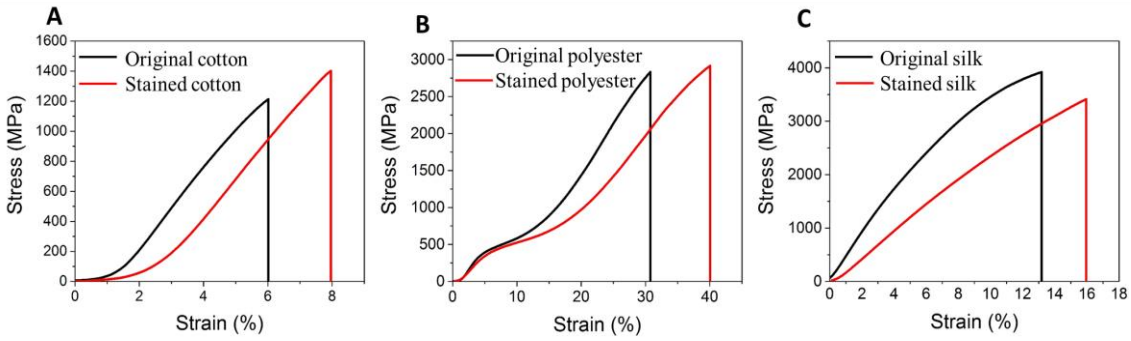

Figure 5.3: Stress-strain plots for; a) original and stained cotton, b) original and stained silk and c) original and stained polyester.

Based on the data, two main observations were made. First, the maximum elongation of the material before breaking was found to increase in the stained fibers compared to the original, unstained material. Thus, an advantageous ability of the fiber to be woven or knitted was preserved in the stained fibers. Second, a decrease in Young's modulus was observed in all the stained fibers, indicating that the conductive ink coating decreased the stiffness of the fiber. This property of the stained fibers may be attributed to a lubricant effect of the rr-P3HT/SWCNT assembly which seems to enable fiber strands to slide on one another following the application of mechanical stimulus.[15]

5.2.8 Morphology Characterization

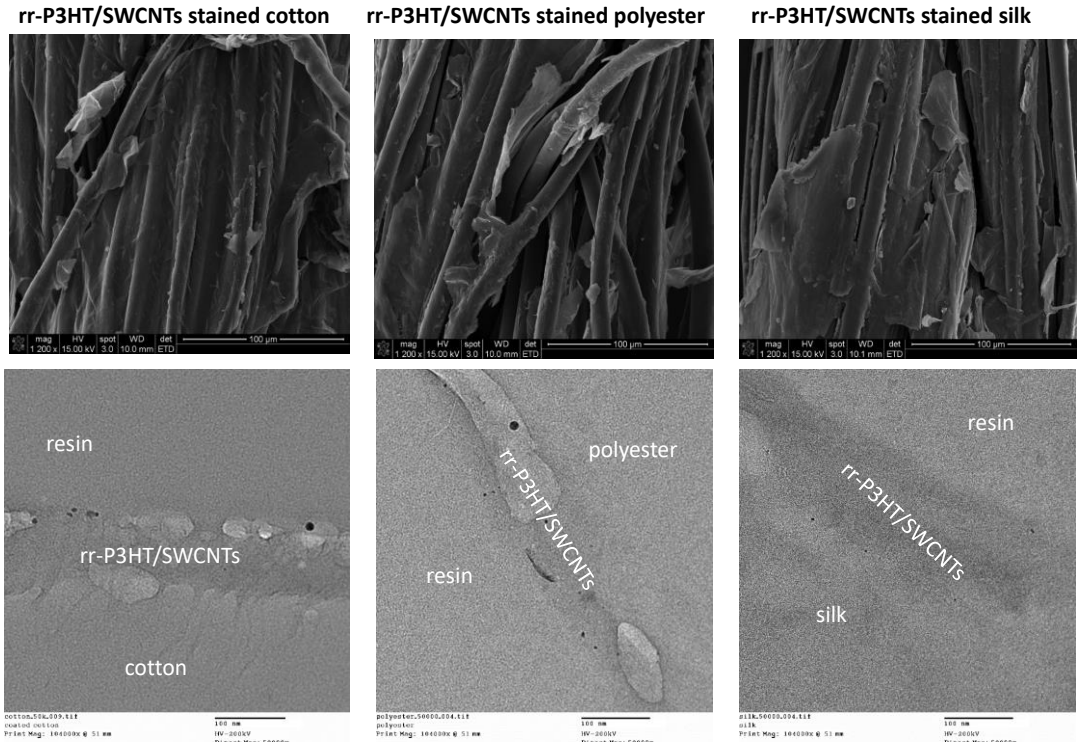

Figure 5.4: Scanning electron microscopy (top) and transmission electron microscopy (bottom) images of organic ECFs.

The morphology of the three different ECFs obtained after 10 depositions cycles was analyzed using Scanning electron microscopy (SEM) (Figure 5.4). SEM images show that conductive ink has stained the exterior of every strand of each observable fiber and has also filled the gap between these strands. Furthermore, TEM images were taken to provide evidence of the presence of SWCNTs on the organic ECFs. In Figure 5.4, TEM images clearly display the stained region on each type of fibers and the presence of carbon nanotubes which appear as darker spots on the stained region.

5.2.9 Surface Electrical Signal Measurements

In these preliminary experiments, the ability of the ECFs to transduce skin surface biological electrical signals was investigated and the results were compared to measurements obtained using

commercially available 9 mm Grass Gold Cup electrodes. These experiments were done on a 34 year old male. In all cases, the stained fibers could successfully record EMG and ECG data. The skin of the subject's palms was prepared with Nuprep Skin Prep Gel. Ten20 conductive paste was then used to fill the cup of the Grass Gold Cup electrodes which were placed over the subjects left thenar and hypothenar muscles as shown in Figure 5.5C. A ground lead was placed over the left forearm. Electrode/skin impedances were measured at 28.8 kΩ and 35.6 kΩ for both the thenar and hypothenar leads. Single channel compound muscle potentials (an EMG variant) were recorded during thumb twitch between the thenar and hypothenar leads. The experiment was repeated with stained polyester fibers. To provide for connecting the stained fibers to the recording system, the stained fibers were attached to the grass gold cup electrodes using Ten20 paste and then placed over thenar and hypothenar muscles as seen in Figure 5.5D. Care was taken that Grass Gold Cup electrodes made no contact with the subject's skin. In this experiment, impedances were recorded at 38.0 kΩ and 18.6 kΩ for thenar and hypothenar leads. The compound muscle potentials were once again recorded across leads during thumb twitch. Representative recordings can be seen in Figure 5.5A for Grass Gold Cup electrodes (Epoch 49) and 5.5B for stained polyester ECF (Epoch 164). EMG recording with Grass Gold Cup electrodes yielded a maximum amplitude of 1787 μV, compared to a maximum amplitude of 1473 μV for the ECFs. Although the voluntary thumb twitch is subject to variability and not precisely reproducible, classic compound muscle potential morphology can easily be identified in both the Grass Gold Cup and ECF trials.

In a second experiment, equivalent to recording the Axis I ECG, the skin of the subject's palms was prepared with Nuprep Skin Prep Gel. Ten20 conductive paste was then used to fill the cup of the Grass Gold Cup electrodes with were placed over the subjects left and right thenar muscles as shown in Figure 5.6C. A ground lead was placed over the left forearm. Impedances were recorded at 20.3 kΩ and 19.0 kΩ for left and right thenar leads. The single channel ECG (Axis I)

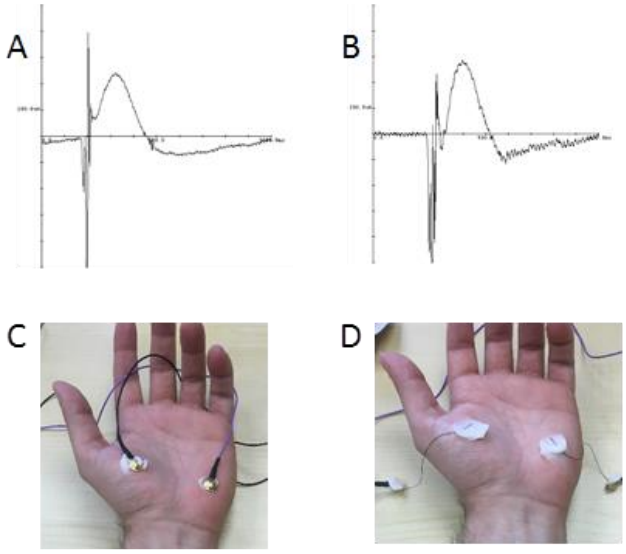

Figure 5.5: Measurements of skin surface electrodes. Compound muscle potentials (EMG varient) recording between thenar and hypothenar muscles using Grass Gold Cup electrodes (A,C) and stained polyester ECF (B,D).

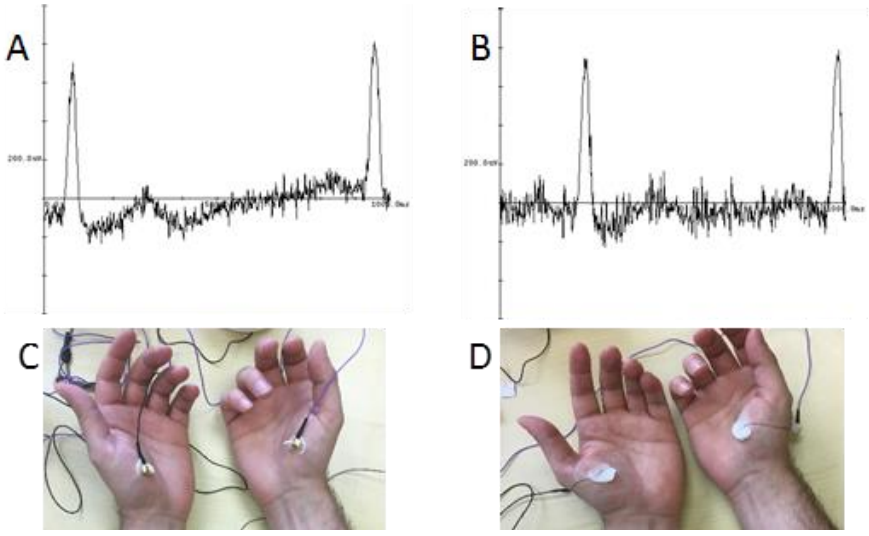

Figure 5.6: Measurements of skin surface electrodes. ECG recording across left and right thenar muscles using Grass Gold Cup electrodes (A,C) and stained polyester ECF (B,D).

was recorded during rest between the left and right palmar leads over the thenar muscles. The experiment was again repeated with stained polyester fibers. The stained fibers were connected to the Grass Gold Cup electrodes using Ten20 paste and then placed over the thenar muscles as

seen in Figure 5.6D. Care was taken that grass gold cup electrodes made no contact with subject's skin. Impedances were recorded at 39.3 kΩ and 18.4 kΩ for the left and right thenar leads. The ECG was once again recorded between leads during rest. A representative ECG signal can be seen in Figure 5.6A for Grass Gold Cup electrodes (Epoch 95) and 6B for stained polyester ECF (Epoch 213). ECG recording with Grass Gold Cup electrodes yielded a maximum amplitude of 816μV, compared to a maximum amplitude of 1108 μV using ECFs. ECG morphology can easily be identified in both Grass Gold Cup and ECF trials.

A notch filter was applied to all modalities prior to data collection. Artifact rejection was set at 80% and the Spike width at 5%. In all cases, the unstained fibers could not record any signal, and data were read as "open" channels by the system, due to electrode impendences being greater than 50 kΩ.

5.3 CONCLUSION

The work in this chapter demonstrated that a conductive ink from rr-P3HT/SWCNT assembly can be used to stain natural and synthetic fibers to generate electrically conductive fibers that retain the native materials mechanical and physical properties. The staining method yielded EFCs with resistance as low as 0.50 kΩ/cm using less of SWCNTs (0.8 mg/mL), while retaining the good mechanical properties of the original substrate. In addition, resistance reduction below 180 Ω/cm could be achieved by doping with iodine. Moreover, these organic ECFs were used to record skin surface biological signals with signal to noise ratios that were similar to or better than the data obtained by using standard metal electrodes. The results demonstrate the promise of these materials for use in modern medical diagnostics.

5.4 EXPERIMENTAL SECTION

5.4.1 Materials

Regioregular poly(3-hexylthiophene) (rr-P3HT), Mw = 22 kDa and single walled carbon nanotubes (SWCNTs) were purchased from American Dye Source, Inc. and Aldrich, respectively. Cotton, polyester and silk threads were purchased from Joann Fabrics and Crafts, and Surgical Specialties and were used without any chemical treatment.

5.4.2 Raman Spectroscopic Characterization

The organic ECFs were characterized using a Nicolet NXR 9610 Raman Spectrometer. The 976 nm excitation laser was used to obtain Raman spectra for all samples.

5.4.3 Electron Microscopy Analysis

The scanning electron microscopy (SEM) samples were prepared by mounting a piece of stained fiber on an aluminum stub. Samples were then coated with a very thin layer of palladium/gold metal deposited using a MED 010 sputter coater (Balzers, Oberkochen, Germany). SEM images were taken with a FEI Quanta 600 SEM with Evex EDS system (FEI, Hillsboro, OR). Transmission electron microscopy (TEM) samples were prepared as follows. Each sample was cut to 1 cm lengths which was embedded in Polybed 812 resin and cured for 36 h at 55 °C. Samples were then sectioned at 70 nm thickness on a RMC Product Powertome XL ultramicrotone using a Diatome diamond knife. Sections were then transferred to carbon square mesh TEM grids (EM Sciences, p/n CF15*0*-CU-UL). TEM images were taken on a JEOL JEM-2100 at 200KV with a Lab6 Filament.

5.4.4 Mechanical Characterization

The mechanical strength of the conductive fibers was characterized by means of stress-strain measurements performed on a TA instrument DMA Q800. The stress applied varied from 0 to 18 N with the linear ramp force 1.00 N/min. Strain was expressed as percentage elongation with respect to the sample's original length.

5.4.5 Electrical Characterization

The DC resistance measurements were obtained using an in-house built apparatus (see Figure 5.1B). Physiological signals (skin surface EMGs and EKGs) were recorded with 9 mm Gold Cup electrodes (Rochester Electro-Medical, Inc) on a NeuroNetVI system (CDI, Pittsburgh) which also measured skin-electrode impedances with an injected current at 400 Hz. All studies were done under the approval of Allegheny Singer Research Institutional Review Board Approval number RC-6318.

5.5 REFERENCES

(1) Marg, E.; Adams, J. E. Indwelling multiple micro-electrodes in the brain. *Electroencephalography and Clinical Neurophysiology* **1967**, *23*, 277-280.

(2) Miocinovic, S.; Somayajula, S.; Chitnis, S.; Vitek, J. L. History, applications, and mechanisms of deep brain stimulation. *JAMA neurology* **2013**, *70*, 163-171.

(3) Sun, F. T.; Morrell, M. J. Closed-loop neurostimulation: the clinical experience. *Neurotherapeutics : the journal of the American Society for Experimental NeuroTherapeutics* **2014**, *11*, 553-563.

(4) Satzer, D.; Lanctin, D.; Eberly, L. E.; Abosch, A. Variation in Deep Brain Stimulation Electrode Impedance over Years Following Electrode Implantation. *Stereotactic and Functional Neurosurgery* **2014**, *92*, 94-102.

(5) Fattahi, P.; Yang, G.; Kim, G.; Abidian, M. R. A Review of Organic and Inorganic Biomaterials for Neural Interfaces. *Advanced Materials* **2014**, *26*, 1846-1885.

(6) Elwassif, M. M.; Kong, Q.; Vazquez, M.; Bikson, M. Bio-heat transfer model of deep brain stimulation-induced temperature changes. *Journal of neural engineering* **2006**, *3*, 306-315.

(7) Tarabella, G.; Villani, M.; Calestani, D.; Mosca, R.; Iannotta, S.; Zappettini, A.; Coppede, N. A single cotton fiber organic electrochemical transistor for liquid electrolyte saline sensing. *Journal of Materials Chemistry* **2012**, *22*, 23830-23834.

(8) Wu, Y.; Wang, L.; Guo, B.; Ma, P. X. Interwoven Aligned Conductive Nanofiber Yarn/Hydrogel Composite Scaffolds for Engineered 3D Cardiac Anisotropy. *ACS Nano* **2017**, *11*, 5646-5659.

(9) Shim, B. S.; Chen, W.; Doty, C.; Xu, C.; Kotov, N. A. Smart Electronic Yarns and Wearable Fabrics for Human Biomonitoring made by Carbon Nanotube Coating with Polyelectrolytes. *Nano Letters* **2008**, *8*, 4151-4157.

(10) Mostafalu, P.; Akbari, M.; Alberti, K. A.; Xu, Q.; Khademhosseini, A.; Sonkusale, S. R. A toolkit of thread-based microfluidics, sensors, and electronics for 3D tissue embedding for medical diagnostics. *Microsystems &Amp; Nanoengineering* **2016**, *2*, 16039.

(11) Stoppa, M.; Chiolerio, A. Wearable Electronics and Smart Textiles: A Critical Review. *Sensors* **2014**, *14*, 11957.

(12) Coppede, N.; Tarabella, G.; Villani, M.; Calestani, D.; Iannotta, S.; Zappettini, A. Human stress monitoring through an organic cotton-fiber biosensor. *Journal of Materials Chemistry B* **2014**, *2*, 5620-5626.

(13) Hamedi, M.; Forchheimer, R.; Inganas, O. Towards woven logic from organic electronic fibres. *Nat Mater* **2007**, *6*, 357-362.

(14) Ryan, J. D.; Mengistie, D. A.; Gabrielsson, R.; Lund, A.; Müller, C. Machine-Washable PEDOT:PSS Dyed Silk Yarns for Electronic Textiles. *ACS Applied Materials & Interfaces* **2017**, *9*, 9045-9050.

(15) Mattana, G.; Cosseddu, P.; Fraboni, B.; Malliaras, G. G.; Hinestroza, J. P.; Bonfiglio, A. Organic electronics on natural cotton fibres. *Organic Electronics* **2011**, *12*, 2033-2039.

(16) Abidian, M. R.; Corey, J. M.; Kipke, D. R.; Martin, D. C. Conducting-polymer nanotubes improve electrical properties, mechanical adhesion, neural attachment, and neurite outgrowth of neural electrodes. *Small* **2010**, *6*, 421-429.

(17) Irwin, M. D.; Roberson, D. A.; Olivas, R. I.; Wicker, R. B.; MacDonald, E. Conductive polymer-coated threads as electrical interconnects in e-textiles. *Fibers and Polymers* **2011**, *12*, 904.

(18) Zhang, W.; Tan, Y. Y.; Wu, C.; Silva, S. R. P. Self-assembly of single walled carbon nanotubes onto cotton to make conductive yarn. *Particuology* **2012**, *10*, 517-521.

(19) Guinovart, T.; Parrilla, M.; Crespo, G. A.; Rius, F. X.; Andrade, F. J. Potentiometric sensors using cotton yarns, carbon nanotubes and polymeric membranes. *Analyst* **2013**, *138*, 5208-5215.

(20) Xue, P.; Park, K. H.; Tao, X. M.; Chen, W.; Cheng, X. Y. Electrically conductive yarns based on PVA/carbon nanotubes. *Composite Structures* **2007**, *78*, 271-277.

(21) Tuncel, D. Non-covalent interactions between carbon nanotubes and conjugated polymers. *Nanoscale* **2011**, *3*, 3545-3554.

(22) Loewe, R. S.; Ewbank, P. C.; Liu, J.; Zhai, L.; McCullough, R. D. Regioregular, Head-to-Tail Coupled Poly(3-alkylthiophenes) Made Easy by the GRIM Method: Investigation of the Reaction and the Origin of Regioselectivity. *Macromolecules* **2001**, *34*, 4324-4333.

CHAPTER VI

BENZODITHIOPHENE-*S*,*S*-TETRAOXIDE BASED NOVEL N-TYPE ORGANIC SEMICONDUCTORS

6.1 INTRODUCTION

After the discovery of the first highly conducting polymer in 1977[1], organic semiconductors (OSCs) have enticed scientific communities for their application in organic light emitting diodes (OLEDs)[2], thin film transistors (TFTs)[3], solar cells[4], sensors[5], conductive fibers[6], etc. It is mainly due to the fact that OSCs offer several advantages over their inorganic counterparts. For example, low cost, flexible, and large area devices can be achieved as OSCs can be solution processed at low temperatures and have mechanically flexible properties. Further, the material properties (such as optical, electronic, morphology etc.) can be fine-tuned simply by modifying the structure of the molecule through intelligent molecular design.[7,8] OSCs, including both small molecules and polymers, are commonly classified as p-type and n-type, in which the major charge carriers are holes and electrons, respectively. While p-type OSCs have seen dramatic rise in performance over the last decade, n-type OSCs, in general, still lag behind p-type OSCs. This lack of high performance n-type OSCs is mainly related to the stability, difficulties in the synthesis of these materials and the scarcity of electron deficient building blocks that can be used to synthesize stable n-type OSCs.[9,10] Both types of OSCs with high performance are required in

order to fabricate high-performance complementary circuits or p-n junction devices. Thus, there is a critical need for exploration of new building blocks for making novel n-type OSCs with improved electron mobility, material stability both under processing and operational conditions, and ease of synthesis.

While benzodithiophenes have been extensively explored in making high performance p-type OSCs[11], their oxidized counterpart benzo[1,2-*b*:4,5-*b*']dithiophene-1,1,5,5-tetraoxide (BDTT), has been less utilized as a building block to make n-type OSCs despite it being an electron poor heterocycle with promise for development of n-type materials. One likely reason is carbon-carbon cross coupling reactions involving BDTT result in low yields.[12] In this chapter, the functionalization of BDTT using two different methodologies and utilization of functionalized BDTT to make BDTT based n-type small molecules and donor-acceptor polymers will be discussed.

6.2 BDTT BASED DONOR-ACCEPTOR POLYMERS

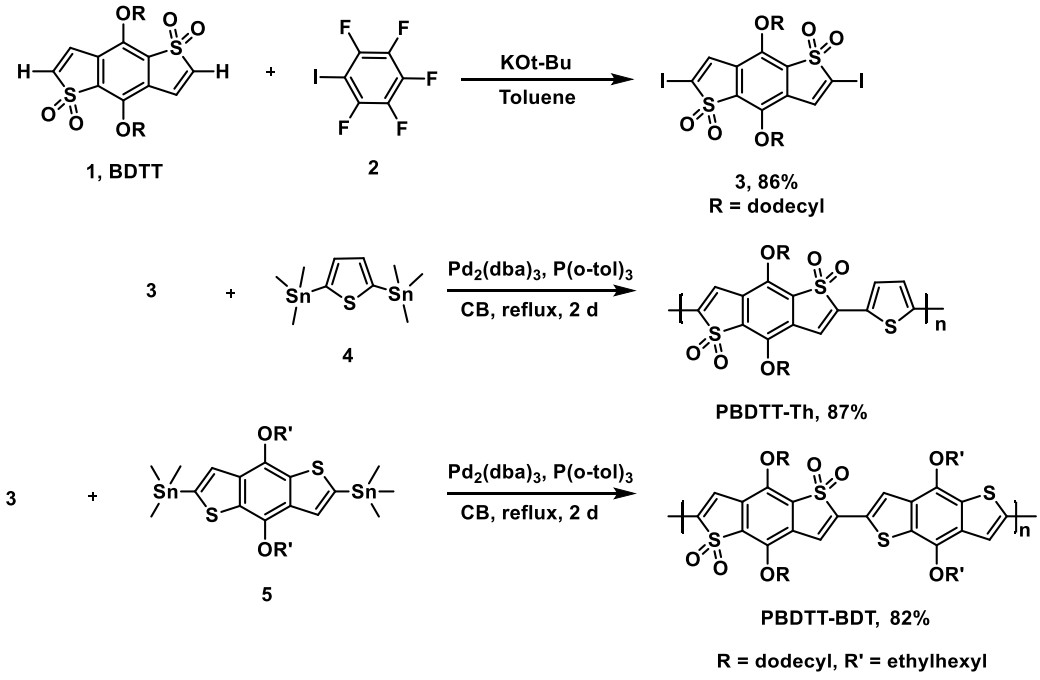

Scheme 6.1: Synthesis of monomers and polymers.

6.2.1 Results and Discussion

The synthetic routes for monomer, **3** and polymers PBDTT-Th and PBDTT-BDT are depicted in the scheme 6.1. The electrophilic halogenation reactions of BDTT either did not give the desired product or the yield was very low < 15%. BDTT was also tried to functionalize with strong bases and nucleophiles, but it was not stable in presence of strong bases and nucleophiles. Thus, the functionalization of BDTT was carried out by using recently developed C-H iodination of electron deficient substrates reactions developed by Qinqin and coworkers.[13] The iodination of BDTT with iodopentafluorobenzene in the presence of potassium *tert*-butoxide was optimized. A high yield of 86% was obtained with 4 equivalents of iodopentafluorobenzene and 0.5 equivalents of potassium tert-butoxide at room temperature. The PBDTT-Th and PBDTT-BDT copolymers were then synthesized by reacting compound **3** with 2,5-bis(trimethylstannyl)thiophene and (4,8-bis((2-ethylhexyl)oxy)benzo[1,2-b:4,5-b']dithiophene-2,6-diyl)bis(trimethylstannane) respectively under Stille copolymerization conditions. The percent yield, number average molecular weight (Mn), and polydispersity index (PDI) of these polymers are shown in Table 6.1. After Soxhlet extraction and reprecipitation, PBDTT-Th and PBDTT-BDT was obtained in high yields of 87% and 82% and moderate number average molecular weights of 10.7 and 14.4 kDa, respectively. PBDTT-BDT was highly soluble in common solvents like THF, toluene and chlorinated solvents such as DCM, chloroform, and chlorobenzenes while PBDTT-Th was soluble in chloroform and chlorobenzenes and moderately soluble in THF and DCM. The reduced solubility of PBDTT-Th compared to PBDTT-BDT is due to the absence of any alkyl chain on thiophene unit of PBDTT-Th polymer. However, both polymers are sufficiently soluble in chlorobenzenes for their utilization in the solution processed electronic device fabrication.

The thermal properties of the polymers were investigated by thermal gravimetric analysis (TGA) and differential scanning calorimetry (DSC). The TGA curves are shown in Figure 6.1A and the data are summarized on Table 6.1. The TGA plots showed that both polymers exhibit good

thermal stabilities under N_2, indicating 5% decomposition at 335 °C for PBDTT-Th and 325 °C for PBDTT-BDT. DSC scans of the second cooling cycle for the polymers are shown in Figure 6.1B. In DSC thermograms, crystallization and melting transitions as well as glass transition temperatures were not observed in the scanned temperature range suggesting the amorphous nature of the polymers.

Table 6.1: Structural and thermal properties of polymers.

Polymer	M_n[a] (kDa)	M_w[a] (kDa)	PDI[a]	T_d[b] (°C)	T_g[b] (°C)
PBDTT-Th	10.7	38.5	3.6	335	-
PBDTT-BDT	14.4	34.5	2.4	325	-

[a] Determined by GPC in THF using polystyrene standards. [b] 5% weight loss temperature by TGA under N_2. [c] Data from second scan reported, heating rate 3 °C min^{-1} under N_2.

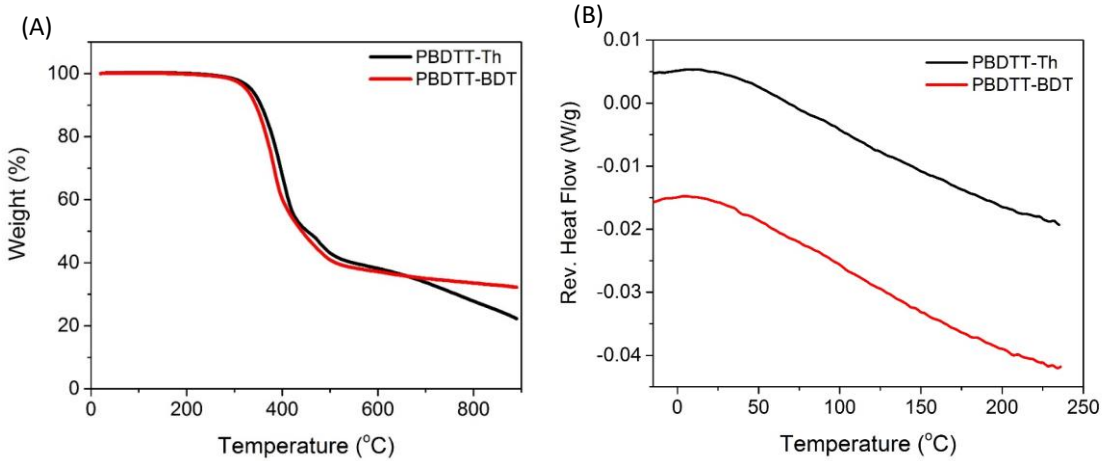

Figure 6.1: A) TGA and B) DCS curves of PBDTT-Th and PBDTT-BDT.

The optical properties of the polymers were investigated using UV-Vis absorption spectroscopy both in $CHCl_3$ solutions and as drop cast films from $CHCl_3$ solution. The normalized absorption spectra of the polymers are shown in Figure 6.2, and the results are summarized in Table 6.2. Both of these polymers showed broad absorption ranging from 400 nm to 725 nm. For PBDTT-Th, the absorption maxima of 595 nm and 577 nm were observed in solution and film

respectively whereas for PBDTT-BDT the absorption maxima were 619 nm and 574 nm in solution and film respectively. The red shifted absorption maximum for PBDTT-BDT compared PBDTT-Th is attributed to better conjugation in PBDTT-BDT due to having a high molecular weight. Hypsochromically shifted spectra were observed for both polymers upon film formation compared to those in solution, which was more pronounced in PBDTT-BDT. These spectral shifts suggest that these polymers have some preaggregates in solution due to strong intermolecular attraction of the large fused and rigid conjugated systems[14] and also due to the attraction among the sulfone groups.

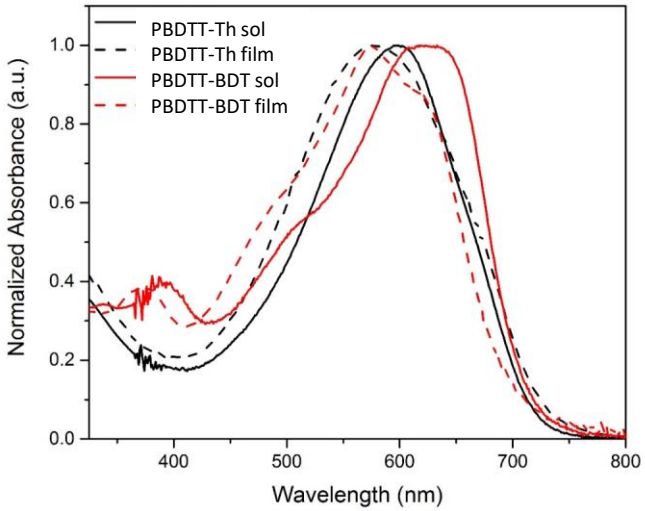

Figure 6.2: Absorption spectra of polymers in solution ($CHCl_3$, solid lines) and thin film (cast from $CHCl_3$, dashed lines).

The electronic properties of the polymers were determined by cyclic voltammetry by depositing thin films of these polymers on a working electrode; the results are summarized in Table 6.2, and the cyclic voltammograms are shown in Figure 6.7B and 6.7C (see experimental section). The LUMO of PBDTT-Th and PBDTT-BDT are -3.72 eV and -3.60 eV respectively which are quite similar while the HOMO of PBDTT-BDT (-5.47 eV) is higher in energy than that of PBDTT-Th (-5.74 eV). This is because these polymers have the same electron poor unit with different

electron rich units. Polymers that have alternating electron rich and electron poor conjugated repeat units typically have the HOMO energy levels that resemble the HOMO of the electron rich unit and the LUMO resembles the electron poor unit. The HOMO energy level of PBDTT-BDT is more shallow than that of PBDTT-Th due to having comparatively high electron rich unit benzodithiophene in PBDTT-BDT compared to thiophene unit in PBDTT-Th. This also causes a decrease in the electronic band gap of PBDTT-BDT polymer (1.87 eV) compared to PBDTT-Th (2.02 eV) as the high electron rich unit increases the HOMO making the band gap less in PBDTT-BDT.

Table 6.2. The optical and electronic properties of the polymers.

Polymers	Media	λ_{abs} (nm)[a]	ε (M^{-1})[a]	E_{ox} (V)[b]	E_{re} (V)[c]	HOMO (eV)[d]	LUMO (eV)[e]	E_g^{ec} (eV)[f]
PBDTT-Th	$CHCl_3$	595	4.99×10^5					
	Film	581		1.07	-0.95	-5.74	-3.72	2.02
PBDTT-BDT	$CHCl_3$	610	5.06×10^5					
	Film	584		0.80	-1.07	-5.47	-3.60	1.87

[a] Measured in dilute chloroform. [b & c] Measured from the onset of oxidation wave and reduction wave respectively. [d] Calculated from the onset of the first oxidation using the equations E_{HOMO} (eV) = - $[E_{ox}^{onset} - E_{1/2}(Fc/Fc^+) + 4.8]$ where $E_{1/2}$ (Fc/Fc^+) is the cell correction. [e] Calculated from the onset of the first reduction using the equation E_{LUMO} (eV) = - $[E_{red}^{onset} - E_{1/2}(Fc/Fc^+) + 4.8]$. [f] Calculated using the equation E_g^{ec} (eV) = HOMO – LUMO.

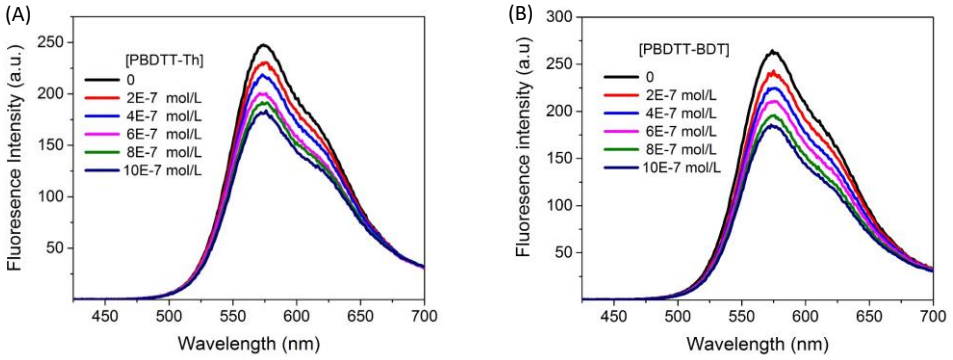

Figure 6.3: Fluorescence spectrum of P3HT (4.0×10^{-7} M) in chloroform with varying concentrations of the electron acceptor (A) PBDTT-Th and (B) PBDTT-BDT.

Both of these polymers did not show any significant emission. This gave us an opportunity to illustrate the electron accepting behavior of these polymers by performing fluorescence quenching experiments of a prototypical donor material, regioregular poly(3-hexylthiophene) (rr-P3HT).[15] Fluorescence quenching experiments with rr-P3HT as electron donor were conducted

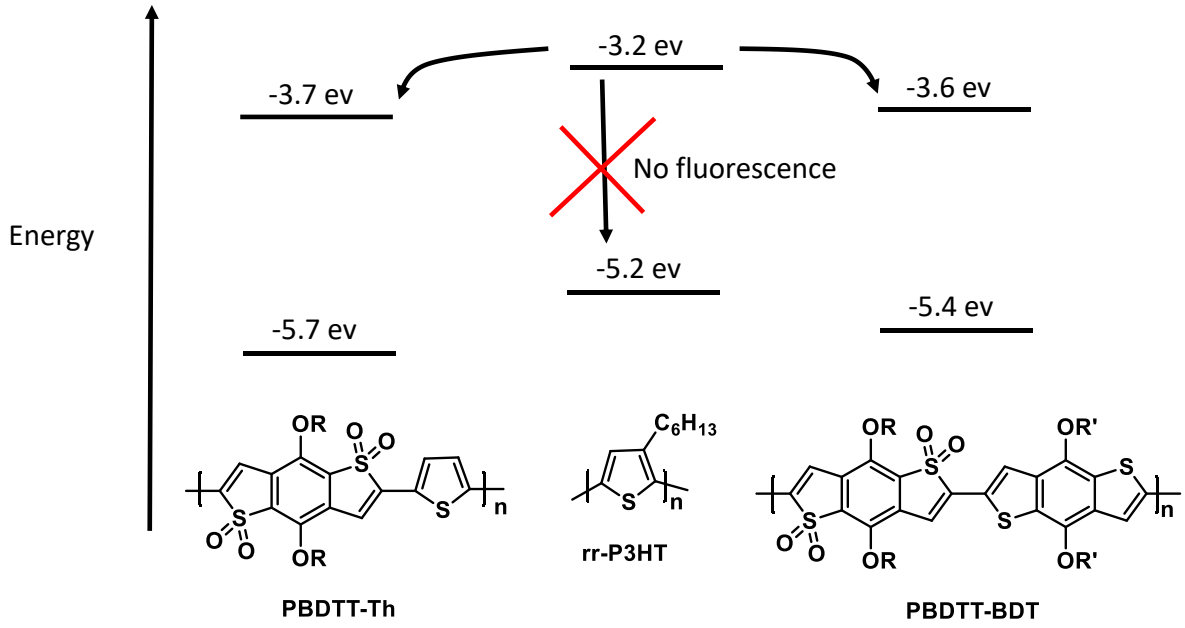

Figure 6.4: Illustration of electron transfer mechanism for fluorescence quenching of rr-P3HT

by varying concentrations of **PBDTT-Th** and **PBDTT-BDT**. Due to the absorbance of polymers **PBDTT-Th** and **PBDTT-BDT** at both the excitation (360 nm) and emission wavelengths, the inner filter effect correction was carried out to get the corrected fluorescence spectra of rr-P3HT. The fluorescence intensity of P3HT was corrected using an equation 1.[16]

$$\frac{F_{corr}}{F_{obs}} = CF = \frac{2.3dA_{ex}}{1 - 10^{-dA_{ex}}} 10^{gA_{em}} \frac{2.3sA_{em}}{1 - 10^{-sA_{em}}} \qquad (1)$$

Where F_{corr} *and* F_{obs} are the corrected and observed emission intensities, *s* is the excitation beam thickness (0.10 cm), *g* is the distance from the edge of the sample beam to the edge of the cuvette

(0.40 cm), and *d* is the width of the cuvette (1.0 cm). A_{ex} and A_{em} are the absorbance of the solution at the excitation and emission wavelengths (units of cm^{-1}).

The correction factor (CF) was calculated for each wavelength and the largest CF was observed for high concentration of both polymers (10^{-6} mol/L). The greatest CF was 2.1 for PBDTT-Th found at 585 nm and 2.3 for PBDTT-BDT found at 610 nm which were within the acceptable range (CF < 3).[16] The corrected fluorescence spectra of rr-P3HT with varying concentration of PBDTT-Th and PBDTT-BDT are shown in Figure 6.3A and 6.3B respectively. The observed fluorescence intensity of rr-P3HT was markedly reduced upon addition of PBDTT-Th and PBDTT-BDT indicating excellent quenching behavior of these polymers. The quenching behavior of these polymers is explained by a general electron-transfer mechanism as depicted in Figure 6.4 which involves the energetically favorable transfer of an electron from the LUMO of rr-P3HT (3.2 eV) to the LUMO of the acceptor polymers PBDTT-Th (3.7 eV) and PBDTT-BDT (3.6 eV).

Further, the quenching data was analyzed using the Stern−Volmer equation (2), which showed a linear fit and gave a quenching constant (K_{SV}) 3.7×10^5 $mol^{-1}L$ and 4.1×10^5 $mol^{-1}L$ for PBDTT-Th and PBDTT-BDT, respectively. These values were similar to the one obtained for $PC_{60}BM$. This data illustrates the good electron accepting properties of the two polymers.

$$\frac{F_o}{F} = 1 + Ksv[Q] \qquad (2)$$

Where F_o and F are the emission intensities of P3HT without and with quencher. *Ksv* is quenching constant and $[Q]$ is the molar concentration of quencher.

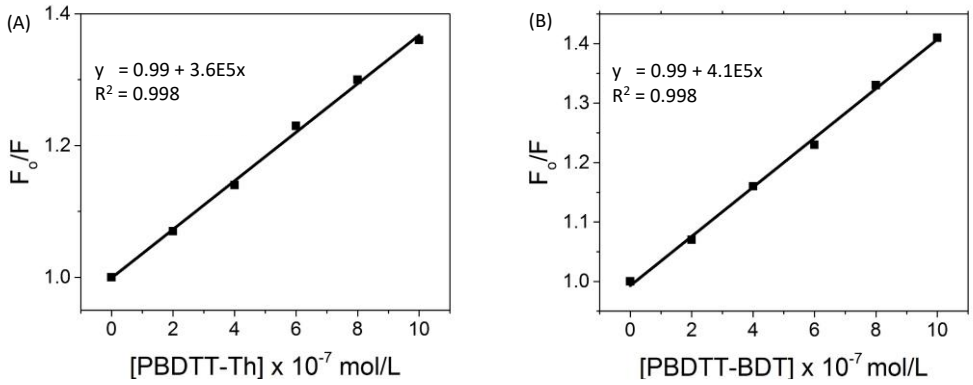

Figure 6.5: (A) Stern-Volmer plots for the data from Figure 6.3A and (B) Stern-Volmer plots for the data from Figure 6.3B.

6.3 BDTT BASED N-TYPE SMALL MOLECULES

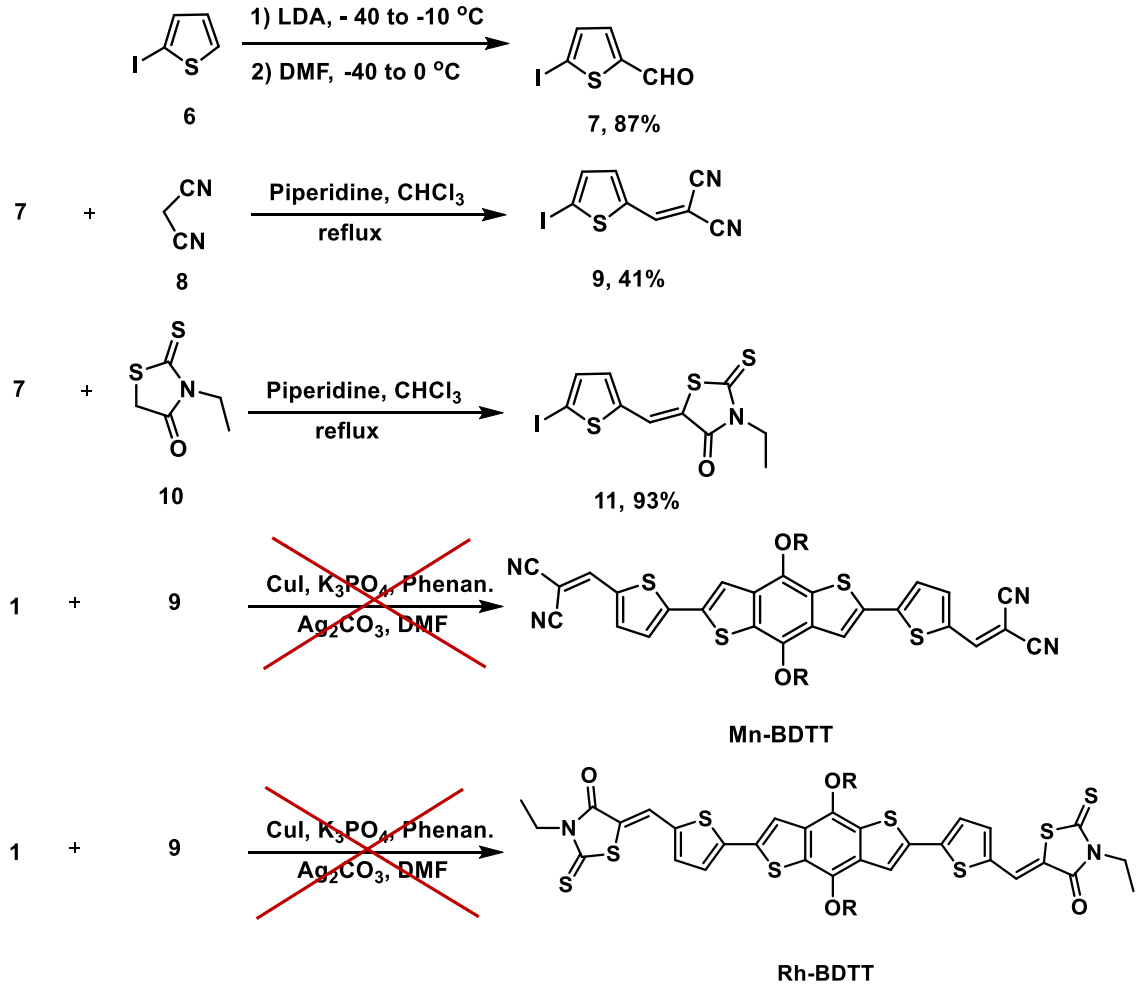

Scheme 6.2: Route 1 for the synthesis of BDTT based small molecules.

6.3.1 Results and Discussion

The two attempted synthetic routes for the synthesis of two BDTT based n-type small molecules Mn-BDTT and Rd-BDTT are given in Schemes 6.2 and 6.3. Here, copper catalyzed direct arylation reaction of BDTT to synthesize these small molecules was utilized. From the first route, depicted in Scheme 6.2, the desired product could not be achieved. The copper catalyzed direct arylation reactions between compounds **9** or **11** with BDTT in different temperature conditions also did not result in the desired product. Thus, an alternate route depicted in Scheme 6.3 was followed. Initially BDTT was reacted with 5-iodo-2-thiophenecarbaldehyde which yielded the desired product in low yield (<15%). However, the aldehyde functionality in **7** may not tolerate to the current reaction conditions. So, the aldehyde functional group was protected

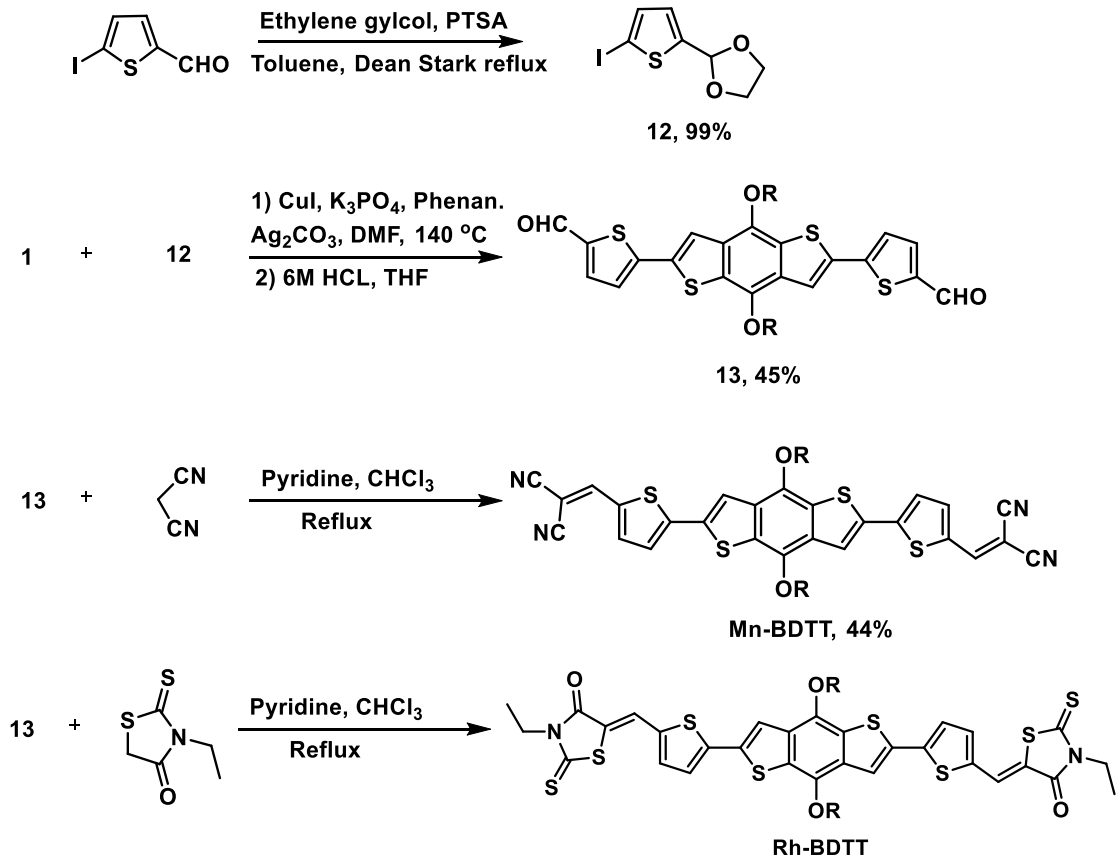

Scheme 6.3: Route 2 for the synthesis of BDTT based small molecules.

then reacted with BDTT followed by deprotection to form compound **13**. Compound **13** was then reacted with malononitrile and 3-ethylrhodanine to make the desired compound Mn-BDTT and Rd-BDTT respectively. Mn-BDTT was purified by column chromatography to give a 44% yield. Unfortunately, isolating the pure compound of Rd-BDTT was difficult. This could be related to the instability or lower solubility of the Rd-BDTT.

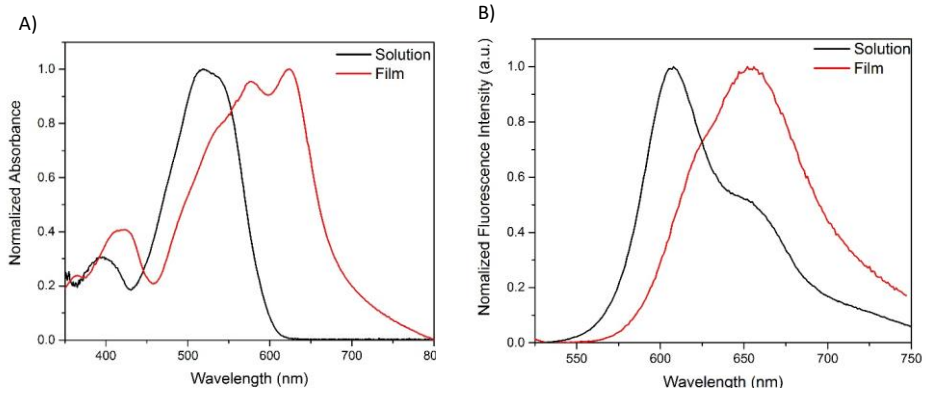

Figure 6.6: A) UV-vis absorption and B) Emission spectra of Mn-BDTT.

The optical properties of Mn-BDTT was investigated using UV-Vis absorption and fluorescence spectroscopy both as a dilute solution in $CHCl_3$ and in thin films. The absorption and emission spectra are shown in Figure 6.6A and 6.6B, respectively, and the results are summarized in Table 6.3. Mn-BDTT exhibits dual-absorption maxima near 400 and 550 nm both in solution and in thin film which is the general feature of the donor-acceptor system. As expected the absorption spectrum of film is red shifted compared to the solution one which is basically due to the $\pi - \pi$ stacking in film which leads to decrease in band gap. Similar trend was seen in fluorescence spectra with λmax for emission are 607 nm and 705 nm respectively in solution and film.

The molecular orbital energy levels of Mn-BDTT were determined using cyclic voltammetry (CV). The results are summarized on Table 6.3 and the cyclic voltamogram is shown in Figure 6.7A. In the cyclic voltammogram, only the reduction wave was observed with no oxidation wave while scanning up to -2V indicating the electron deficient nature of the molecule. The

LUMO level was calculated from the onset of the first reduction wave and found to be -3.92 eV which is quite close to that of the stand electron acceptor fullerene (-4.3 eV). The HOMO level was found to be -5.67 eV which was calculated by using the equation Optical Band Gap (E_g^{opt}) = HOMO – LUMO. Since Mn-BDTT has a low lying LUMO level, this molecule can be used as electron acceptor material to fabricate non-fullerene based organic solar cells.

Table 6.3: Optical and electronical properties of Mn-BDTT.

Absorption (nm)		Emission (nm)		E_{re} (V)[a]	HOMO[b] (eV)	LUMO[c] (eV)	Optical Band Gap[d] (eV)
Solution	Film	Solution	Film				
392,518	422,576,625	607	705	0.61	-5.67	-3.92	1.75

[a] Measure from the onset of first reduction wave. [b] Calculated from the equation E_g^{opt} (eV) = HOMO – LUMO. [c] Calculated from the onset of the first reduction wave using the equations E_{LUMO} (eV) = - $[E_{red}^{onset} - E_{1/2}(Fc/Fc^+) + 4.8]$ where $E_{1/2}$ (Fc/Fc^+) is the cell correction. [d] Measured (extrapolated) from the tangent drawn at the thin film absorption onset.

6.4 CONCLUSION

The electron poor building block benzodithiophene-*S*,*S*-tetraoxide has been successfully functionalized utilizing recently developed C-H iodination reaction for electron poor heteroarenes. The functionalized core was then incorporated as the acceptor unit on the donor-acceptor conjugated system to synthesize novel donor-acceptor polymers in high yields. These polymers have similar LUMO levels while the HOMO of PBDTT-BDT is higher in energy than PBDTT-Th as they have the same electron poor unit but the donor unit, the benzodithiophene in PBDTT-BDT is more electron rich compared to the thiophene donor unit in PBDTT-Th. While both of these polymers showed broad absorption of light ranging from 400 nm to 725 nm, they did not give any significant fluorescence. The electron accepting properties of these polymers were studied by performing fluorescence quenching experiments with donor material, P3HT. It has been found that both of these polymers are excellent quenchers with quenching constants

(K_{SV}) 3.7×10^5 $mol^{-1}L$ and 4.1 x 10^5 $mol^{-1}L$ for PBDTT-Th and PBDTT-BDT, respectively, which were similar to that of $PC_{60}BM$.

6.5 EXPERIMENTAL SECTION

6.5.1 Materials

Anhydrous toluene, DMF and THF were obtained from a solvent purification system under ultrapure argon. 4,8-Bis(decyloxy)benzo[1,2-*b*:4,5-*b*']dithiophene 1,1,5,5-tetraoxide (BDTT) and (4,8-Bis((2-ethylhexyl)oxy)benzo[1,2-*b*:4,5-*b*']dithiophene-2,6-diyl)bis(trimethylstannane) were synthesized according to the previously reported procedure. Regioregular poly(3-hexylthiophene) (rr-P3HT) was purchased from American Dye Source, Inc. All other chemicals were purchased from Sigma-Aldrich, Alfa Aesar and Oakwood Chemicals and were used as received.

6.5.2 Instrumentation

^1H and ^{13}C NMR spectra were acquired on a Bruker Avance 400 MHz instrument with TMS as the internal reference. Molecular weights of the polymers were obtained on gel permeation chromatography (GPC). GPC was performed using a Waters pump with a Waters 2410 refractive index detector using THF as solvent at 35 °C with a flow rate of 1.0 mL min^{-1}. Polystyrene standards were used for calibration. UV–visible and fluorescence spectra were recorded on a Cary 5000 UV–VIS–NIR spectrophotometer and a Cary Eclipse fluorescence spectrophotometer, respectively. UV–vis and fluorescence measurements were obtained using polymer solutions in $CHCl_3$, and thin films were drop casted from these solutions. Cyclic voltammetry was performed on a BASI CV-50W Version instrument with 0.1 M tetrabutylammonium hexafluorophosphate as the supporting electrolyte in dry acetonitrile using a platinum working electrode, platinum wire as the counter electrode, and Ag/Ag^+ as the reference electrode with a scan rate of 100 mV s^{-1}. The CV experiment was performed by drop casting a thin film of the polymer on the platinum

working electrode. TGA measurements were performed using a high-resolution thermogravimetric analyzer TA instrument Model Q-50, within the temperature interval of 30–900 °C, with a rate of 20 °C min^{-1} under continuous nitrogen flow. DSC was performed using a TA Instruments Model Q-2000 from -80 °C to 200 °C at a heating rate of 3 °C min^{-1} in a modulated mode. The second cooling cycle was chosen to observe the thermal transitions in polymers. All runs were performed under nitrogen.

6.5.3 Synthesis

Synthesis of 4,8-bis(dodecyloxy)-2,6-diiodobenzo[1,2-*b*:4,5-*b*']dithiophene 1,1,5,5-tetraoxide (**3**): To a solution of 4,8-bis(dodecyloxy)benzo[1,2-*b*:4,5-*b*']dithiophene 1,1,5,5-tetraoxide (BDTT) (100 mg, 0.16 mmol) in toluene (0.2 M) were added iodopentafluorobenzene (188 mg, 0.64 mmol), and potassium t-butoxide (9.0 mg, 0.08 mmol), and the mixture was stirred at room temperature for 30 min. After the reaction was completed, the solution was filtered through Celite®, concentrated and subjected to chromatography on silica gel with DCM and hexanes (1:2) as the eluent. The product **3** was isolated as a yellow solid (104 mg, 86%). Mp. 100-103 °C. ^{1}H NMR (400 MHz, $CDCl_3$) δ 7.59 (s, 2H), 4.43 (t, *J* = 6.5 Hz, 4H), 1.86 (p, *J* = 6.6 Hz, 4H), 1.48 (m, 4H), 1.38-1.27 (m, 32H), 0.88 (t, *J* = 6.5 Hz, 6H). ^{13}C NMR (101 MHz, CDCl3) δ 144.48, 132.97, 130.34, 129.49, 94.28, 31.92, 29.87, 29.65, 29.63, 29.57, 29.50, 29.35, 29.25, 25.67, 22.69, 14.13. HRMS (ESI) $[M]^+$ calcd for $C_{34}H_{52}I_2O_6S_2$ *m/z* 874.1295, *m/z* found 874.1307.

General procedure for the Stille polycondensation reactions: In a 10-mL oven-dried Schlenk flask were placed, 4,8-bis(dodecyloxy)-2,6-diiodobenzo[1,2-b:4,5-b']dithiophene 1,1,5,5-tetraoxide (100 mg, 0.11 mmol), $Pd_2(dba)_3$ (6.2 mg, 2 mol%) and tri-*tert*-butylphosphine (8.2 mg, 8 mol%) and put under vacuum for 5 minutes then purged with argon. This was repeated three times. Bis(trimethylstannyl)-substituted monomers (0.11 mmol) and chlorobenzene (3 mL) were

added inside the glove box, the solution was purged with Ar for 15 min and then heated at reflux for 2 days. The reaction mixture was cooled to room temperature and precipitated in methanol (20 mL) to give a black precipitate. The resulting precipitate was filtered through a Soxhlet thimble, which was then subjected to successive methanol, hexane, acetone and chloroform extractions. Finally, the chloroform extraction was evaporated to dryness and reprecipitated from methanol to yield black polymers.

Polymer, PBDTT-Th: Black powder (66 mg, 87% yield). ^{1}H NMR (400 MHz, $CDCl_3$) δ 7.71 (br s, 2H), 7.32 (b, 2H), 4.52 (br s, 4H), 1.93 (b, 4H), 1.27 (b, 36H), 0.88 (b, 6H). Mn = 10.7 kDa and PDI = 3.6.

Polymer, PBDTT-BDT: Black powder (93 mg, 82% yield). ^{1}H NMR (400 MHz, $CDCl_3$) δ 8.09 (b, 2H), 7.68 (b, 2H), 4.55 (b, 4H) 4.18 (b, 4H), 2.02 (b, 6H), 1.82-1.26 (b, 44H), 1.12-1.04 (b, 6H), 0.88 (b, 12H). Mn = 14.4 kDa and PDI = 2.6.

Synthesis of **5-iodothiophene-2-carbaldehyde (7):** In 100 ml three-necked round bottomed flask, dry diisopropylamine (0.074 mL, 0.523 mmol) was added to an inert environment and dry THF (15 mL) was added. The reaction mixture was cooled down to -78 °C and 2.5 M n-BuLi (0.476 mmol) was added dropwise. It was then stirred for 10-15 minutes at -78 °C and warmed to -40 °C. 2-iodothiophene (100 mg, 0.476 mmol) was added in one portion to the reaction mixture and stirred for 15 minutes at -40 °C. The solution was then warmed to -10 °C and stirred until the solution turned a dark red color indicating the complete lithiation of iodothiophene (about 30-45 minutes). The reaction mixture was again cooled down to -40 °C and added dry DMF (0.074 mL, 0.952 mmol). After addition of DMF, the reaction temperature was slowly warmed to 0 °C and the reaction was quenched by addition of saturated NH_4Cl (1 mL) solution. After extraction of the reaction mixture with Et_2O (3 x 10 mL), drying the combined extracts in $MgSO_4$ and removal of solvent *in vacuo*, a brown solid was obtained. The crude product was

purified by column chromatography on silica gel using hexane/ethyl acetate (9:1) as eluent to get pale yellow solid. Yield (83 mg, 74%). Mp. 43-45 °C. ^{1}H NMR (400 MHz, $CDCl_3$) δ 9.78 (s, 1H), 7.39 (s, 2H).

Synthesis of **2-((5-iodothiophen-2-yl)methylene)malononitrile (9):** In a 25 mL Schenk flask was added compound **7** (100 mg, 0.42 mmol), malononitrile (34 mg, 0.504 mmol) and dry $CHCl_3$ (1.5 mL) and purge with nitrogen gas for 15 minutes while stirring. A drop of piperidine was added and the reaction mixture was heated to reflux for overnight. The reaction mixture was cooled down and precipitated with 10 mL of methanol to get a brown solid. Yield (50 mg, 41%). Mp. 183-186 °C. ^{1}H NMR (400 MHz, $CDCl_3$) δ 7.76 (s, 1H), 7.43 (d, *J* = 4.0 Hz, 1H), 7.36 (d, *J* = 4.0 Hz, 1H).

Synthesis of **3-ethyl-5-((5-iodothiophen-2-yl)methylene)-2-thioxothiazolidin-4-one (11):** In a 25 mL Schenk flask was added compound **7** (100 mg, 0.42 mmol), 3-ethylrhodanine (82 mg, 0.504 mmol) and dry $CHCl_3$ (1.5 mL) and purge with nitrogen gas for 15 minutes while stirring. A drop of piperidine was added to the reaction mixture and was heated to reflux for overnight. The reaction mixture was cooled down and precipitated in 10 mL of methanol to get shiny black solid. Yield (150 mg, 93%). Mp. 189-192 °C. ^{1}H NMR (400 MHz, $CDCl_3$) δ 7.79 (s, 1H), 7.35 (d, *J* = 3.9Hz, 1H), 7.12 (d, *J* = 3.9Hz, 1H), 4.18 (q, *J* = 7.0Hz, 2H), 1.28 (t, *J* = 7.1Hz, 3H).

Synthesis of **2-(5-iodothiophene-2-yl)-1,3-dioxolane (12):** In a 100 mL one-necked round-bottomed flask, 5-iodothiophene-2-carbaldehyde (1g, 4.2 mmol) was dissolved in dry toluene (30 mL) and then ethylene glycol (0.704 mL, 12.6 mmol) and *p*-toluenesulfonic acid monohydrate (8 mg, 0.042 mmol) were added. The flask was equipped with a Dean-Stark trap and the reaction was refluxed overnight. The reaction mixture was then cooled to room temperature, washed with deionized water and extracted with ethyl acetate. The organic layer was dried ($MgSO_4$) and concentrated *in vacuo* to afforded **3** as a light brown liquid. From the ^{1}H NMR, the product was

found to contain 3% of the starting material, which was used for next step without further purification. Yield (1.1 g, 99%). To get rid of the staring material the reaction was worked up with the saturated sodium bicarbonate, but still starting material was present on the product. ^{1}H NMR (400 MHz, $CDCl_3$) δ 7.13 (d, *J* = 3.7 Hz, 1H), 6.83 (d, *J* = 3.7 Hz, 1H), 6.07 (s, 1H), 4.11-3.98 (m, 4H).

Synthesis of **5,5'-(4,8-Bis(dodecyloxy)benzo[1,2-b:4,5-b']dithiophene-2,6-diyl)bis(thiophene-2-carbaldehyde) (13):** 4,8-Didodecyloxybenzo[1,2-b;3,4- b]dithiophene-1,1,5,5-tetraoxide (500 mg, 0.80 mmol) was added in a glovebox to a 50 mL reaction vessel, followed by 2-(5-iodothiophene-2-yl)-1,3-dioxolane (0.45 mg, 1.60 mmol), CuI (46 mg, 0.24 mmol), 1,10-phenanthroline (87 mg, 0.48 mmol), Ag_2CO_3(221 mg, 0.80 mmol), K_3PO_4 (349 mg, 1.61 mmol), and dry DMF (20 mL). The reaction vessel was sealed, removed from the glovebox, and stirred at 140 °C for 2 h. The reaction mixture was allowed to cool to room temperature, poured into 6 M HCl solution (5 mL) and stirred for overnight. The reaction mixture was then extracted with dichloromethane and the organic layer was washed with deionized water, dried ($MgSO_4$) and concentrated *in vacuo*. The residue was purified by dissolving in DCM/methanol (1:1) mixture and subsequent rotary evaporation to precipitate the product. The suspension was filtered, and washed with cold methanol to obtain the pure product (orange solid). Yield (301 mg, 45%). Mp. 246-250 °C. ^{1}H NMR (400 MHz, $CDCl_3$) δ 9.97 (s, 2H), 7.80 (d, *J* = 4.1 Hz, 2H), 7.76 (d, *J* = 4.1 Hz, 2H), 7.44 (s, 2H), 4.52 (t, *J* = 6.6 Hz, 4H), 1.94 (p, *J* = 6.7 Hz, 4H), 1.43 – 1.27 (m, 32H), 0.88 (t, *J* = 6.8 Hz, 6H). ^{13}C NMR (101 MHz, $CDCl_3$) δ 182.42, 145.48, 145.15, 137.05, 136.94, 136.65, 131.01, 129.03, 127.68, 119.62, 31.93, 29.95, 29.68, 29.66, 26.63, 29.56, 29.37, 29.32, 25.77, 22.70, 14.14.

Synthesis of **2,2'-(((4,8-bis(tridecyloxy)benzo[1,2-b:4,5-b']dithiophene-2,6-diyl)bis(thiophene-5,2-diyl))bis(methaneylylidene))dimalononitrile (Mn-BDTT):** To a 100-mL three-necked round-bottomed flask were added 4,8-didodecyloxybenzo[1,2-b;3,4-

b]dithiophene-1,1,5,5-tetraoxide, (300 mg, 0.35 mmol), malononitrile (231 mg, 3.5 mmol) and chloroform (40 mL). The mixture was deoxygenated with nitrogen for 15 min, pyridine (1.5 mL) was added and the reaction was refluxed for overnight. After cooling to room temperature, the mixture was poured into methanol (200 mL) and filtered. The residue was purified by column chromatography on silica gel using hexane/DCM (1:4) as eluent, yielding a dark blue solid (150 mg, 45%). Mp. 242-244 °C. ^{1}H NMR (400 MHz, $CDCl_3$): δ. 7.84 (s, 2H), 7.80 (d, *J* = 4.1 Hz, 2H), 7.76 (d, *J* = 4.2 Hz, 2H), 4.55 (t, *J* = 6.7 Hz, 4H), 1.98 (p, *J* = 6.9 Hz, 4H), 1.59-1.52 (m, 4H), 1.41-1.27 (m, 36H), 0.89 (t, *J* = 6.7 Hz, 6H). ^{13}C NMR (101 MHz, $CDCl_3$): δ 149.40, 145.87, 139.19, 138.58, 137.17, 136.65, 131.20, 129.25, 128.03, 120.41, 113.19, 112.63, 80.90, 31.94, 29.98, 29.71, 29.65, 29.59, 29.54, 29.35, 29.29, 25.74, 22.67, 14.04.

Synthesis of **(5Z,5'Z)-5,5'-(((4,8-bis(dodecyloxy)benzo[1,2-b:4,5-b']dithiophene-2,6-diyl)bis(thiophene-5,2-diyl))bis(methaneylylidene))bis(3-ethyl-2-thioxothiazolidin-4-one) (Rd-BDTT):** To a 100-mL three-necked round-bottomed flask were added 4,8-didodecyloxybenzo[1,2-b;3,4- b]dithiophene-1,1,5,5-tetraoxide, (100 mg, 0.11 mmol), 3-ethylrhodanine (177 mg, 1.1 mmol) and chloroform (15 mL). The mixture was deoxygenated with nitrogen for 15 min, piperidine (1 mL) was added and the reaction was refluxed for overnight. After cooling to room temperature, the mixture was poured into methanol (75 mL) and filtered.

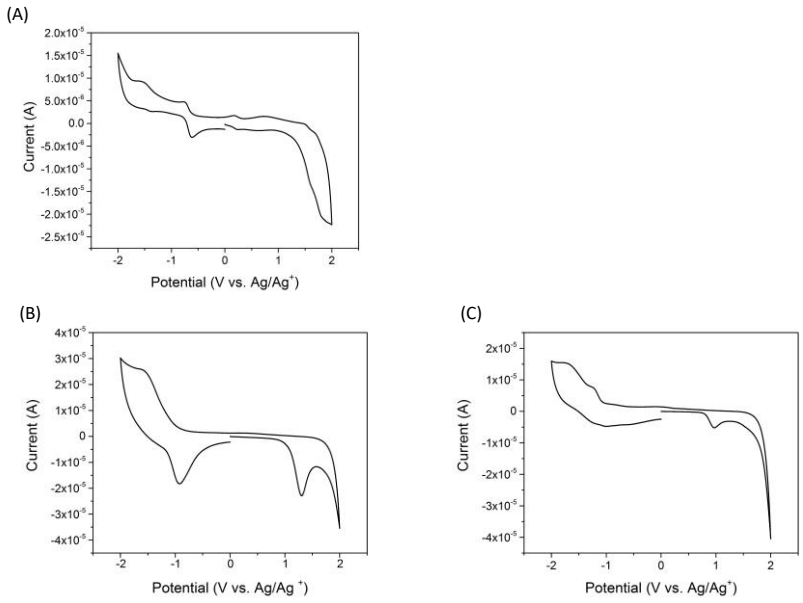

Figure 6.7: CV spectra of (A) Mn-BDTT, (B) PBDTT-Th, and (C) PBDTT-BDT.

6.6 REFERENCES

(1) Shirakawa, H.; Louis, E. J.; MacDiarmid, A. G.; Chiang, C. K.; Heeger, A. J. Synthesis of electrically conducting organic polymers: halogen derivatives of polyacetylene, (CH). *Journal of the Chemical Society, Chemical Communications* **1977**, 578-580.

(2) Xu, R.-P.; Li, Y.-Q.; Tang, J.-X. Recent advances in flexible organic light-emitting diodes. *Journal of Materials Chemistry C* **2016**, *4*, 9116-9142.

(3) Torsi, L.; Magliulo, M.; Manoli, K.; Palazzo, G. Organic field-effect transistor sensors: a tutorial review. *Chemical Society Reviews* **2013**, *42*, 8612-8628.

(4) Hedley, G. J.; Ruseckas, A.; Samuel, I. D. W. Light Harvesting for Organic Photovoltaics. *Chemical Reviews* **2017**, *117*, 796-837.

(5) Bernards, D. A.; Malliaras, G. G.; Owens, R. M., Eds.;*Organic Semiconductors in Sensor Applications*; Springer: Verlag Berlin, Heidelberg, **2008**; Vol. 107.

(6) Hamedi, M.; Forchheimer, R.; Inganäs, O. Towards woven logic from organic electronic fibres. *Nature Materials* **2007**, *6*, 357.

(7) Rockett, A. In *The Materials Science of Semiconductors* Spinger: Boston, MA, **2008**, p 395-453.

(8) Kelley, T. W.; Baude, P. F.; Gerlach, C.; Ender, D. E.; Muyres, D.; Haase, M. A.; Vogel, D. E.; Theiss, S. D. Recent Progress in Organic Electronics: Materials, Devices, and Processes. *Chemistry of Materials* **2004**, *16*, 4413-4422.

(9) Quinn, J. T. E.; Zhu, J.; Li, X.; Wang, J.; Li, Y. Recent progress in the development of n-type organic semiconductors for organic field effect transistors. *Journal of Materials Chemistry C* **2017**, *5*, 8654-8681.

(10) Shan, B.; Miao, Q. Molecular design of n-type organic semiconductors for high-performance thin film transistors. *Tetrahedron Letters* **2017**, *58*, 1903-1911.

(11) Yao, H.; Ye, L.; Zhang, H.; Li, S.; Zhang, S.; Hou, J. Molecular Design of Benzodithiophene-Based Organic Photovoltaic Materials. *Chemical Reviews* **2016**, *116*, 7397-7457.

(12) Khambhati, D. P.; Sachinthani, K. A. N.; Rheingold, A. L.; Nelson, T. L. Regioselective copper-catalyzed direct arylation of benzodithiophene-S,S-tetraoxide. *Chemical Communications* **2017**, *53*, 5107-5109.

(13) Shi, Q.; Zhang, S.; Zhang, J.; Oswald, V. F.; Amassian, A.; Marder, S. R.; Blakey, S. B. KOtBu-Initiated Aryl C–H Iodination: A Powerful Tool for the Synthesis of High Electron Affinity Compounds. *Journal of the American Chemical Society* **2016**, *138*, 3946-3949.

(14) Marios, N.; Daniel, B.; Sergei, L.; Hu, C.; K., H. R.; Lewis, C.; Iain, M.; Wan, Y. Alternative Thieno[3,2-b][1]benzothiophene Isoindigo Polymers for Solar Cell Applications. *Macromolecular Rapid Communications*, *0*, 1700820.

(15) Wood, J. D.; Jellison, J. L.; Finke, A. D.; Wang, L.; Plunkett, K. N. Electron Acceptors Based on Functionalizable Cyclopenta[hi]aceanthrylenes and Dicyclopenta[de,mn]tetracenes. *Journal of the American Chemical Society* **2012**, *134*, 15783-15789.

(16) Gauthier, T. D.; Shane, E. C.; Guerin, W. F.; Seitz, W. R.; Grant, C. L. Fluorescence quenching method for determining equilibrium constants for polycyclic aromatic hydrocarbons binding to dissolved humic materials. *Environmental Science & Technology* **1986**, *20*, 1162-1166.

CHAPTER VII

CONCLUSION AND FUTURE DIRECTIONS

7.1 INTRODUCTION

In this chapter, I have described conclusion from the chapter 2 through 6 and have also outlined the future directions of these projects.

7.2 CHAPTER 2: CONCLUSION AND FUTURE DIRECTIONS

In Chapter 2, the effect of structural variation on the optoelectronic properties of Eumelanin-inspired indole small molecules was studied by combining both synthetic and computational techniques. Five new Eumelanin-inspired indole small molecules have been synthesized which differ by the substituents attached to the para-position of the phenylene ring. The results suggested that the frontier orbitals, and hence the bandgap and optical properties of the molecules can be manipulated by substituting different electron donating and electron withdrawing groups at the para-position of the phenylene ring.[1] Furthermore, the unique chromic response of one of the eumelanin-inspired molecule to TFA suggested the potential utility of these type of molecules as an acidochromic sensor. In general, this chapter demonstrates the utility of the eumelanin-inspired indole core and opens up the possibility of designing materials with interesting properties for specific applications by decorating this core with various functionalities. Moreover, this work brings the field one step closer to elucidating and enhancing the properties of the naturally occurring eumelanin.

For future work, the study of the properties of the eumelanin-inspired co-crystals formed between the two eumelanin inspired small molecules; one having strong electron withdrawing group (compound **2e** from chapter 2) (electron deficient molecule) and the other with strong electron donating group (compound **2b** from chapter 2) (electron donating molecule) could be interesting in further elucidating and enhancing the properties of naturally occurring eumelanin and in making bio-inspired electronics.[2]

7.3 CHAPTER 3 CONCLUSION AND FUTURE DIRECTIONS

Chapter 3 demonstrated the intrinsic antimicrobial activity of eumelanin-inspired indole core (DBI) and the enhancement of its antimicrobial activity with the incorporation of bacteria targeting sites. A novel eumelanin-inspired antimicrobial (EIPE-1) was synthesized which was found to have antimicrobial activity against gram-positive bacteria. Specifically EIPE-1 demonstrated activity against *S. aureus* with a minimum inhibitory concentration of 16 μg/mL. The bactericidal activity of EIPE-1 against *S. aureus* was confirmed by Live/Dead staining experiments and scanning electron micrographs suggested that membrane damage of *S. aureus* was occurring with EIPE-1 treatment.

Since, EIPE-1 did not show any activity against gram-negative bacteria including *Pseudomonas aeruginosa,* the future work could be designing and synthesizing eumelanin-inspired antimicrobials with broad bactericidal spectrum that target both gram-positive as well as gram-negative bacteria. It would be also important to investigate the antifungal activities of eumelanin-inspired indole core and its derivatives.

7.4 CHAPTER 4 CONCLUSION AND FUTURE DIRECTIONS

In chapter 4, a series of conjugated polymers based on the Eumelanin-inspired indole core were synthesized differing by the arylene and carbon–carbon bond linkages and the effect of these differences on the optoelectronic properties of the conjugated polymers were studied.[3] Also an

effort to synthesize high molecular weight poly(indoyleneethynylene) and poly(indoylenevinylene) polymers was attempted by putting solubilizing group on the eumelanin-inspired indole core. In future, different reactions conditions could be employed in order to synthesize high molecular weight conjugated polymers from eumelanin-inspired indole core having long or branched alkyl chains as a solubilizing groups (compound **10** from chapter 4).

7.5 CHAPTER 5 CONCLUSION AND FUTURE DIRECTIONS

Chapter 5 demonstrated the very simple, scalable, and economical method for the fabrication of organic electrically conductive fibers (ECFs) by coating commercially available non-conducting fibers such as cotton, polyester, and silk with the conductive ink composed of two intrinsically conductive materials *viz*: single walled carbon nanotubes (SWCNTs) and poly(3-hexylthiophene) (P3HT). These organic ECFs were found to retain the native materials mechanical and physical properties and were successfully used to record skin surface biological signals with signal to noise ratios that were similar and exceeded the data by standard metal electrodes illustrating the promise of these materials to be used in modern medical diagnostic and treatment.

One of the drawbacks of our organic conductive fibers is that the conductive materials are only adsorbed on the fibers so they may come off during use. Future work could be focused on forming covalent bond between the conductive ink components and original fibers. It could be achieved by functionalizing SWCNTs and/or P3HT such that they can form covalent bonds on the surface of the original fibers. One way could be end chain functionalization of P3HT with trimethoxysilane groups and use these groups to covalently bond with the hydroxyl groups on the cotton fibers. The other method could be the use of carboxylic acid functionalized SWCNTs which could form hydrogen bonding with the hydroxyl groups present on the cotton fibers.

7.6 CHAPTER 6 CONCLUSION AND FUTURE DIRECTIONS

In chapter 6, benzodithiophene-*S,S*-tetraoxide (BDTT) based novel n-type organic semiconductors (OSCs) both small molecules as well as polymers were synthesized and characterized. BDTT based n-type small molecules were synthesized by the copper catalyzed regio-selective C-H direct arylation reaction developed in our lab. BDTT based n-type polymers were achieved by synthesizing donor-acceptor polymers under Stille polymerization conditions using BDTT core as electron deficient unit. These polymers were illustrated as a good electron accepting materials by performing fluorescence quenching experiments with prototypical donor material P3HT.

In future, the BDTT core could be further explored to synthesize donor-acceptor conjugated polymers with narrow bandgaps. Some narrow bandgap conjugated polymers have been known to possess ambipolar (electron and hole) mobility and also can be used in making infrared light sensing devices. Furthermore, the 3-position on rhodadine could be substituted with long alkyl chain to make the final BDTT based molecule more soluble. This could help to purify the final BDTT based small molecules.

7.7 REFERENCES

(1) Selvaraju, S.; Adhikari, S.; Hopson, R. A.; Dai, S.; Rheingold, A. L.; Borunda, M. F.; Nelson, T. L. Effects of structural variations on the optical and electronic properties of eumelanin-inspired small molecules. *Journal of Materials Chemistry C* **2016**, *4*, 3995-3999.

(2) Zhang, J.; Xu, W.; Sheng, P.; Zhao, G.; Zhu, D. Organic Donor–Acceptor Complexes as Novel Organic Semiconductors. *Accounts of Chemical Research* **2017**, *50*, 1654-1662.

(3) Adhikari, S.; Hopson, R. A.; Sedai, B. R.; McFarland, F. M.; Guo, S.; Nelson, T. L. Synthesis and characterization of eumelanin-inspired poly(indoylenearylenevinylene)s and

poly(indoylenearyleneethynylene)s. *Journal of Polymer Science Part A: Polymer Chemistry* **2017**, *55*, 457-463.

VITA

Santosh Adhikari

Candidate for the Degree of

Doctor of Philosophy

Dissertation: DESIGN, SYNTHESIS AND CHARACTERIZATION OF ORGANIC SEMICONDUCTORS: FROM EUMELANIN-INSPIRED ORGANIC MATERIALS TO NOVEL ELECTRON ACCEPTORS

Major Field: Organic Chemistry

Biographical:

Education:

Completed the requirements for the Doctor of Philosophy in Organic Chemistry at Oklahoma State University, Stillwater, Oklahoma in July, 2018.

Completed the requirements for the Master of Science in Physical Chemistry at Tribhuvan University, Kathmandu, Nepal in 2007.

Completed the requirements for the Bachelor of Science in Chemistry at Tribhuvan University, Kathmandu, Nepal in 2005.

Experience:
Teaching and research assistant, Department of Chemistry, Oklahoma State University, Stillwater, OK, 2013-2018.
Assistant Lecturer, Cosmos College of Management and Technology, Lalitpur, Nepal, 2009-2013.

Professional Memberships:
American Chemical Society (Division of Polymer Chemistry)
Nepal Polymer Institute
Electrochemical Society, Oklahoma Chapter

Awards and Honors:
Merrill and Winona M. Schnitzer Outstanding Graduate Student Award, Department of Chemistry, Oklahoma State University, OK, 2018.
O. C. Dermer Scholarship Award, Department of Chemistry, Oklahoma State University, Stillwater, OK, March 2016
Phi Kappa Phi Society induction award for excellent academic accomplishments, Oklahoma State University, Stillwater, OK, 2015